# Impact on Liquids: Void Collapse and Jet Formation

Stephan Gekle

**Samenstelling promotiecommissie:**

| | |
|---|---|
| Prof. dr. Leen van Wijngaarden (voorzitter) | Universiteit Twente |
| Prof. dr. Detlef Lohse (promotor) | Universiteit Twente |
| Dr. Devaraj van der Meer (assistent-promotor) | Universiteit Twente |
| Prof. dr. José Manuel Gordillo (assistent-promotor) | Universidad de Sevilla |
| Dr. Onno Bokhove | Universiteit Twente |
| Prof. dr. Arjen Doelman | Universiteit van Amsterdam |
| Prof. dr. Paul Kelly | Universiteit Twente |
| Prof. dr. Walter Zimmermann | Universität Bayreuth |

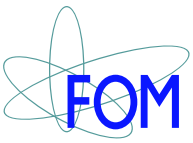


The work in this thesis was carried out at the Physics of Fluids group of the Faculty of Science and Technology of the University of Twente. It is part of the research programme of the Foundation for Fundamental Research on Matter (FOM), which is financially supported by the Netherlands Organisation for Scientific Research (NWO).

Nederlandse titel:
*Inslag van een object op water: Hoe de implosie van een holte leidt tot de vorming van een jet*

Publisher:
Stephan Gekle, Physics of Fluids, University of Twente,
P.O. Box 217, 7500 AE Enschede, The Netherlands
pof.tnw.utwente.nl
Cover Illustration: Stefanie Gekle


ISBN: 978-90-365-2929-7

# IMPACT ON LIQUIDS:
# VOID COLLAPSE AND JET FORMATION

PROEFSCHRIFT

ter verkrijging van
de graad van doctor aan de Universiteit Twente,
op gezag van de rector magnificus,
Prof. dr. H. Brinksma,
volgens besluit van het College voor Promoties
in het openbaar te verdedigen
op vrijdag 13 november 2009 om 11.00 uur

door

Stephan Gekle
geboren op 20 juni 1978
te Nürtingen, Duitsland

Dit proefschrift is goedgekeurd door de promotor:

Prof. dr. rer. nat. Detlef Lohse

en de assistent-promotoren:

Dr. Devaraj van der Meer
Prof. dr. José Manuel Gordillo

# Contents

# 1 Introduction

The thin liquid jet ejected after the impact of an object onto a water surface has been one of the icons of fluid mechanics for more than a century [1]. Despite a plethora of experimental, theoretical, and computational studies this only seemingly simple every-day phenomenon keeps scientists busy even today yielding ever new and surprising discoveries. Some of these are described in the present thesis.

Besides the intrinsic interest of understanding such a well-known and immensely frequent phenomenon, impacts can be of enormous practical importance in, for example, climate research: every day billions of raindrops hit the surface of the ocean and each of them entrains a small air bubble [2, 3]. Such an entrainment constitutes an important mechanism of carbon dioxide exchange between the atmosphere and the sea [4, 5]. Furthermore, the oscillations of these bubbles are a major source of underwater noise and as such are crucial for sonar research [6]. In medical physics, scientists are currently seeking ways to use thin liquid jets similar to the ones created during solid object impact for drug delivery through cell membranes or through a patient's skin [7, 8].

Before going into details, we first illustrate in Fig. 1.1 the sequence of principal events during the impact process. Right upon impact a thin sheet of liquid (the "crown splash") is thrown upwards along the rim of the solid object. Below the water surface a large cavity forms in the wake of the impactor which almost immediately starts to collapse due to the hydrostatic pressure of the surrounding liquid. This pressure acts on every point of the free surface accelerating it inward as soon as the object has

passed with a force that increases with the depth. Thus, points near the top surface start moving early with a small acceleration, while deeper points start with increasing delay, but higher acceleration [9, 10]. This subtle balance results in the closing of the cavity in a single point (about halfway down its length for the impacting disc in Fig. 1.1).

As soon as the cavity closes two fast sharp-pointed jets are observed shooting up- and downwards from the closure location. These originate as the fluid that rushes inwards hits the axis of symmetry making any further radial motion impossible. The abrupt deceleration of the fluid leads to a zone of very high pressure and consequently to a strong vertical acceleration: the jets emerge.

Most impactors in reality are bulky objects extending in all three spatial directions. In a laboratory the most common setup is a sphere being dropped into a water tank. As realized already by Worthington [1] at the beginning of the last century the surface characteristics of the impacting object are of crucial importance for the formation of the impact cavity: while a rough sphere creates a large cavity a smoothly polished sphere can penetrate the water almost without creating any cavity at all. The key to understand this discrepancy lies in the motion of the water/air/liquid contact line: for a smooth wetting sphere it can easily slide around the object and close on top while for the rough sphere it becomes pinned at the sphere's equator leading to the formation of a large impact cavity.

For our purposes it is important to obtain a large, undisturbed, and reproducible cavity in order to study the various aspects of the impact, collapse, and jetting process. By impacting a flat disc we can avoid the above mentioned complications since the contact line remains pinned at the disc's edge throughout the entire process. To ensure that the disc impacts in a perfectly horizontal way we attach it to the end of a long steel rod. This rod runs through the bottom of a water tank where it is connected to a vertically moving linear motor which allows us to pull the disc through the surface at a constant velocity.

In addition to the experimental studies we will present in this thesis an extensive set of numerical simulations. The simulations are conducted using a "boundary-integral" simulation code which was developed as part of this thesis based on an earlier version used in [11]. The boundary-integral method uses a potential flow description assuming an inviscid and irrotational fluid. These assumptions are expected to be very well satisfied as can be seen by evaluating global and local Reynolds numbers, all of which are at least of the order of 100 and usually much larger [12]. The agreement between experiment and simulation depicted in Fig. 1.1 is very good.

We have thus at our disposal a combination of a sophisticated experimental setup and a powerful numerical method which we can use to elucidate various aspects of

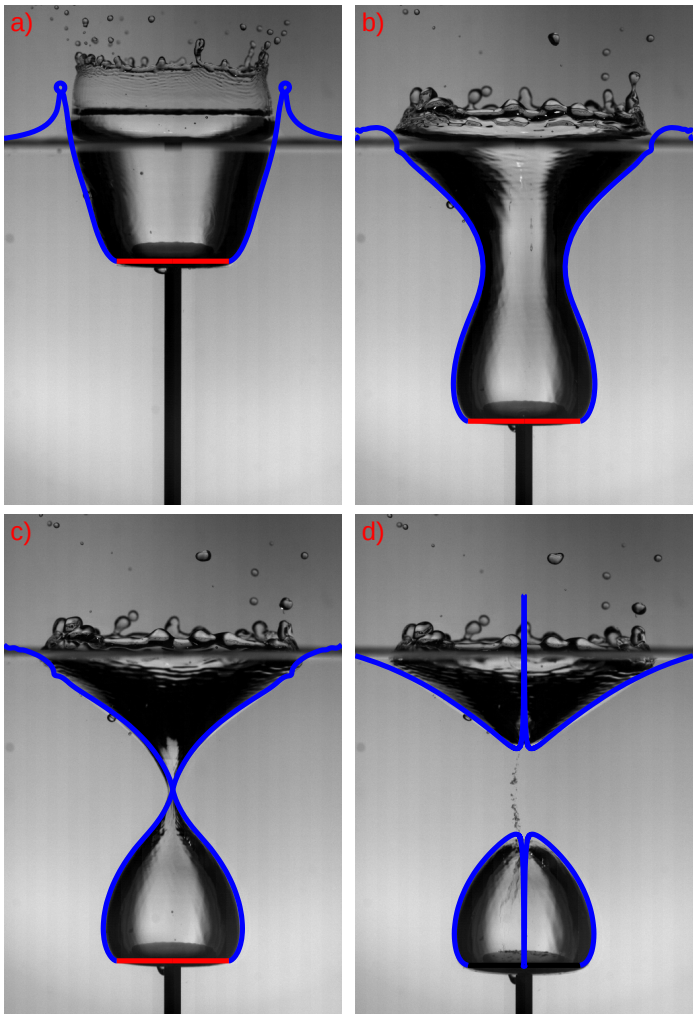


Figure 1.1: The sequence of events as a circular disc of 2 cm radius impacts a water surface at 1 m/s: (a) Immediately after impact a crown splash is ejected into the air while below the water surface a large cavity is created. (b) Due to hydrostatic pressure from the surrounding liquid the cavity starts to collapse. (c) Eventually the cavity closes in a single point pinching off its lower half as a giant bubble. (d) After closure two violent jets emerge shooting up- and downwards from the closure location. The blue and red lines represent the free surface and the disc, respectively, from our numerical simulation which is in very good agreement with the experimental images.

the common, yet fascinatingly beautiful, phenomenon of solid-liquid impact.

In Chapter 2 we will show in detail how the initial downward motion of the disc is, upon impact, turned into the upward motion of the liquid jet. For this we will illustrate how the collapsing cavity wall squeezes out the jet very much like the squeezing of a tube of tooth paste – but of course much faster. Observations made from detailed numerical simulations will lead us to construct an analytical model to describe the jet formation mechanism which we find in very good agreement with our simulations and experiments.

Next, in Chapter 3, we will show how to predict not only jet formation, but the entire shape of the ejected liquid jets. For this purpose, the results from the previous chapter will serve as an input into a new and independent theoretical model for the stretching of the jet. We will show further that the break-up of such a stretching thin jet due to a surface-tension driven (Rayleigh-Plateau)-instability can be fully described by only two non-dimensional quantities determined at the very beginning of jet formation. Finally, we will demonstrate that our three-step jetting model – formation, stretching, break-up – can not only be applied to jets after solid object impact but also to the liquid jets observed after the pinch-off of gas bubbles injected from a small underwater nozzle into a quiescent liquid pool as in, e.g. [13–15].

In Chapter 4 we will use a new multiphase computational scheme coupling our boundary-integral method for the liquid to a fully compressible Euler solver for the gas dynamics to illustrate the stream of air as it is first sucked into and later pushed out of the impact cavity. We will combine these computations with experiments in which the air flow is visualized using fine smoke particles. The striking result is that the air is pushed out of the cavity so violently that it attains *supersonic* speeds. Perhaps even more striking, due to the rapidly shrinking liquid cavity these high air speeds can be achieved with pressures inside the bubble being merely 2% larger than the surrounding atmosphere.

In Chapter 5 we will present the details of the computational scheme used in the previous chapter. This chapter also covers a number of interesting aspects regarding the boundary-integral implementation used in the other parts of this work.

A long-standing controversy in the fluid dynamics community has been until recently the pinch-off of an elongated bubble with a neck which – due to some external forcing – is shrinking in time. It was predicted initially that the neck should shrink in a universal fashion determined only by liquid inertia [13, 16]. The fact, however, that the predicted power-law with an exponent of 1/2 could not be found experimentally raised doubts about whether or not bubble pinch-off was a truly universal phenomenon (as is its close cousin, the pinch-off of a liquid thread surrounded by air). A recent theory then predicted a universal behavior but with a more complicated,

time-dependent local exponent [17]. The crucial aspect which was not addressed in [17] is whether this universal behavior would actually occur on time scales which are observable in a real experiment. In Chapter 6 we go back to the single-phase boundary-integral simulations of the first two chapters to answer this question for a number of different systems including the impacting disc. Surprisingly, we find that the duration of the universal regime differs by many orders of magnitude from one system to another – a fact which we use to explain why and how universal behavior can (indirectly) be observed in some systems and not in others.

In Chapter 7 we slightly modify our experimental and computational setup replacing the disc with a long cylinder. As we will show this leads to a qualitatively new behavior of the cavity closure. While for the disc the closure depth scales continuously with the impact velocity, for a submerging cylinder it exhibits discontinuous jumps at certain well-defined velocities. These jumps can be traced back to the occurrence of capillary waves which are created at the very beginning of the impact and are not present in the case of the impacting disc.

Chapter 8 connects back to the first two chapters studying jetting phenomena: here we will use our boundary-integral simulations to illustrate how nanopits (with radii of roughly 50 nm) can be filled with liquid by tiny jets. In the experimental setup, an array of nanopits drilled into a silicon wafer is submerged in pure water. Due to the stabilizing effect of surface tension the pits initially remain filled with air. A strong underpressure created by an ultrasound pulse triggers the nucleation of bubbles out of the nanopits which immediately collapse as soon as normal pressure is restored. It is an intriguing observation that each nanopit can nucleate a bubble exactly once. Our simulations show that during the collapse of the first bubble a very thin jet is formed which can penetrate into the nanopit and, as it hits the bottom, fills the pit with liquid making a second nucleation impossible.

Finally, Chapter 9 presents some overall conclusions and suggests possibilities for further study.

# References

[1] A. M. Worthington, *A study of splashes* (Longmans, Green and Co., London) (1908).

[2] H. N. Oguz and A. Prosperetti, “Bubble entrainment by the impact of drops on liquid surfaces”, J. Fluid Mech. **219**, 143–179 (1990).

[3] M. Rein, “Phenomena of liquid drop impact on solid and liquid surfaces”, Fluid. Dyn. Res. **12**, 61–93 (1993).

[4] R. F. Keeling, "On the role of large bubbles in air-sea gas exchange and supersaturation in the ocean", J. Marine Res. **51**, 237–271 (1993).

[5] D. K. Woolf, "Bubbles and their role in gas exchange", in *The Sea Surface and Global Change*, edited by P. S. Liss and R. A. Duce (Cambridge University Press) (1997).

[6] H. N. Oguz and A. Prosperetti, "Numerical calculation of the underwater noise of rain", J. Fluid Mech. **228**, 417–442 (1991).

[7] C. D. Ohl and R. Ikink, "Shock-wave-induced jetting of micron-sized bubbles", Phys. Rev. Lett. **90**, 214502 (2003).

[8] M. Postema, A. van Wamel, F. J. ten Cate, and N. de Jong, "High-speed photography during ultrasound illustrates potential therapeutic applications of microbubbles", Med. Phys. **32**, 3707–3711 (2005).

[9] V. Duclaux, F. Caillé, C. Duez, C. Ybert, L. Bocquet, and C. Clanet, "Dynamics of transient cavities", J. Fluid Mech. **591**, 1–19 (2007).

[10] D. Lohse, R. Bergmann, R. Mikkelsen, C. Zeilstra, D. van der Meer, M. Versluis, K. van der Weele, M. van der Hoef, and H. Kuipers, "Impact on soft sand: void collapse and jet formation", Phys. Rev. Lett. **93**, 198003 (2004).

[11] R. Bergmann, D. van der Meer, M. Stijnman, M. Sandtke, A. Prosperetti, and D. Lohse, "Giant bubble pinch-off", Phys. Rev. Lett. **96**, 154505 (2006).

[12] R. Bergmann, D. van der Meer, S. Gekle, A. van der Bos, and D. Lohse, "Controlled impact of a disc on a water surface: Cavity dynamics", J. Fluid Mech. **633**, 381–409 (2009).

[13] H. N. Oguz and A. Prosperetti, "Dynamics of bubble growth and detachment from a needle", J. Fluid Mech. **257**, 111–145 (1993).

[14] S. T. Thoroddsen, T. G. Etoh, and K. Takehara, "Experiments on bubble pinch-off", Phys. Fluids **19**, 042101 (2007).

[15] R. Bolaños-Jiménez, A. Sevilla, C. Martinez-Bazán, and J. M. Gordillo, "Axisymmetric bubble collapse in a quiescent liquid pool. II. Experimental study", Phys. Fluids **20**, 112104 (2008).

[16] M. S. Longuet-Higgins, B. R. Kerman, and K. Lunde, "The release of air bubbles from an underwater nozzle", J. Fluid Mech. **230**, 365–390 (1991).

[17] J. Eggers, M. A. Fontelos, D. Leppinen, and J. H. Snoeijer, "Theory of the collapsing axisymmetric cavity", Phys. Rev. Lett. **98**, 094502 (2007).

# 2

# High-speed jet formation after solid object impact *

*A circular disc impacting on a water surface creates an impact crater which after collapse leads to a remarkably vigorous jet. Upon impact an axisymmetric air cavity forms and eventually pinches off in a single point halfway down the cavity. Immediately after closure two fast sharp-pointed jets are observed shooting up- and downwards from the closure location, which by then has turned into a stagnation point. This stagnation point deflect the radially inflowing liquid vertically up and down creating a locally hyperbolic flow pattern. This flow, however, is not the mechanism feeding the two jets. Using high-speed imaging and numerical simulations we show that jetting is fed by the local flow around the base of the jet, which is forced by the colliding cavity walls. Based on this insight, we then show how the well-known analytical description of a collapsing void (using a line of sinks along the axis of symmetry) can be continued beyond the time of pinch-off to obtain a new and quantitative model for jet formation which is in good agreement with the numerical and experimental data.*

*Published as: Stephan Gekle, José Manuel Gordillo, Devaraj van der Meer, and Detlef Lohse, "High-speed jet formation after solid object impact", Phys. Rev. Lett. **102**, 034502 (2009).

## 2.1 Introduction

The most prominent phenomenon when a solid object hits a water surface is the high-speed jet shooting upwards into the air. The basic sequence of events leading to this jet has been studied since Worthington over a century ago: After impact, the intruder creates an air-filled cavity in the liquid which due to hydrostatic pressure immediately starts to collapse, eventually leading to the pinch-off of a large bubble. Two very thin jets are ejected up- respectively downwards from the pinch-off point. This finite-time singularity has been intensively studied in recent time [1–4]. Such singularities have been shown to lead to a hyperbolic flow pattern after collapse and thus to the formation of liquid jets [5–8].

As we show in the present work, however, the radial energy focussing towards the singular pinch-off point alone is not sufficient to explain the extreme thinness of jets observed after the impact of a solid object. Instead, this jet formation is shown to depend crucially on the kinetic energy contained in *the entire collapsing wall of the cavity* even far above the pinch-off singularity.

This is in contrast to jets observed in many other situations where narrow confining cavity walls are not present, e. g. for bubbles bursting on a free surface or near a solid wall [8–10], wave focussing [11, 12], or jets induced by pressure waves [13]. In addition, surface tension in our case turns out to be irrelevant in contrast to capillary-driven scenarios as suggested for Faraday waves [6, 7]. In all these cases jetting seems thus to be accomplished by a mechanism different from the one in this chapter.

In the case of drop impact [14] however, the formation of a cavity and its subsequent inertial collapse can be observed for certain parameter values and the present mechanism might be of relevance.

Our experimental setup consists of a circular disc with radius $R_0$ that is pulled through a water surface with velocity $V_0$ as described in [1]. The velocity $V_0$ is kept constant throughout the whole process. Global and local Reynolds and Weber numbers are fairly large as shown in [1] and therefore the only relevant control parameter is the Froude number, $\mathrm{Fr} = V_0^2/R_0 g$ with gravity $g$, which for our experimental conditions of $R_0 = 2\mathrm{cm}$ and $V_0 = 1\mathrm{m/s}$) equals 5.1.

## 2.2 Numerical results

We treat the problem as inviscid and irrotational. The inviscid assumption is justified by the large Reynolds numbers * together with the very short time scale of jet formation and irrotationality has been confirmed by detailed PIV measurements [15]. We thus make use of potential flow employing an axisymmetric boundary-integral technique which explicitly tracks the free surface. The topology change at pinch-off is implemented as follows: When the radial position of the node closest to the axis becomes smaller than the local node distance, the two neighboring nodes are shifted to the axis, conserving their vertical position and their potential. Continuing the simulation, these nodes eventually form the tip of the top and bottom jets. These numerical simulations have shown very good agreement with experiments for different impact geometries [1, 16] and we verified carefully that our results are independent of numerical parameters such as node density and time stepping. The influence of air is neglected.

Figure 2.1 shows the pinch-off of the impact cavity and the subsequent formation of two thin jets. We use polar coordinates with $z = 0$ at the pinch-off height and $t = 0$ at the pinch-off moment. Velocity, length, and time scales are normalized by $V_0$, $R_0$, and $T_0 = R_0/V_0$, respectively. As can be clearly appreciated from Fig. 2.1 surface tension is completely irrelevant for the present mechanism which is markedly different from the jetting mechanism suggested for Faraday waves [6, 7].

We set out to elucidate the precise mechanism which turns the horizontally collapsing cavity of Fig. 2.1 (a) into the thin vertical jets of Fig. 2.1 (b) and (c). For this we focus on the dynamics of the upward jet base defined as the local surface minimum illustrated in Fig. 2.2. It is remarkable how the geometric confinement of the narrow cavity forces the jet to move upwards very fast while the widening of its base is restricted by the collapsing walls. We find that jet formation occurs on an extremely short time scale: the jet grows above the initial quiescent surface in less than 1% of the total time after impact.

These high speeds, however, are not due to a hyperbolic flow around the original pinch-off point as one could have expected based on suggested jetting mechanisms in other situations [5–8]. Figure 2.3 demonstrates how the fluid here is not accelerated upwards continuously from the pinch-off singularity but instead acquires its large vertical momentum in a small zone located around the jet base: Since each horizontal cross-section of the axisymmetric cavity wall will keep flowing radially inwards even after pinch-off, eventually it must collide on the axis in a similar way as the

*After pinch-off one can additionally define $\mathrm{Re}_{\mathrm{jet}}$ using the width of the jet at its base and the local free surface velocity. Also this Reynolds number is $O(10^3)$.

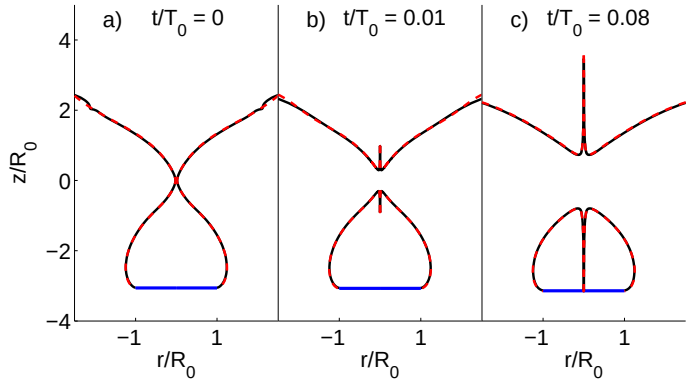


Figure 2.1: The free surface shape (black solid line) for simulations with surface tension ($\sigma = 72.8$ mN/m) and without surface tension (red dashed line) and the disc position (blue) from the simulation at pinch-off (a), at an intermediate time with the growing up- and downward jets (b) and at the instant when the downward jet hits the disc (c). As the free surface shapes lie almost exactly on top of each other we conclude that surface tension has no influence on the jet formation.

original pinch-off. This creates an upward and downward acceleration, of which the upward acceleration feeds the jet. The downward (negative) acceleration below the jet base can clearly be observed in Fig. 2.3. It is thus essential to consider not only the singularity itself but the continuous collapse of the entire cavity wall in any kind of theoretical modelling.

## 2.3 Analytical model

Inspired by the above observations we derive an analytical model for the jet formation: First, the flow field of the collapsing cavity before pinch-off will be described by a line of sinks along the axis of symmetry as in, e.g. [2, 3, 17]. The strength of these sinks will be determined from the simulation *at pinch-off* and forms the only input quantity for our model. Next, we will show how this picture naturally leads to a good description of the bulk flow after pinch-off. The line of sinks acquires a ”hole” between the two jets and an additional point sink emerges near the jet bases. Finally, we will obtain two differential equations for the widening and upward motion of the jet base which are the two most relevant processes for jet formation. Secondary processes as jet breakup and the precise dynamics of the jet tip are not considered

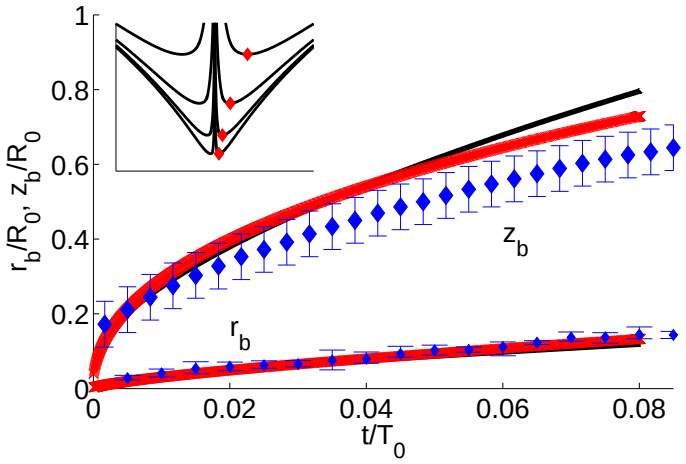


Figure 2.2: The inset illustrates the position of the jet base (red diamond) at different times. In contrast to other situations the vertical motion is much faster than the widening. The main figure shows the upwards motion $z_b(t)$ of the jet base derived from the analytical model (black line) which compares very favorably with simulation (red crosses) and experiment (blue diamonds). (The slightly slower motion in the experiment can be attributed to an imperfect axisymmetry reducing the radial focussing effect and thus slowing down the jet motion.) The agreement between model, experiment, and numerics is equally good for the base widening $r_b(t)$. The motion of $z_b$ is reminiscent to gas bubbles injected into water [4].

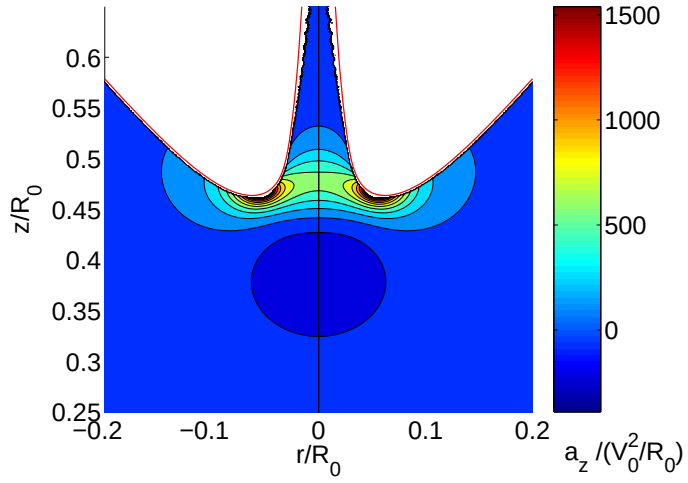


Figure 2.3: The vertical material acceleration $a_z = Dv_z/Dt$ at $t/T_0 = 0.028$ is confined to a small region around the jet base. The pinch-off location at (0,0) lies far too deep to influence the jetting process longer than in the first instants after pinch-off. The red line depicts the free surface. Note that as the boundary integrals diverge when the surface is approached no acceleration data is available immediately below the surface.

here.

As a starting point, Green's identity allows us to write the potential at any point $\mathbf{r}$ in the liquid bulk as an integral of sources and dipoles over the free surface:

$$4\pi\phi(\mathbf{r}) = \int_S dS'\mathbf{n}' \cdot \left[\frac{1}{|\mathbf{r}-\mathbf{r}'|}\nabla'\phi - \phi(\mathbf{r}')\nabla'\frac{1}{|\mathbf{r}-\mathbf{r}'|}\right] \tag{2.1}$$

with the integration taken over the free surface $S$ as illustrated in Fig. 2.4 (a) and (b). Since the dipole term decays quickly as $1/|\mathbf{r}-\mathbf{r}'|^2$, the source term (which decays only as $1/|\mathbf{r}-\mathbf{r}'|$) will be the dominant contribution to the integral if the observation point is chosen sufficiently far from the free surface. As the cavity close to pinch-off becomes slender, $\partial\phi/\partial n \approx -\dot{R}$ for a point $R$ on the free surface. Since the surface has no overhangs we write $dS = 2\pi R dz$. Approximating the radial distance as $r - r' \approx r$ turns Eq. (2.1) into [2, 3]:

$$2\phi(r,z,t) = \int \frac{q_{\text{axis}}(z',t)}{\sqrt{r^2+(z-z')^2}}dz'. \tag{2.2}$$

with a time- and height-dependent line distribution of sinks $q_{\text{axis}}(z,t) = -R\dot{R}$ along the axis of symmetry. Keeping in mind the extremely short time scale of jet formation as compared to the cavity collapse, we can assume the sink strength to remain *constant in time* from the moment of pinch-off $t_c$ onwards, $q_c(z) = q_{\text{axis}}(z,t_c)$.

During jet formation we divide the free surface into two regions separated by the jet base. The outer region contains the collapsing cavity until the jet base, while the inner region extends from the base inwards to the axis of symmetry as sketched in Fig. 2.4 (b). The principal fluid motion in the outer region remains identical to the collapsing cavity before pinch-off. High up in the jet, the motion will be vertically upwards with negligible radial velocity and thus will not contribute to the integral Eq. (2.2). As a free surface fluid element travels through the jet base and further up into the jet, it transitions from one flow regime to the other by decelerating its initial radial motion and turning it into vertical momentum. Thereby, its contribution to the integral (2.2) decays to a negligible amount. This decay of the sink strength cannot happen instantaneously which leads to an accumulation (see Fig. 2.4) of sinks around the jet base and a corresponding inward motion in that area. The length over which the sinks decay and accumulate must be proportional to the radius of the jet base which is the only relevant local length scale, $Cr_b$, with $C$ a constant of order one. This accumulation of sinks makes the dynamics qualitatively different from the collapsing cavity before pinch-off as in [2, 3, 17] and is crucial for the emergence of the high-speed jet. Note that our model is constructed only for the bulk flow outside

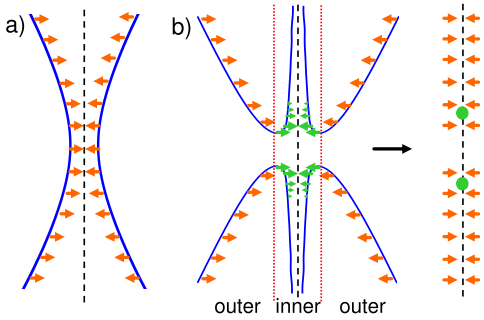


Figure 2.4: (a) Sketch of the collapsing cavity being described by a distribution of sinks (orange arrows; lengths are not representative of sink strength) on its free surface. (b) During jet formation the cavity collapse in the outer region remains unchanged (orange arrows) while around the jet base sinks accumulate (green arrows). This can be approximated as a line of sinks along the axis of symmetry plus a point sink (green dot). In the central region around the pinch-off point, a hole is formed: sinks are completely absent. For a detailed description see the main text.

the actual jet. The sinks on the axis thus always remain outside of the liquid domain which they aim to describe.

From an observation point at $r \gg r_b$, the contribution of the sinks accumulating around the base is seen as a point sink of strength $Cr_b q_c(z_b)$ since $q_c(z) \approx q_c(z_b)$ along the length $Cr_b$. The point sink is located some distance above the base which is again proportional to the local length scale, i.e., $z_{\text{sink}} = z_b + C_{\text{sink}} \cdot r_b$ introducing a second constant $C_{\text{sink}}$ of order unity. The exact value of the constants needs to be determined by fitting to the numerical and experimental data and depends on the Froude number.

Similarly, the most relevant contribution of the outer region will be that part of the integral closest to the observation point $\mathbf{r}$. At an altitude similar to or lower than the base, this is the region close to the base where again $q_c(z) \approx q_c(z_b)$. To allow analytical treatment of the integral from Eq. (2.2), we can thus at any given time assume a sink strength being *constant in space* along the entire axis above the base. Through the motion of the base this sink strength depends implicitly on time $q_b(t) = q_c(z_b(t))$.

Combining the approximations of the preceding paragraphs, we are now able to give an analytical expression derived from Eq. (2.2) for the potential at any point ($r$,

$z$) as a function of the base position $r_b$ and $z_b$:

$$2\phi(r,z,t) = \underbrace{q_b(t)\int_{-\infty}^{\infty}\frac{dz'}{\sqrt{r^2+(z-z')^2}}}_{\text{collapsing cavity}} - \underbrace{q_b(t)\int_{-z_b(t)}^{z_b(t)}\frac{dz'}{\sqrt{r^2+(z-z')^2}}}_{\text{hole}} + \underbrace{\frac{Cq_b(t)r_b(t)}{\sqrt{r^2+(z-(z_b(t)+C_{\text{sink}}r_b(t)))^2}}}_{\text{point sink}}. \tag{2.3}$$

The initial sink distribution is obtained from the numerics by calculating $q_c(z) = -R\dot{R}$ along the surface just once *at pinch-off*. It forms the *only* input quantity required by our jetting model. Note that, as we are dealing with the upwards jet, the point sink for the downward jet is far away and can be neglected.

In order to derive the desired ODEs for $r_b(t)$ and $z_b(t)$ we apply the Bernoulli equation with zero pressure $\partial\phi/\partial t + |\nabla\phi|^2/2 = 0$ on the free surface, neglecting small hydrostatic contributions. We then employ Eq. (2.3) to obtain the first differential equation involving $\dot{r}_b(t)$ and $\dot{z}_b(t)$. The second ODE results from the kinematic boundary condition at the jet base which, since the base is a local minimum, reads $\partial\phi/\partial z = \partial z_b/\partial t$. This leads to a closed system of two ODEs. The calculations are presented in the appendix. With $C = 4.55$ and $C_{\text{sink}} = 0.63$ the agreement with simulations and experiment is remarkable as demonstrated by Fig. 2.2. We stress that the model requires as its only ingredient the sink strength distribution *at pinch-off*.

## 2.4 The surface layer

Finally, it is important to understand which region of the liquid bulk at pinch-off will eventually become ejected into the jet. This knowledge can be obtained from the numerical simulations by injecting a line of particles at the base of the jet, cf. Fig. 2.5 (a). Since the flow field is known for all times previous to particle injection, the tracers can be followed backwards to their origin at $t = 0$. The line of tracers injected at the final instant will yield the outer boundary of the fluid layer that, together with the free surface, delimitates the fluid volume from which the jet originates. While the radial extent of the fluid layer depicted in Fig. 2.5 (c) is of the order of the disc radius, its maximum thickness is only about $0.01 \cdot R_0$. Thus far, a similar surface layer has only been observed when jetting is directly caused by surface waves [11]. In the present case, the thinness of the layer is even more remarkable as it does not arise from a surface phenomenon but from the collapsing motion of the entire bulk liquid.

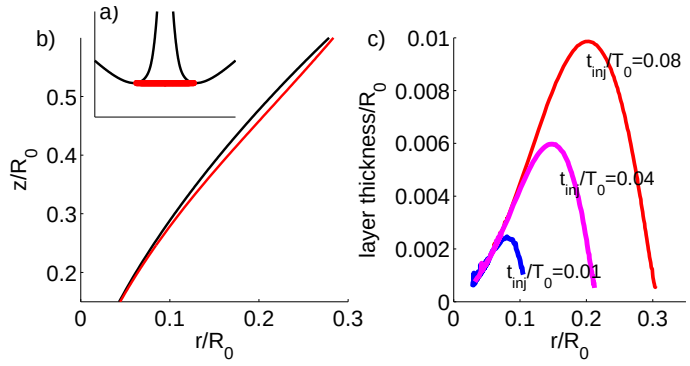


Figure 2.5: A line of tracer particles is injected at the base of the jet at $t_{\mathrm{inj}}/T_0 = 0.08$ (a). After advecting them backwards in time to the moment of pinch-off they form the border of a thin surface layer containing the liquid that eventually ends up in the jet (b). A corresponding movie can be found on the web [18]. (c) The thickness of the layer that has gone into the jet at three different times.

## 2.5 Conclusions

In conclusion, we have studied in detail the mechanism responsible for the formation of high-speed Worthington jets after the impact of solid objects on a liquid surface. We showed that the liquid forming the jet originates from a thin layer straddling the surface of the impact cavity. Our main finding, nevertheless, is the vital importance of the radial energy focussing *along the entire wall* of this cavity. In contrast to other situations [5–8], the hyperbolic flow around the singular pinch-off point turned out to be *not* the relevant mechanism behind jet formation. Instead, our case seems more reminiscent of the violent jets observed during the explosion of lined cavities [19]. We proposed an analytical model which is in very good quantitative agreement with experimental data and numerical simulations. The only ingredients to the model are two constants of order one and a sink distribution $q_c(z)$ describing the collapsing cavity *at pinch-off*.

We expect that the present mechanism is also responsible for the very thin jets ejected after the impact of water droplets on a liquid pool [14] in a parameter range where a small cylindrical cavity at the bottom of the crater collapses in a very similar fashion as the impact cavity described in this work. In the future, our model of jet formation can serve as the base for analyzing the shape and the velocity of the jet itself.

## Appendix: Differential equations for the jet base

Introducing a cut-off length scale $L \gg z$ and $L \gg r$ for the infinite integral in Eq. (2.3) of the main text, it may be integrated to yield the potential at any point $(r,z)$:

$$\begin{aligned}\phi(r,z,t) &= -q_b \ln\frac{r}{L} \\ &\quad -\frac{1}{2}q_b \ln\left(-z+z_b+\sqrt{r^2+(z-z_b)^2}\right) \\ &\quad +\frac{1}{2}q_b \ln\left(-z-z_b+\sqrt{r^2+(z+z_b)^2}\right) \\ &\quad +\frac{1}{2}\frac{Cq_b r_b}{\sqrt{r^2+(z-z_b-C_{\text{sink}}r_b)^2}},\end{aligned} \tag{2.4}$$

where the time dependence of $q_b(t)$, $r_b(t)$ and $z_b(t)$ is omitted for clarity. Further, we have approximated $\sqrt{\frac{r^2}{(z-L)^2}+1} \approx 1+\frac{1}{2}\frac{r^2}{(z-L)^2}$.

The dynamic boundary condition directly furnishes the first differential equation for $\dot{z}_b(t)$:

$$\begin{aligned}\dot{z_b} &= \frac{\partial\phi}{\partial z}|_{r=r_b,z=z_b} \\ &= \frac{q_b}{2r_b}+q_b\frac{-1+\frac{2z_b}{\sqrt{r_b^2+4z_b^2}}}{-4z_b+2\sqrt{r_b^2+4z_b^2}} \\ &\quad +\frac{1}{2}\frac{Cq_bC_{\text{sink}}}{r_b\left(1+C_{\text{sink}}^2\right)^{3/2}}.\end{aligned} \tag{2.5}$$

For the second boundary condition we pick an observation point $(r_{\text{obs}}, z_{\text{obs}})$ on the free surface. The radial coordinate is taken proportional to $r_b$ with a proportionality constant $\alpha$ in the range 1.2-1.5 (all values give similar results). Since this observation point is thus not located too far from the base and the free surface profile is rather flat around the jet base we can assume $z_{\text{obs}} \approx z_b$. Application of the Bernoulli equation at this observation point then gives

$$\frac{\partial\phi}{\partial t}+\frac{1}{2}|\nabla\phi|^2 = G+J\dot{z}_b+\frac{1}{2}\frac{Cq_b\dot{r}_b}{d_{\text{sink}}}-\dot{z}_bH-C_{\text{sink}}H\dot{r}_b = 0. \tag{2.6}$$

with the squared distance between the sink and the observation point

$$d_{\text{sink}} = \sqrt{r_{\text{obs}}^2+(z_{\text{obs}}-z_b-C_{\text{sink}}r_b)^2}, \tag{2.7}$$

the time derivative of the sink strength $\dot{q}_b = \frac{\partial q_b}{\partial z}\dot{z}_b$, and the terms independent of $\dot{r}_b$ and $\dot{z}_b$:

$$
\begin{aligned}
G &= -\dot{q}_b \ln\frac{r}{L} + \frac{1}{2}\dot{q}_b \ln\left(\frac{-z_{\rm obs}-z_b+\sqrt{r_{\rm obs}^2+(z_{\rm obs}+z_b)^2}}{-z_{\rm obs}+z_b+\sqrt{r_{\rm obs}^2+(z_{\rm obs}-z_b)^2}}\right) + \frac{1}{2}\frac{C\dot{q}_b r_b}{d_{\rm sink}} \\
&\quad + \frac{1}{2}\left[-\frac{q_b}{r_{\rm obs}} - \frac{1}{2}\frac{q_b r_{\rm obs}}{\sqrt{r_{\rm obs}^2+(z_{\rm obs}-z_b)^2}\cdot\left(-z_{\rm obs}+z_b+\sqrt{r_{\rm obs}^2+(z_{\rm obs}-z_b)^2}\right)}\right. \\
&\quad + \frac{1}{2}\frac{q_b r_{\rm obs}}{\sqrt{r_{\rm obs}^2+(z_{\rm obs}+z_b)^2}\cdot\left(-z_{\rm obs}-z_b+\sqrt{r_{\rm obs}^2+(z_{\rm obs}+z_b)^2}\right)} \\
&\quad \left. - \frac{1}{2}\frac{C q_b r_b r_{\rm obs}}{d_{\rm sink}^3}\right]^2 \\
&\quad + \frac{1}{2}\left[-\frac{1}{2}\frac{q_b\left(-1+\frac{z_{\rm obs}-z_b}{\sqrt{r_{\rm obs}^2+(z_{\rm obs}-z_b)^2}}\right)}{-z_{\rm obs}+z_b+\sqrt{r_{\rm obs}^2+(z_{\rm obs}-z_b)^2}} + \frac{1}{2}\frac{q_b\left(-1+\frac{z_{\rm obs}+z_b}{\sqrt{r_{\rm obs}^2+(z_{\rm obs}+z_b)^2}}\right)}{-z_{\rm obs}-z_b+\sqrt{r_{\rm obs}^2+(z_{\rm obs}+z_b)^2}}\right. \\
&\quad \left. - \frac{1}{2}\frac{C q_b r_b\left(z_{\rm obs}-z_b-C_{\rm sink} r_b\right)}{d_{\rm sink}^3}\right]^2 \\
J &= \frac{1}{2}q_b\left(\frac{-1+\frac{z_{\rm obs}-z_b}{\sqrt{r^2+(z_{\rm obs}-z_b)^2}}}{-z_{\rm obs}+z_b+\sqrt{r_{\rm obs}^2+(z_{\rm obs}-z_b)^2}} + \frac{-1+\frac{z_{\rm obs}+z_b}{\sqrt{r_{\rm obs}^2+(z_{\rm obs}+z_b)^2}}}{-z_{\rm obs}-z_b+\sqrt{r_{\rm obs}^2+(z_{\rm obs}+z_b)^2}}\right) \\
H &= -\frac{1}{2}\frac{C q_b r_b\left(z_{\rm obs}-z_b-C_{\rm sink} r_b\right)}{d_{\rm sink}^3}.
\end{aligned}
\tag{2.8}
$$

From Eq. (2.6) we can isolate $\dot{r}_b$ and substitute $\dot{z}_b$ from Eq. (2.5) to obtain the second ODE required to close the system. The initial conditions for the integration are provided by the cut-off radius and the size of the initial liquid bridge, whose values are however not important for the long-term behavior of the jet base as described in the next chapter.

# References

[1] R. Bergmann, D. van der Meer, M. Stijnman, M. Sandtke, A. Prosperetti, and D. Lohse, “Giant bubble pinch-off”, Phys. Rev. Lett. **96**, 154505 (2006).

[2] J. M. Gordillo and M. Pérez-Saborid, "Axisymmetric breakup of bubbles at high reynolds numbers", J. Fluid Mech. **562**, 303–312 (2006).

[3] J. Eggers, M. A. Fontelos, D. Leppinen, and J. H. Snoeijer, "Theory of the collapsing axisymmetric cavity", Phys. Rev. Lett. **98**, 094502 (2007).

[4] S. T. Thoroddsen, T. G. Etoh, and K. Takehara, "Experiments on bubble pinch-off", Phys. Fluids **19**, 042101 (2007).

[5] M. S. Longuet-Higgins, "Bubbles, breaking waves and hyperbolic jets at a free surface", J. Fluid Mech. **127**, 103–121 (1983).

[6] J. E. Hogrefe, N. L. Peffley, C. L. Goodridge, W. T. Shi, H. G. E. Hentschel, and D. P. Lathrop, "Power-law singularities in gravity-capillary waves", Physica D **123**, 183–205 (1998).

[7] B. W. Zeff, B. Kleber, J. Fineberg, and D. P. Lathrop, "Singularity dynamics in curvature collapse and jet eruption on a fluid surface", Nature **403**, 401–404 (2000).

[8] L. Duchemin, S. Popinet, C. Josserand, and S. Zaleski, "Jet formation in bubbles bursting at a free surface", Phys. Fluids **14**, 3000–3008 (2002).

[9] J. M. Boulton-Stone and J. R. Blake, "Gas bubbles bursting at a free surface", J. Fluid Mech. **254**, 437–466 (1993).

[10] J. R. Blake, P. B. Robinson, A. Shima, and Y. Tomita, "Interaction of two cavitation bubbles with a rigid boundary", J. Fluid Mech. **255**, 707–721 (1993).

[11] F. MacIntyre, "Bubbles: A boundary-layer "microtome" for micron-thick samples of a liquid surface", J. Phys. Chem. **72**, 589–592 (1968).

[12] S. T. Thoroddsen, T. G. Etoh, and K. Takehara, "Microjetting from wave focussing on oscillating drops", Phys. Fluids **19**, 052101 (2007).

[13] A. Antkowiak, N. Bremond, S. L. Dizès, and E. Villermaux, "Short-term dynamics of a density interface following an impact", J. Fluid Mech. **577**, 241–250 (2007).

[14] M. Rein, "Phenomena of liquid drop impact on solid and liquid surfaces", Fluid. Dyn. Res. **12**, 61–93 (1993).

[15] R. Bergmann, D. van der Meer, S. Gekle, A. van der Bos, and D. Lohse, "Controlled impact of a disc on a water surface: Cavity dynamics", J. Fluid Mech. **633**, 381–409 (2009).

[16] S. Gekle, A. van der Bos, R. Bergmann, D. van der Meer, and D. Lohse, "Noncontinuous froude number scaling for the closure depth of a cylindrical cavity", Phys. Rev. Lett. **100**, 084502 (2008),
*See Chapter 7 of this thesis.*

[17] M. S. Longuet-Higgins, B. R. Kerman, and K. Lunde, "The release of air bubbles from an underwater nozzle", J. Fluid Mech. **230**, 365–390 (1991).

[18] See EPAPS Document No. E-PRLTAO-102-014905 for supplementary material. For more information on EPAPS, see http://www.aip.org/pubservs/epaps.html.

[19] G. D. Birkhoff, D. P. MacDonald, W. M. Pugh, and G. I. Taylor, "Explosives with lined cavities", J. Appl. Phys. **19**, 563–582 (1948).

# 3

# Generation and breakup of Worthington jets after cavity collapse *

*Helped by the careful analysis of their experimental data, Worthington and coworkers described, almost a century ago, roughly the mechanism underlying the formation of high-speed jets ejected after the impact of an axisymmetric solid on a liquid-air interface. They made the fundamental observation that the intensity of these sharp jets was intimately related to the formation of an axisymmetric air cavity in the wake of the impactor. In this work we combine detailed boundary-integral simulations with analytical modeling to describe the formation and break-up of such Worthington jets in two common physical systems: the impact of a circular disc on a liquid surface and the release of air bubbles from an underwater nozzle. We first show that the jet base dynamics can be described for both systems using our earlier model in Chapter 2. Nevertheless, our main point here is to present a model which allows us to accurately capture the shape of the entire jet. In our model, the flow structure inside the jet is divided into three different regions: The axial acceleration region, where the radial momentum of the incoming liquid is converted into axial momentum, the ballistic region, where fluid particles experience no further acceleration and move constantly with the velocity obtained at the end of the acceleration region and the jet tip region where the jet eventually breaks into droplets. Good agreement with numerics and*

*Submitted as: Stephan Gekle and José Manuel Gordillo, "Generation and breakup of Worthington jets after cavity collapse", J. Fluid Mech. (2009).

*some experimental data is found. Moreover we find that, contrarily to the capillary breakup of liquid cylinders in vacuum studied by Lord Rayleigh (1878), the breakup of stretched liquid jets at high values of both Weber and Reynolds numbers is not triggered by the growth of perturbations coming from an external source of noise. Instead, the jet breaks up due to the capillary deceleration of the liquid at the tip which produces a corrugation to the jet shape. This perturbation, which is self-induced by the flow, will grow in time promoted by a capillary mechanism. Combining these three regions for the base, the jet, and the tip we are able to model the exact shape evolution of Worthington jets ejected after the impact of a solid object - including the size of small droplets ejected from the tip due to a surface-tension driven instability - using as the single input parameters the minimum radius of the cavity and the flow field before the jet emerges.*

## 3.1 Introduction

The impact of a solid object against a liquid interface is frequently accompanied by the ejection of a high speed jet emerging out of the liquid bulk into the air. Figure 3.1, which shows the effect of a horizontal disc that impacts on a pool of water, illustrates a liquid jet which flows $\sim 20$ times faster than the disc impact speed. The qualitative description of this common and striking phenomenon was firstly elucidated at the beginning of the twentieth century by [1, 2]. Through the careful analysis of the photographs taken after a solid sphere was dropped into water, [1, 2] realized that these type of liquid threads emerge as a consequence of the hydrostatic collapse of the air-filled cavity which is created at the wake of the impacting solid. [1, 2] also made the remarkable observation that the generation of such cavities was very much influenced by the surface properties of the spherical solid. One century after their original observations, [3] quantified the conditions that determine the existence of the air cavity in terms of the surface properties of the solid and the material properties of the liquid.

High speed jets emerging out of a liquid interface are also frequently observed in many other situations. For instance, it is very usual to perceive that the liquid "jumps" out of the surface of sparkling drinks, a fact which is known to happen as a consequence of bubbles bursting at the liquid interface [4–6]. Similarly, the impact of a drop on a liquid interface or solid surface [7–12], is commonly accompanied by the ejection of liquid jets whose velocities can be substantially larger than that of the impacting drop. Less familiar situations such as those related to the focussing of capillary [13, 14] or Faraday waves [15, 16] also give rise to the same type of phenomenon. Nevertheless, in spite of the clear analogies, the main difference between

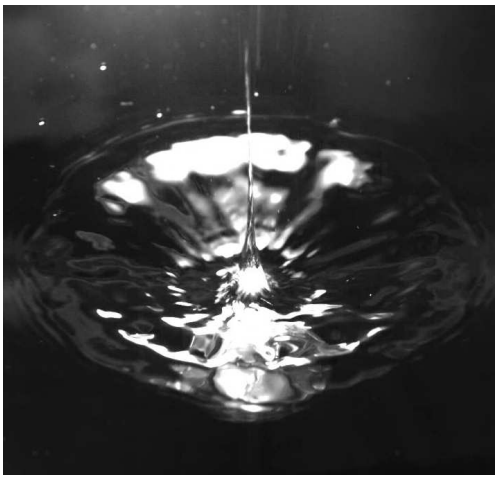

Figure 3.1: Image of the high-speed jet ejected after the impact of 2cm disc with 1 m/s on a quiescent water surface.

the situations enumerated above and the case of jet formation after cavity collapse is that, in the latter case, surface tension does not play any role in the jet ejection process [17]. Indeed, the type of Worthington jets to be described here depend on a purely inertial mechanism, namely the radial energy focussing along the narrow cavity wall right before the cavity pinches-off. This fact makes our process also somewhat different from situations in which jets are induced by pressure waves [18–21].

Moreover, contrarily to what could be expected from the analogy with other related physical situations [22, 23], [17] pointed out that jets formed after cavity collapse are not significantly influenced by the hyperbolic type of flow existing at the pinch-off location. Instead, the description of this type of jets shares many similarities with the very violent jets of fluidized metal which are ejected after the explosion of lined cavities (e.g. [24]), with those formed when an axisymmetric bubble collapses inside a stagnant liquid pool [25, 26] or possibly even with the granular jets observed when an object impacts a fluidized granular material [27, 28].

Most of the results presented here refer to the perpendicular impact of a circular disc with radius $R_D$ and *constant* velocity $V_D$ against a liquid surface. The fact that the solid is a disc instead of a sphere leads to the formation of an air cavity which is attached at the disc periphery, independent of the surface properties. Thus, this choice for the solid geometry avoids the additional difficulty of determining the position of the void attachment line on the solid surface. The differences pointed out above set our system somewhat apart from similar studies [29, 30]. The experimental

realization of the setup to which the numerical simulations presented are referred, is described by [17, 31–33], who show that boundary-integral simulations are in very good with experiments. In addition, potential flow numerical simulations to study of the type of Worthington jets ejected after bubble pinch-off from an underwater nozzle sticking into a quiescent pool of water [25, 26, 34–43] are also reported in this chapter. As in the case of Worthington jets ejected after solid body impact, similar boundary-integral simulations have been shown to be in very good agreement with experiments see [26, 35].

This chapter is organized as follows: In Section 3.2 we present the three different numerical methods used. Section 3.3 presents the results from the simulations which are compared to the analytical model in Section 3.4. Conclusions are drawn in Section 3.5.

## 3.2 Numerical methods

In this chapter we have used three types of boundary-integral simulations. The first two model, respectively, the normal impact of a disc on a free surface and the pinch-off of a bubble from an underwater nozzle. With the purpose of simulating the capillary breakup of the jets formed in the first two situations, the third type of simulation represents a jet issued from a constant-diameter nozzle with an imposed axial strain rate. The latter type of numerical simulations have the advantage of allowing us to directly impose the values of both the strain rate and the Weber number, which are the parameters controlling the breakup of the jet, as will become clear from the discussion below. All simulations include surface tension.

### 3.2.1 Disc impact simulations

The process of disc impact see also [17, 31, 32] is illustrated in Fig. 3.2: after impact a large cavity is created beneath the surface which subsequently collapses roughly at its middle due to the hydrostatic pressure from the liquid bulk. From the closure location two high-speed jets are ejected up- and downwards. Here positions, velocities and time are made dimensionless using as characteristic quantities the disc radius $R_D$, the impact velocity $V_D$, and $T_D = R_D/V_D$, respectively. (Variables in capital letters will be used to denote dimensional quantities whereas their lower case analogs will indicate the corresponding dimensionless variable). Moreover, it will be assumed that axisymmetry is preserved and, thus, a polar coordinate system $(r,z)$ will be used. The origins of both the axial polar coordinate $z$ and of time $t$ are set at the cavity pinch-off height and at the pinch-off instant, respectively.

Since global and local Reynolds numbers are large and the generation of vorticity is negligible [17, 32] we can make use of a flow potential to describe the liquid flow field. The numerical details, including the "surface surgery" needed to accurately capture the transition from the cavity collapse process to the jet ejection, are given elsewhere [17, 32]. These simulations have shown very good agreement with experimental high-speed recordings and particle image velocimetry measurements [17, 31–33]. The simulation stops when the downward jet hits the disc surface.

Since the Reynolds number is large, the dimensionless parameters controlling the jet ejection process are the Froude number, $\mathrm{Fr} = V_D^2/(R_D\, g)$, and the Weber number, $\mathrm{We} = \rho V_D^2 R_D/\sigma$ where $g$, $\rho$ and $\sigma$ indicate the gravitational acceleration, the liquid density and the interfacial tension, respectively. Since $\mathrm{We} \gtrsim O(10^2)$ in all cases considered here, the jet ejection is not promoted by surface tension [17] which nevertheless is included in the simulations. The exact dynamics of the jet tip and its breakup can – for the impacting disc – not be predicted by the present simulations since the jet is so thin that eventually numerical instabilities arise at its tip which have to be removed. Air effects, which play an essential role during the latest stages of cavity collapse [42, 44, 45], are not taken into explicit consideration here. Instead the cut-off radius at which the cavity geometry is changed into the jet geometry is fixed manually verifying carefully that the exact value of this parameter does not influence our results. The only consequence of this simplification is that a tiny fraction of the jet - the jet tip - may not be accurately described neither by our numerical simulations nor by our theory as will be discussed in Section 3.3.1.

### 3.2.2 Bubble pinch-off from an underwater nozzle

In the second type of simulations a bubble grows and detaches when a constant gas flow rate is injected from an underwater nozzle into a quiescent pool of liquid. [25] and [26] experimentally showed that this process also creates high speed jets. Indeed, as the bubble grows in size, the neck becomes more and more elongated and, eventually, surface tension triggers the pinch-off of the bubble, leading to the formation of two fast and small jets as illustrated in Fig. 3.3. Surface tension also leads to the pinch-off of a small droplet at the jet tip, which is precisely the instant when the simulation stops.

Here, distances are made non-dimensional using the nozzle radius $R_N$ as the characteristic length scale; moreover, the prescribed gas flow rate $Q$ is used to derive the typical time scale $T_N = (\pi R_N^3)/Q$. For the quasi-static injection conditions considered here, the relevant dimensionless parameter characterizing this physical situation is the Bond number $\mathrm{Bo} = \rho R_N^2 g/\sigma$ [26, 34], which in the case presented here equals 2.1. More details of the simulation method are given in [35, 46]. Note that the present

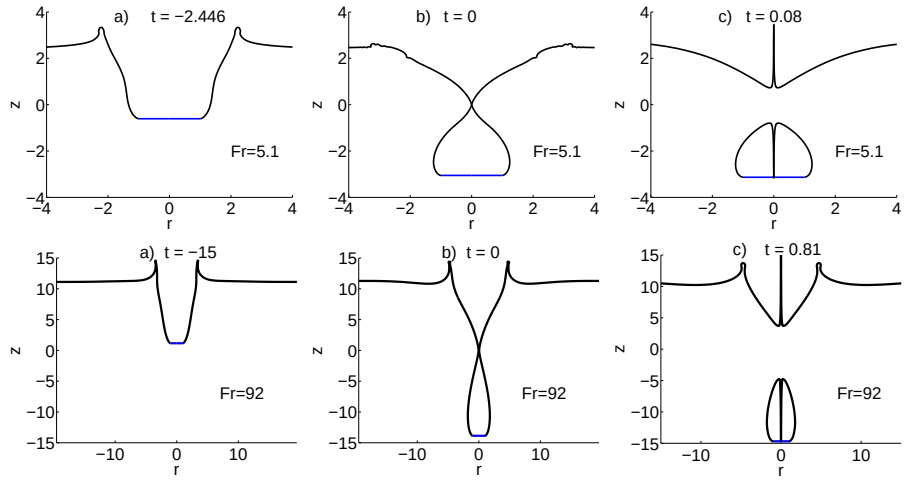


Figure 3.2: Numerical results obtained when a circular disc (blue line) impacts perpendicularly and at constant velocity on a flat liquid interface. Upon impact a cavity attached at the disc periphery is created in the liquid (a) which collapses under the influence of hydrostatic pressure (b). As a consequence of the cavity collapse, two jets with velocities much larger than that of the impact solid, are ejected upwards and downwards. The influence of increasing the impact Froude number from $\mathrm{Fr} = 5.1$ – top row – to $\mathrm{Fr} = 92$ - bottom row - is that the cavity becomes more slender.

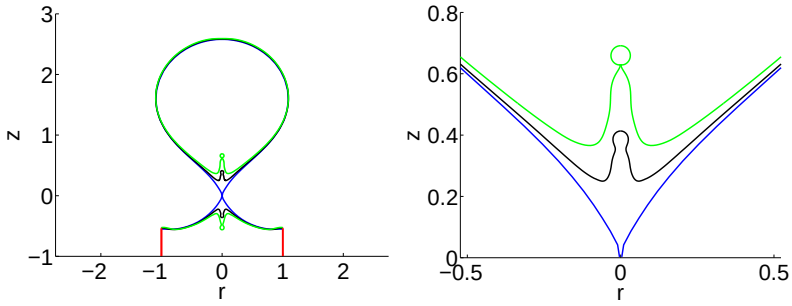


Figure 3.3: (a) Time evolution of jets formed after the collapse of gas bubbles injected into a quiescent liquid pool through a nozzle (red line), showing the ejection of the first drop, for Bo = 2.1. b) Closeup view of the jet region in (a). The colors correspond to different dimensionless times: $t = 0$ (blue), $t = 0.0014$ (black) and $t = 0.0027$ (green)

.

numerical simulations give the same results as those in [35] which are in good agreement with experiments [35].

### 3.2.3 Simulations of a jet ejected at constant diameter

As will be shown by our theoretical analysis below, the jet breakup process can be described in terms of two dimensionless parameters evaluated nearby the base of the jet, namely, the local Weber number and the dimensionless axial strain rate. These quantities depend non-trivially on the input parameters of our physical simulations (disc speed, nozzle size etc.). In order to obtain a way of systematically varying both the local Weber number and strain rate we conducted a third type of simulation by adapting the axisymmetric (two-fluid) boundary integral method described in [40] to a situation that retains the essential ingredients to describe the capillary breakup process in the first two types of simulations. For this purpose, we have simulated the discharge of a liquid injected through a constant radius needle with a length of 20 times its radius into a gaseous atmosphere. The density ratio of the inner and outer fluids is $10^3$ and a uniform velocity profile linearly decreasing with time is imposed on the boundary that delimits the computational domain on the left (see Fig. 3.4). Initially, the liquid interface is assumed to be a hemisphere attached at the nozzle tip. The uniform velocity with which the liquid is injected varies in time according to

$$U_N(t_N) = U_N(0)(1 - \alpha t_N) \tag{3.1}$$

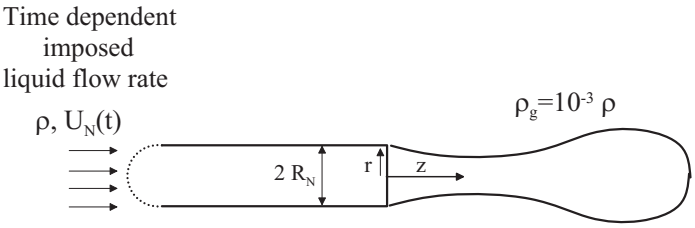


Figure 3.4: Sketch defining the geometry of the numerical simulations used to describe the capillary breakup of a stretched liquid jet of density $\rho$ injected into a gaseous atmosphere of density $\rho_g = 10^{-3}\rho$. The liquid velocity profile imposed at the boundary which delimits the nozzle on the left is uniform and decreases linearly with time.

with the dimensionless strain rate $\alpha$ and the initial velocity $U_N(0)$ determined by the physical situation which one intends to imitate (jets formed either after the disc impact or from the underwater nozzle). For these type of simulations positions, velocities and time will be made non dimensional using, as characteristic dimensional quantities, the injection needle radius $R_N$, the initial velocity $U_N(0)$, and $T_N = R_N/U_N(0)$ respectively.

In Section 3.3.4 we demonstrate very good agreement between the results of these type of simulations and those related to the formation of jets after bubble pinch-off from an underwater nozzle. Unfortunately, the extremely large values of the Weber number reached at the tip of the liquid jets formed after the impact of a disc on a free surface ($\sim O(10^3)$) unavoidably lead to the development of numerical instabilities [19]. This fact makes a direct comparison between the simulations of the axial strain system sketched in Fig. 3.4 and those corresponding to the impacting disc impossible.

## 3.3 Analysis of numerical results

### 3.3.1 Effects of azimuthal asymmetries in the determination of the cut-off radius

The value of $r_{min}$ (the minimum radius of the cavity before the jet emerges) would be zero under the ideal conditions of our simulations. This would imply that the initial jet velocity would be infinity. In reality, effects such as gas flow [41, 42, 44, 45], liquid viscosity [36, 38, 47], or small azimuthal asymmetries [37, 43] are known to strongly influence the spatial region surrounding the cavity neck during the very last stages of bubble pinch-off and, therefore, are essential to determine the real value of

$r_{min}$ ([42, 45]).

Note first that, the larger $r_{min}$ is, the smaller will be the maximum liquid velocity at the tip of the jet. Here we will provide experimental evidence showing that non-axisymmetric perturbations are of crucial importance to fix $r_{min}$ and, consequently, the maximum velocity reached by the jet. This is due to the fact that asymmetries influence the radial flow focussing effect on the central axis even before the actual cavity closure. The development of azimuthal instabilities leads to a decrease of the liquid acceleration towards the axis before pinch-off and thus reduces the speed of the ejected jet. This is clearly observed in Figs. 3.5 and 3.6, which show the cavity formation and jet ejection processes when either a brass disc (smooth surface) or a golf ball (structured surface) impact perpendicularly on a quiescent pool of water. Despite the fact that both the velocity and the diameter of the ball are larger than those of the disc, the maximum jet velocity is larger for the disc case. Indeed, while the shape of the cavity in Fig. 3.5 is smooth, the cavity interface in Fig. 3.6 clearly exhibits asymmetric modulations already right after the impact (which – in addition to the rough surface structure – may in part also be due to a rotation of the ball). Note that the overall shape of the cavity is very similar in both cases. Consequently, since the self-acceleration of the liquid towards the axis is lost when the amplitude of azimuthal disturbances is similar to the radius of the cavity, the maximum velocity reached during the collapse process decreases when the cavity interface is not smooth. Note that Figs. 3.5 and 3.6 are representative of an exhaustive set of experiments. The analysis of the whole experimental data has shown that the rough surface systematically produces lower jet speeds.

The initial amplitude or the precise instant at which such azimuthal instabilities may develop is not easy to predict. For instance, [37, 43] pointed out that tiny geometrical asymmetries in the initial setup might break the cylindrical symmetry of the cavity at the pinch-off location. Moreover, even if the cavity is perfectly axisymmetric, the strong shear between the gas and the liquid will induce instabilities that tend to break the cylindrical symmetry of the cavity [31, 48].

Therefore, the precise determination of $r_{min}$ is a very complex and difficult subject which in addition will heavily depend on the system under study and must therefore remain outside the scope of this contribution. We have instead decided to vary $r_{min}$ within reasonable bounds and to analyze carefully the effect on the subsequent time evolution of the jet. It can be clearly appreciated in Fig. 3.7 that differences in the simulations can be observed in both the jet base and tip region right after pinch-off occurs. However, as soon as the jet radius at its base becomes of the order of the maximum value of $r_{min}$ explored, differences in the jet base region disappear and only remain appreciable in the jet tip region. Physically, this means that gas effects

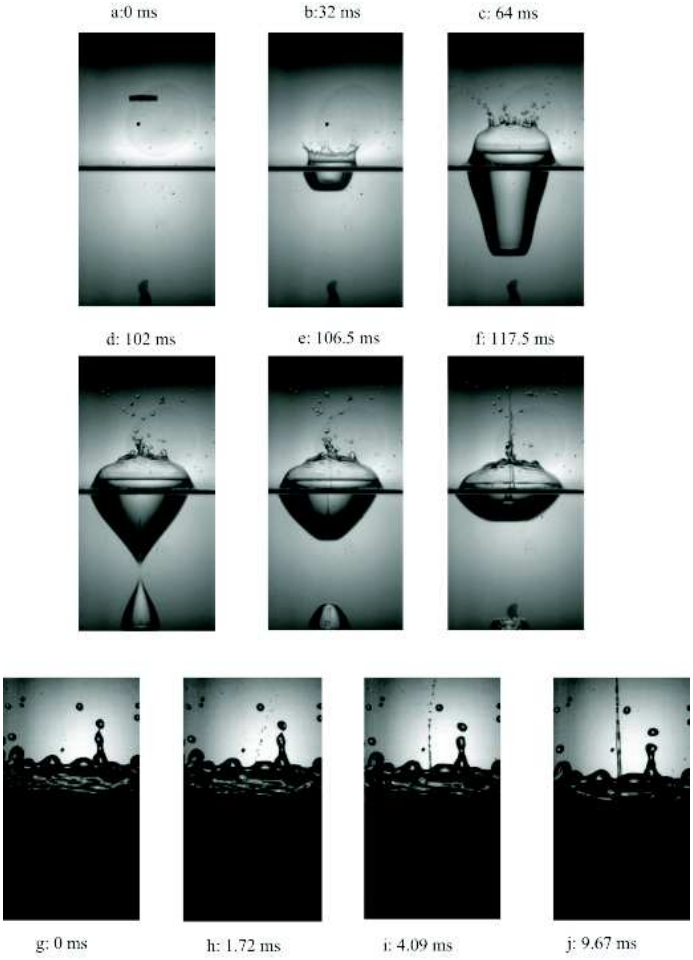


Figure 3.5: Pictures (a)-(f) show the smooth cavity formed after the normal impact of a brass disc against a water interface. The disc dimensions are 22 mm in diameter and 4.7 mm in height. The disc falls by gravity and the impact velocity is $V_{\text{impact}} = 1.85$ m/s. Note that, while the time between impact and cavity closure is roughly 70 ms, the upwards jet reaches the free surface in less than 4 ms, indicating that the jet velocity is much larger than the impactor's velocity. Indeed, the initial velocity of the tip of the jet, measured from detailed images of the type (g)-(j), is larger than – since drops might not be in a plane perpendicular to the free surface – 22.71 m/s and thus larger than 12.28 times the disc velocity. The huge velocities reached by the liquid jet can also be visually appreciated by comparison with the velocity of the drops formed in the corona splash which hardly change their position between images (g) and (j). Let us also remark that, initially, the jet is not axisymmetric ((h) and (i)). Nevertheless, after a few milliseconds, picture (j) shows that the jet becomes approximately axisymmetric.

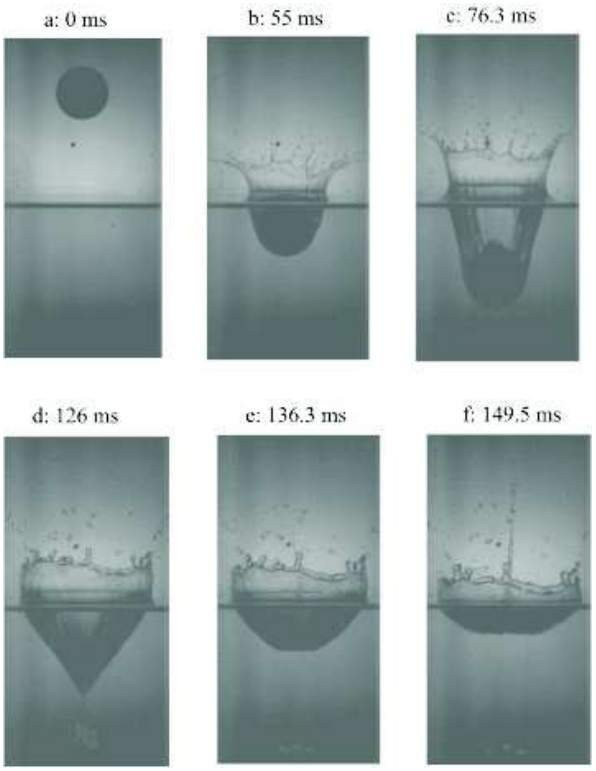


Figure 3.6: Pictures (a)-(f) show the cavity formation caused by a golf ball with a diameter of 42.75 mm impacting with a velocity of 2.03 m/s. Compared to Fig. 3.5 the surface shape is visibly distorted (c) due to the rough surface structure of the ball. Nevertheless, it can be inferred from a detailed image analysis that the jet velocity is again much larger than the ball's velocity. However, in spite of both the impact velocity and the ball diameter being larger than those of the disc, the maximum velocity of the jet is only $V_{\text{impact}} \simeq 20$ m/s and thus smaller than for the impacting disc.

and small asymmetries will only be felt at the highest part of the jet, which represents only a very small fraction of both the total volume and of the total kinetic energy of the jet. Note also that, in spite of the jet tip being the spatial region where the highest velocities are reached, it is also the least reproducible one from an experimental point of view since it strongly depends on the precise details of pinch-off. Thus, regarding experimental reproducibility, our study will be valid to accurately describe the most robust part of the jet. In the case of the impacting disc we will set $r_{min} = 0.01$ and in the case of the gas injection needle, the minimum radius will be fixed to $r_{min} = 0.05$.

Finally, note that our axisymmetric approach has been proven to be in good agreement with experiments whenever either the radius of the collapsing cavity or the radius of the emerging jet, are larger than the cut-off radius $r_{min}$ for which any of the effects enumerated above – gas, azimuthal perturbations – become relevant (see, for instance, [17, 26, 31, 33, 47]).

### 3.3.2 Jet ejection process for the disc impact

The different stages of the jet formation process have been illustrated in Fig. 3.2. After the solid body impacts against the free surface, an air cavity is generated (a). As a consequence of the favorable pressure gradient existing from the bulk of the liquid to the cavity interface, the liquid is accelerated inwards (b). These radially inward velocities focus the liquid towards the axis of symmetry, leading to the formation of two fast and sharp fluid jets shooting up- and downwards, as depicted in Fig. 3.2 (c). Here we will mainly focus on the detailed description of the upwards jet and demonstrate that the downward jet can be treated in the same way.

From Fig. 3.2, observe that impacts with larger Froude numbers lead to more slender cavities and also increase the non-dimensional depth at which the cavity pinches-off. Furthermore, it can be appreciated that the jets are extremely thin and that the time needed for the tip of the jet to reach the free surface is only a small fraction of the pinch-off time. This latter observation means that the jets possess a much faster velocity than the velocity of the impacting solid, a conclusion which was also extracted from the analysis of the experiments in Figs. 3.5-3.6. Motivated by this striking fact, one of the main objectives in this chapter will be to address the following question: what is the relationship between the impact velocity $V_D$ - or, in dimensionless terms, between the Froude number - and the liquid velocity within the jet?

With this purpose in mind, it will prove convenient to define first the length scale that characterizes the jet width. In [17] we showed that the time evolution of the jet is a *local* phenomenon, independent of the stagnation-point type of flow generated after pinch-off at the location where the cavity collapses. Therefore, this characteristic

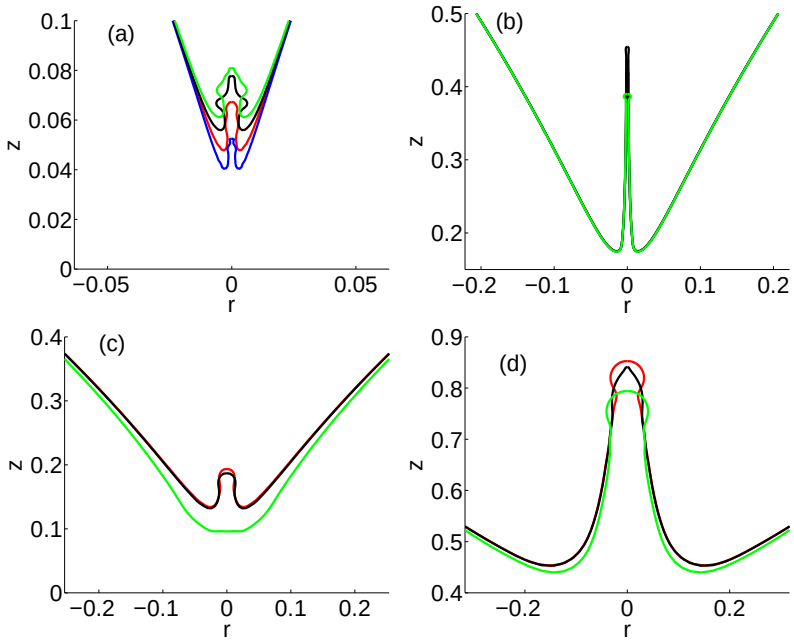


Figure 3.7: Top row: Jet shapes for the disc impact at Fr= 5.1 at two different instants of time, $t = 10^{-4}$(a) and $t = 3.2 \times 10^{-3}$ (b), for four different values of the cut-off radius, $r_{min} = 0.005$ (blue), $r_{min} = 0.01$ (red), $r_{min} = 0.02$ (black), and $r_{min} = 0.05$ (green). Bottom row: Jet shapes for the underwater nozzle with different cut-off radii (colors as in top row) at $t = 0.0003$ (c) and $t = 0.004$ (d), respectively (here the simulations are extended beyond the ejection of the first droplet). It is evident in both cases that the influence of varying the cut-off is significant only in the very first instants after pinch-off and at the very tip of the jet.

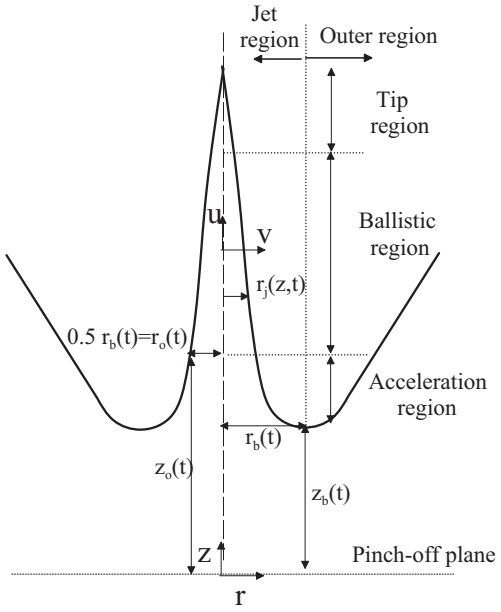


Figure 3.8: Sketch showing the different lengths used to define the jet base and the regions of the jet. The jet base $(r_b, z_b)$ is located where the interface possesses a local minimum. The outer region covers the bulk of the fluid with $r > r_b$ and $z < z_b$. The jet region is subdivided into the acceleration, the ballistic and the tip region. Note that, in the following, $u$ and $v$ will be used to denote axial and radial velocities, respectively

length needs to be related to a *local* instead of a global quantity and, following [17], we choose the radial position at which the interface possesses a local minimum i.e., the radius $r_b(t)$ indicated in Fig. 3.8. We shall in the following call this point the *jet base* and denote its vertical position by $z_b(t)$.

To clearly show the spatial region surrounding the jet base, some of the different jet shapes taken from the time evolutions of Fig. 3.2, are translated vertically so that they share a common vertical origin, as depicted in Fig. 3.9. Note that both the jet base and the jet itself widen as the time from pinch-off increases. Interestingly enough, Fig. 3.10 shows that jet shapes exhibit some degree of self-similarity since they nearly collapse onto the same curve when distances are normalized using $r_b$. This fact indicates that $r_b$ is not an arbitrary choice, but a relevant local length that plays a key role in the dynamics of the jet. The same arguments hold for the downward jet as illustrated in Fig. 3.11.

In order to model the full process of jet ejection and break-up we divide the liquid

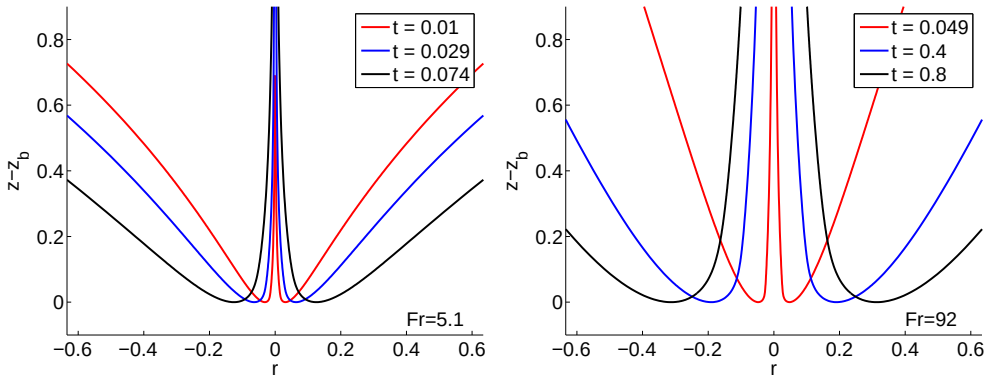


Figure 3.9: Jet shapes translated vertically for different instants of time and different values of the impact Froude number.

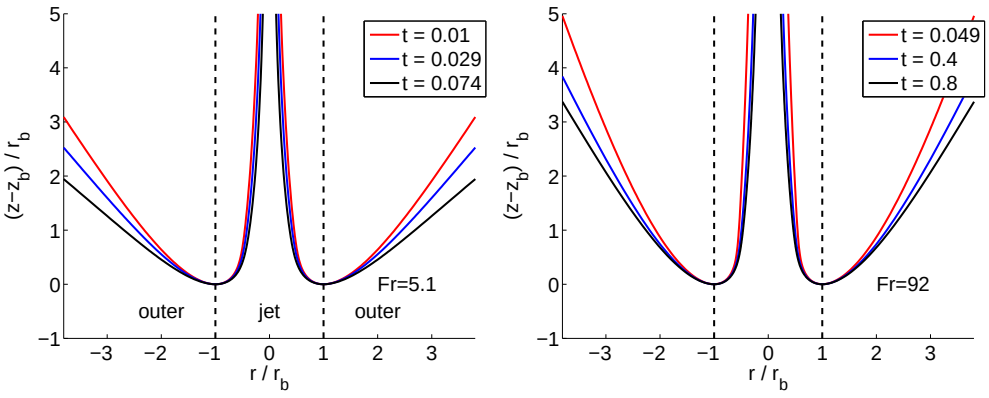


Figure 3.10: Shapes of the jets depicted in Fig. 3.9 when distances are normalized using $r_b$ overlay reasonably well indicating that $r_b$ is a good choice for the characteristic local length scale. The definition of the outer and jet regions is also indicated.

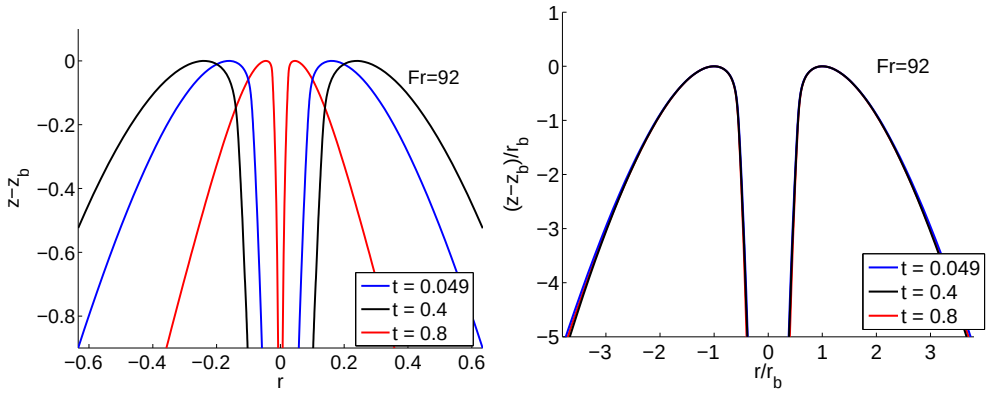


Figure 3.11: Jet shapes for the downward jet at Fr=92 taken at the same times as in Figs. 3.9 and 3.10 show a similarly good rescaling with the corresponding base radius $r_b$.

flow field into two different regions: the outer region, defined for $r > r_b$, $z < z_b$ and the jet region, extending from the jet base to the axis i.e, $r < r_b$ and $z \geqslant z_b$, as illustrated in Fig. 3.10. The jet region is further divided into three different axial subregions: the *acceleration region*, the *ballistic region* and the *tip region* as illustrated in Fig. 3.8.

Figure 3.12 shows that $z_b(t) \gg r_b(t)$. These comparatively large values of $z_b(t)$ with respect to $r_b(t)$ are caused by the confinement of the jet by the cavity walls, which inhibits the widening of the base radius. Moreover, the small values of $r_b$ are responsible for the large axial velocities within the jet (and, thus, for the large values of $dz_b/dt$) since, as it will become clear below, vertical velocities are inversely proportional to $r_b$.

The importance of local processes around the jet base is even more clearly illustrated in Fig. 3.13 where both the axial and radial velocities evaluated at the jet air/liquid interface, $u$ and $v$ respectively, are represented for different instants of time. In this figure one can observe that while the axial velocities are of similar magnitude as the radial velocities at $r = r_b$, they monotonically increase to much higher values as the jet radius diminishes. Contrarily, the modulus of the (negative) radial velocities decays from $\sim O(10)$ at $r = r_b$ to almost zero at $r \simeq 0.5\, r_b$ and, therefore, the radial inflow experiences a strong deceleration in the *small* distance $\sim 0.5 r_b$. Since the liquid is at atmospheric pressure at the free surface of the jet, the strong radial deceleration provokes an overpressure below the jet base. Accordingly, a strong favorable *vertical* pressure gradient is created and, therefore, the liquid experiences a large upwards acceleration in the vertical direction, creating the high speed jet ejected

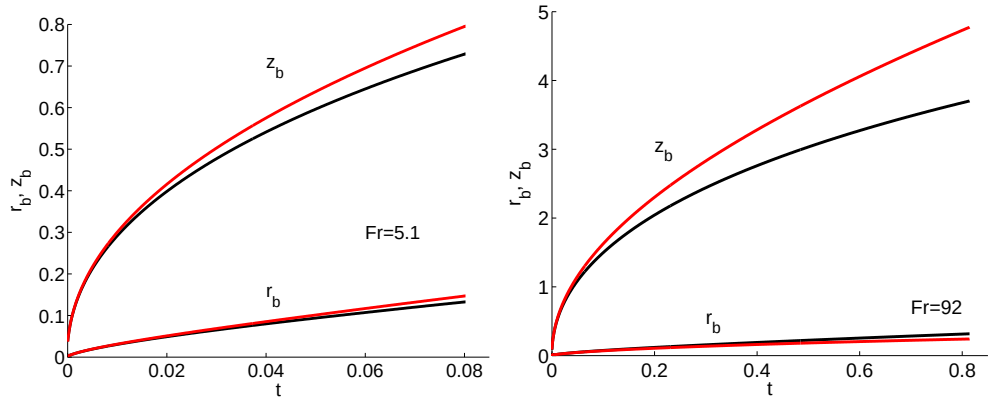


Figure 3.12: Time evolution of radial and axial positions of the jet base, $r_b$ and $z_b$ respectively. The upward jet is shown in black and the downward in red (for the downward jet $-z_b$ is shown for convenience). The behavior of both jets is very similar.

into the atmosphere.

In the following, we shall define $r_0(t) = 0.5 r_b(t)$ as the radial position on the jet interface at which radial velocities become negligible – $v \approx 0$ for jet radii smaller than $r_0$ – and the corresponding vertical position and velocity, will be denoted in what follows $z_0(t)$ and $u_0(t)$, respectively. Moreover, we will also define at this point a local Weber number as $\mathrm{We}_0(t) = \rho\, U_0(t)^2 R_0(t)/\sigma = \mathrm{We}\, u_0(t)^2 r_0(t)$ (recall that capital letters imply dimensional quantities and small letters their non-dimensional counterparts) whose time evolution is depicted in Fig. 3.14. The large values indicate that surface tension effects can be neglected in the description of the jet ejection process.

Thus, since the jet interface can be considered to be at constant atmospheric pressure and surface tension effects are negligible near the jet base, the only source of axial acceleration is the axial pressure gradient caused by the radial deceleration of the flow. Remarkably, this radial deceleration takes place in a very localized region nearby the jet base. (For radial positions on the jet smaller than $r_0$ already $v \simeq 0$ as shown in Fig. 3.13.) Therefore, the source of axial acceleration (radial deceleration) is no longer active high up into the jet, but only near the jet base. This key observation is used to define two of the three different regions within the jet: the *axial acceleration region* for $r_0 < r < r_b$ and $z_b < z < z_0$ and the *ballistic region* for $r < r_0$, $z \geqslant z_0$. The term used to name the latter region is based on the fact that, since $v \simeq 0$ for $r < r_0$ and the pressure at the jet interface is atmospheric, the momentum equation

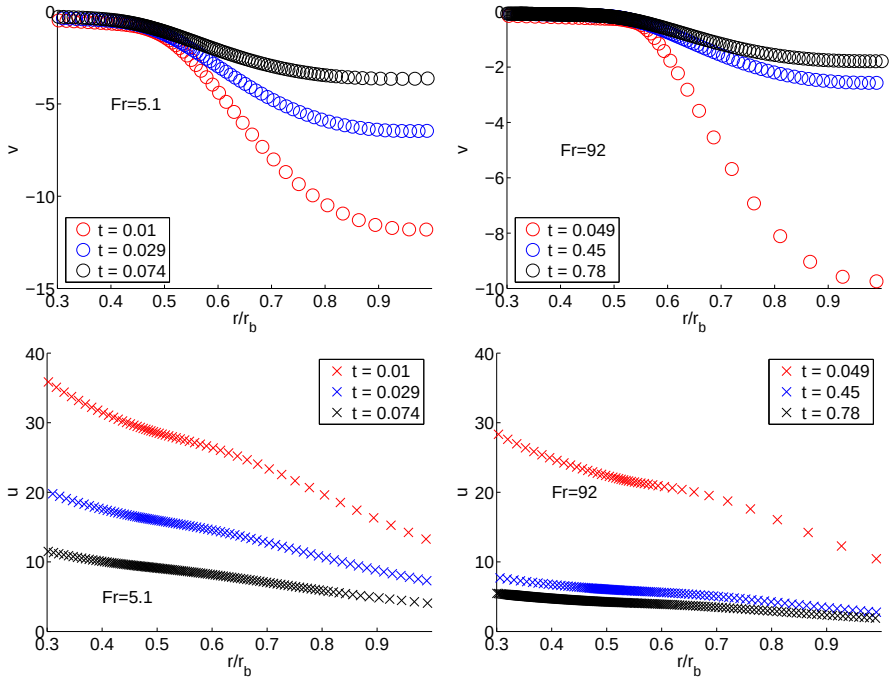


Figure 3.13: Time evolutions of the radial and axial velocities ($v$ and $u$ respectively) of the liquid evaluated at the jet interface for Fr=5.1 and Fr=92.

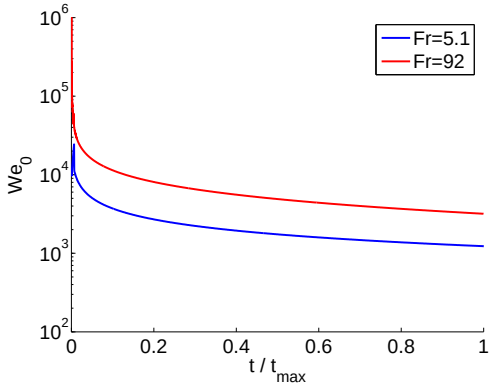


Figure 3.14: Time evolution of the local Weber number at the beginning of the ballistic region for two different values of the impact Froude number. The large values demonstrate that surface tension is not relevant during the jet ejection process. To facilitate the comparison between the different Froude cases, times have been normalized by $t_{\max}$, which is the time when the downward jet hits the disc and the simulation stops.

projected in the axial direction yields

$$\frac{Du}{Dt} = 0 \quad \text{for} \quad z > z_0 \quad \text{with} \quad u \neq u(r)\,, \tag{3.2}$$

and $D/Dt$ indicating the material derivative. Equation (3.2) implies that fluid particles are no longer accelerated upwards and conserve the vertical velocities they possess at $z = z_0$, which is the axial boundary between the *axial acceleration region* and the *ballistic region*. In Eq. (3.2), $u \neq u(r)$ since the radial velocity gradients of axial velocities are negligible in the ballistic region (not shown).

As a next step, we would like to scale the radial velocity field in the vicinity of the jet base which is, as discussed above, the source of momentum driving the jet ejection process. These radially inward velocities are originally created by the difference between the hydrostatic pressure in the bulk of the liquid and the gas pressure inside the cavity. After pinch-off however, the radial velocity field feeding the liquid jet is not appreciably modified by gravity during the time evolution of the jet since the local Froude number at the beginning of the ballistic region is $\mathrm{Fr}_0 = U_0^2/(gZ_{\text{surface}}) \gg 1$ with $Z_{\text{surface}}$ the axial distance between the beginning of the ballistic region and the height of the free surface far from the impact region (see Fig. 3.2).

Therefore, the radial velocities which give rise to the jet emergence can be characterized by the sink strength distribution at $t = 0$ right before pinch-off occurs:

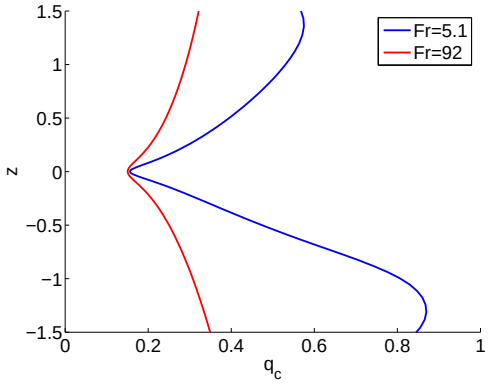


Figure 3.15: The sink strength distribution $q_c(z)$ for two values of the Froude number.

$q_c(z) = -r_c(z)\dot{r}_c(z)$, where $r_c$ and $\dot{r}_c$ indicate the radius of the cavity and its associated radial velocity, respectively (see [17]). The values of $q_c(z)$ are shown in Fig. 3.15 for several values of the impact Froude number.

In order to demonstrate the intimate relation of the jet ejection process with the velocity field right before pinch-off, we normalize the velocities $v$ and $u$ at the jet surface (as shown in Fig. 3.13) using, as the characteristic scale for velocities, $q_b(t)/r_b(t)$, where $q_b(t) = q_c(z = z_b(t))$ is the sink strength at the height of the jet base. The remarkable result, depicted in Fig. 3.16, is that both rescaled velocities nearly collapse onto the same master curves for a given Froude number and thus are almost constant in time for a fixed value of the rescaled position $r/r_b < 1$. This implies that, for a fixed value of $q_b$, axial velocities are inversely proportional to $r_b$ i.e., the smaller the jet base radius - or, equivalently, the more confined is the jet by the cavity walls -, the larger will be the axial liquid velocities within the jet.

Of critical importance for our forthcoming discussion is the rescaled axial velocity evaluated at the boundary of the ballistic region, $B_t = u_0(t)/(q_b(t)/r_b(t))$, whose time evolution is depicted in Fig. 3.17 (a). In accordance with the collapse of the rescaled velocities on a single master curve depicted in Fig. 3.16, $B_t$ hardly changes with time and, thus, we can define the function $B(\mathrm{Fr}) = u_0/(q_b/r_b)$ which depends also very weakly on the Froude number, as depicted in Fig. 3.17 (b).

The result in Fig. 3.17 possesses the additional remarkable implication that axial velocities within the jet are larger than the radial velocities existing at the cavity interface before pinch-off occurs. This can be seen directly by recalling that $|q_b/r_b| = |\dot{r}_b|$, such that $B$ is the ratio between the axial velocity $u_0$ with which fluid is ejected into the jet and the radial inward velocity at the jet base. Then, during the initial

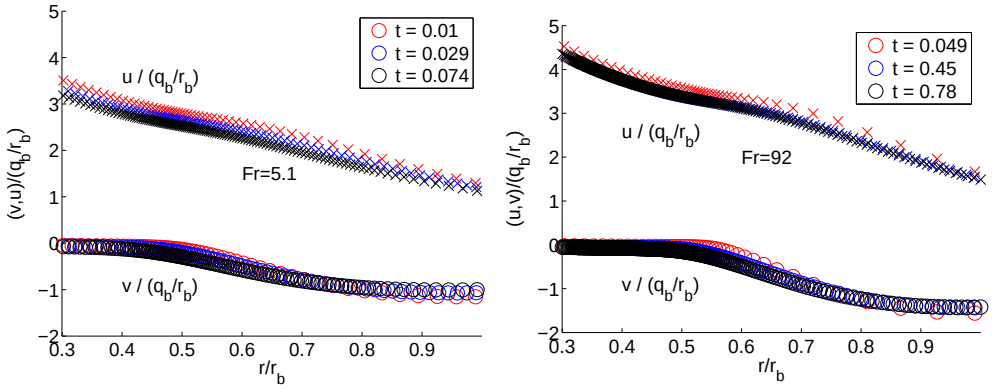


Figure 3.16: Spatial and temporal evolutions of the radial and axial velocities depicted in Fig. 3.13 normalized with $q_b(t)/r_b(t)$. Observe that $u/(q_b/r_b)$ and $v/(q_b/r_b)$ nearly collapse onto the same curves for each of the two values of the impact Froude number considered, $\mathrm{Fr} = 5.1$ (a) and $\mathrm{Fr} = 92$ (b).

instants of jet formation, $r_b \simeq r_{min}$, with $r_{min}$ the minimum radius of the cavity before jet emerges. Therefore, since the maximum radial velocity before pinch-off occurs is $|\dot{r}_{min}| = |q_c(z=0)/r_{min}|$, the maximum axial velocity within the jet is given by $\max(u_0) = B(\mathrm{Fr})\, q_c(z=0)/r_{min} \sim 3\,\dot{r}_{min}$. This means that, essentially, the velocity with which the jet is ejected is roughly three times larger than the maximum radial velocity attained before pinch-off!

In addition, provided that $\mathrm{We}_0 \gg 1$, fluid particles conserve their axial velocity within the ballistic region [see Eq. (3.2)] and, consequently, the tip of the jet *transports* away from the pinch-off location very valuable information about the largest velocities reached during the cavity collapse process. The knowledge of the function $B$ could thus allow an experimentalist to estimate the maximal pinch-off velocity simply from measurements of the jet tip velocity.

### 3.3.3 Jet ejection after bubble pinch-off from an underwater nozzle

This Section is devoted to the study of Worthington jets which are ejected after the bubble collapse into a liquid pool [25, 26]. As depicted in Fig. 3.3, these jets are quite similar to the ones formed after the impact of a solid body against a free surface and, thus, we expect that the conclusions of Section 3.3.2 can be also used for their description.

Figure 3.18 shows that, similarly to Section 3.3.2, the different shapes nearly collapse onto the same master curve when distances are normalized using $r_b$. This fact

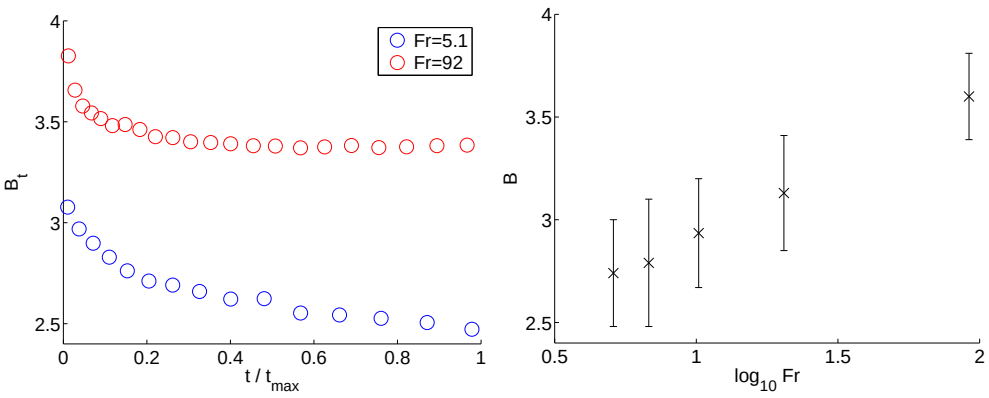


Figure 3.17: (a) The time evolution of $B_t$ demonstrates that $B_t$ is roughly constant in time, but does depend somewhat on the Froude number. (b) Taking the average of $B_t$ over time (with error bars indicating the min/max) for different Froude numbers yields a function $B(\mathrm{Fr})$ which varies only between 2.5 and 3.5 in the range $3 \leqslant \mathrm{Fr} \leqslant 92$. As indicated in Fig. 3.14, $t_{\max}$ is the time when the downward jet hits the disc and the simulation stops.

corroborates that $r_b$ is also the correct length scale to characterize this type of jets. However, differently to the case of Worthington jets ejected after the impact of a solid body against a free surface, in which $We_0 \gtrsim 10^3$, the local Weber number evaluated at the beginning of the ballistic region is $\sim O(10)$ in this case (see Fig. 3.19a). As a consequence of this, the total length at breakup of these jets is $\sim O(r_b)$ (see Fig. 3.18), i.e, much shorter than the length of the Worthington jets in Section 3.3.2. Moreover, such comparatively low values of the local Weber number indicate that surface tension has an effect in the description of the jet ballistic region. This is clearly appreciated in Figs. 3.18 and 3.20 where the collapse onto each other of the normalized time evolutions of the axial and radial velocity components evaluated at the free surface ($u$ and $v$) is also a bit deteriorated when compared with the case depicted in Fig. 3.16. Nevertheless, the two main prerequisites for the model to be presented in the following sections are also satisfied in this case: firstly, the acceleration and ballistic regions are clearly differentiated in Fig. 3.20 and, secondly, the normalization of the interfacial velocities with $q_b/r_b$ leads to a reasonable collapse onto a single master curve (see Fig. 3.20).

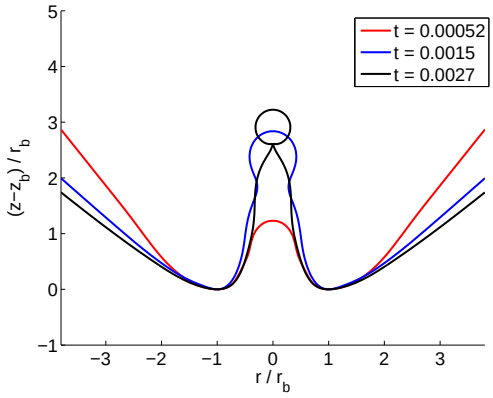


Figure 3.18: The time evolution of the shapes of the jets ejected after bubble pinch-off from an underwater nozzle, show good overlap when distances are normalized using $r_b$.

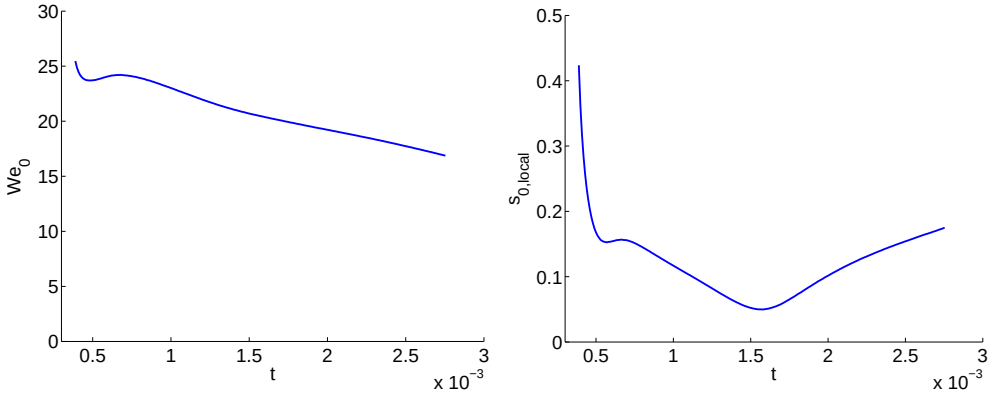


Figure 3.19: (a) Time evolution of the local Weber number for the jet depicted in Fig. 3.3. (b) Time evolution of the normalized strain rate $s_{0,local}$ (see Eq. (3.9)) at the beginning of the ballistic region for the same case as in (a).

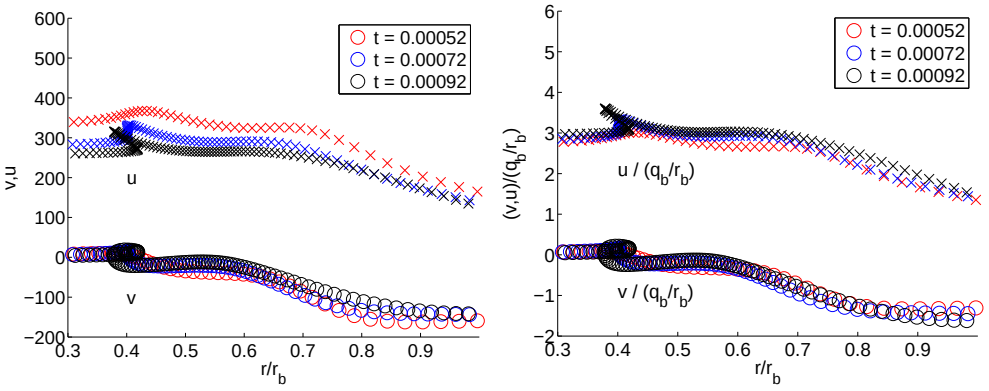


Figure 3.20: (a) Axial and radial velocities evaluated at the jet interface for the case depicted in Fig. 3.3. In analogy with Fig. 3.16, both the acceleration and ballistic regions are clearly identified: the modulus of the radial velocities decreases from $r = r_b$ to become negligibly small for $r/r_b \lesssim 0.5$. (b) The same as in (a), but with velocities scaled with $q_b/r_b$. Due to the fact that the Weber number is considerably smaller in this case than for the impacting disc, the jet tip region can be appreciated in this figure as the multivalued part of the curves $u$ and $v$ for $r/r_b \simeq 0.4$.

### 3.3.4 Jet breakup

The growth of capillary perturbations in a cylindrical liquid jet, firstly quantified by [49] (see also [50]), is based on the assumption that fluid particles conserve, to first order, their longitudinal velocity $U$. Note that for jet breakup surface tension is important as a driving force of the instabilities – in contrast to jet formation as shown in Fig. 2.1 in the previous chapter. Rayleigh's analysis shows that, moving in a frame of reference with the jet velocity $U$ (which in his case is constant $U \neq U(z,t)$), and no matter how large the Weber number is, the jet breaks due to the growth of capillary perturbations of wavelengths larger than the jet perimeter. The characteristic time needed for such perturbations to disrupt the jet into drops is the capillary time, $\sim (\rho R^3/\sigma)^{1/2}$, with $R$ the jet radius. Therefore the jet breakup length, $L_b$, is such that $L_b/R \propto (\rho U^2 R/\sigma)^{1/2}$ if aerodynamic effects are absent [51, 52]. Notice that the study of jet breakup in our case is somewhat related to that considered by Rayleigh since the fluid particles conserve their velocities, in a first approach, along the ballistic region of the jet.

Similarly to the case considered by [49], the study of the capillary breakup of stretched jets will be divided in two: the calculation of the *basic flow*, which is free of capillary effects and the analysis of capillary waves propagating and growing in

amplitude at the jet tip region. Viscous effects will be neglected in the analysis.

**Unperturbed flow**

If $We_0 \gg 1$, the time evolution of both the jet radius and the liquid velocities in the ballistic region can be calculated neglecting surface tension forces and making use of the slenderness of the jet. However, differently to the case considered by [49], in which the jet radius $r_{jet} = 1$ and $u = constant$, here $u$ and $r_{jet}$ are functions of $z$ and $t$. In effect, if the fluid is assumed to follow a purely vertical motion inside the ballistic region, the couple of equations that determine $u$ and $r_{jet}$ are the momentum equation (3.2), which can be also written as

$$\frac{Du}{Dt} = 0 \rightarrow \frac{\partial u}{\partial t} + u\frac{\partial u}{\partial z} = 0\,, \tag{3.3}$$

and the unidirectional version of the continuity equation, namely,

$$\frac{\partial r_{jet}^2}{\partial t} + \frac{\partial (u\, r_{jet}^2)}{\partial z} = 0 \rightarrow \frac{D \ln r_{jet}^2}{Dt} = -\frac{\partial u}{\partial z}\,, \tag{3.4}$$

where $D/Dt \equiv \partial/\partial t + u\partial/\partial z$ indicates again the material derivative. From Eqs. (3.3)-(3.4), $u$, $r_{jet}$ and $z_{jet}$ - the height at which the jet radius is $r_{jet}$ - are completely determined if the relevant quantities at the beginning of the ballistic region ($r_0$, $z_0$, and the velocity $u_0$) are known functions of time. Indeed, Eq. (3.3) expresses that fluid particles conserve the vertical velocity they possess at the beginning of the ballistic region. Consequently, a particle ejected from the acceleration into the ballistic region at time $\tau < t$ will, at time $t$, have attained a height

$$z_{jet}(t) = z_0(\tau) + (t - \tau)\, u_0(\tau). \tag{3.5}$$

Note that every fluid particle is ejected at a different time such that $\tau$ can serve as a label for the fluid particle. To obtain the corresponding jet radius $r_{jet}$, Eq. (3.4) can be integrated to give

$$r_{jet}^2(z = z_{jet}, t) = r_0^2(\tau)\frac{u_0(\tau) - d\, z_0/d\tau}{u_0(\tau) - d\, z_0/d\tau - d\, u_0(\tau)/d\tau (t - \tau)}\,. \tag{3.6}$$

Introducing the definition of the strain rate at the beginning of the ballistic region

$$s_o(\tau) = \frac{\partial u}{\partial z}(z = z_0) = -\frac{\dot{u}_o(\tau)}{u_o(\tau) - \dot{z}_o(\tau)} \tag{3.7}$$

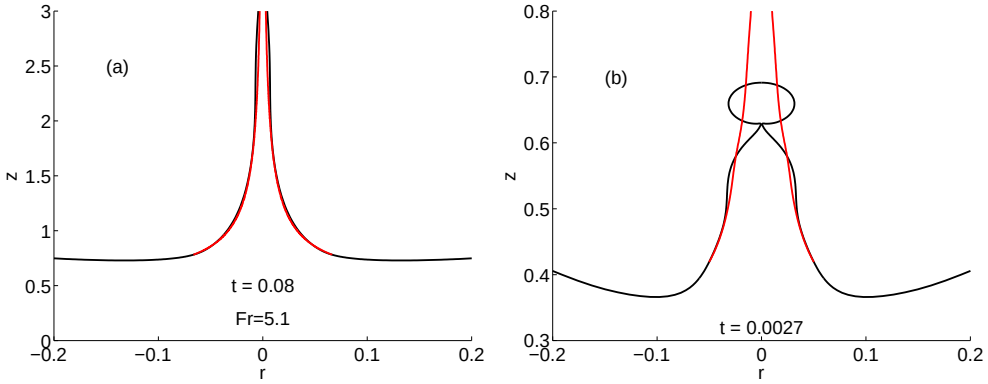


Figure 3.21: Comparison between the numerical jet shape and that obtained from Eq. (3.6) for the disc impact at Fr=5.1 (a) and the jet ejected from the underwater nozzle (b). The black line is the simulation and the red line is the analytical model. The input values of $r_0(t)$, $z_0(t)$ and $u_0(t)$ for the jet stretching model are taken from the simulations. Note that, since surface tension is not included in this model, the tip of the jet requires a separate treatment as described in Section 3.3.4

allows us to rewrite Eq. (3.6) in a more compact form as

$$r_{jet}^2(z_{jet},t) = \frac{r_o^2(\tau)}{1+(t-\tau)s_o}. \tag{3.8}$$

Note that Rayleigh's original analysis, $u = constant$ and $r_{jet} = 1$ (cylindrical jet) may be recovered from Eqs. (3.3)-(3.4) by setting $s_0 = 0$ and $u_0$, $z_0$ and $r_0$ constants in time. However, in our case, $\dot{u}_0 < 0$ and $u_0 = Bq_b/r_b > \dot{z}_b \simeq \dot{z}_0$ and, therefore, by virtue of Eq. (3.7), these conditions imply $s_o > 0$; consequently, from Eq. (3.8), the jet is not cylindrical since it stretches downstream.

Now, in order to obtain the complete jet shape at time $t$, we vary $\tau$ between 0 and $t$ and use Eqs. (3.5) and (3.6) to compute the corresponding vertical and radial coordinates of the jet. Note that, clearly, the particle ejected at $\tau = 0$ will end up forming the tip of the jet. The comparison between the numerical results and those obtained from the integration of (3.3)-(3.4), with the values of $u_o(\tau)$, $z_o(\tau)$ and $r_o(\tau)$ taken from the numerical simulations, is depicted in Fig. 3.21. The very good agreement between numerics and the model validates the approach of considering that fluid particles conserve their axial velocities within the ballistic region. It should be pointed out, however, that Eqs. (3.3)-(3.4) need to be corrected at the tip of the jet, where surface tension effects need to be retained.

**Growth of capillary disturbances**

The linear stability analysis for the type of velocity field given in Section 3.3.4 was firstly accomplished by [53], who recovered Rayleigh's original result in the limit of $s_0 = 0$. It is our purpose here to extend the analysis on the breakup of stretched jets of [53] to account for non linear effects and also for the influence of the tip. It is worthy to mention that, in our numerical approach, the wavelength of fastest growth rate is naturally selected by the local flow around the jet tip and, therefore, a linear stability analysis of the type reported in [53], is avoided. We will derive our results using simulations as depicted in Fig. 3.4 and apply them to the breakup of jets ejected from an underwater nozzle as depicted in Fig. 3.3.

As a first step, the dimensional counterparts of $r_0(\tau)$ $[R_0(\tau)]$ and $u_0(\tau)$ $[U_0(\tau)]$ are chosen as the characteristic scales for lengths and velocities, respectively. Consequently, dimensional analysis indicates that the evolution of capillary perturbations in the ballistic region for $t > \tau$ will solely depend on the dimensionless parameters $\mathrm{We}_0(\tau)$ and

$$s_{0,local}(\tau) = S_0(\tau)\, R_0(\tau)/U_0(\tau) = s_0(\tau)\, r_0(\tau)/u_0(\tau). \tag{3.9}$$

The values of $\mathrm{We}_0$ and $s_{0,local}$ depend non-trivially on the dimensionless parameters controlling the two different physical situations analyzed here. Consequently, in order to study systematically the jet breakup process as a function of $s_{0,local}$ and $\mathrm{We}_0$ we employ the third type of simulations of the axial strain type described in Section 3.2 and illustrated in Fig. 3.4. The real jet breakup process can then be reproduced provided that the values of the Weber number and the strain rate at the nozzle exit coincide with those at the beginning of the ballistic region i.e, $\mathrm{We}_0(\tau = 0) = \mathrm{We}_N = \rho\, U_N^2(0)\, R_N/\sigma$ and $s_{0,local}(\tau = 0) = \alpha$.

Note that, since the values of the Weber number based on $U_N$ and $\rho_g$ are always such that $\mathrm{We}_g = \rho_g\, U_N^2\, R_N/\sigma \ll 1$, the gas dynamics can be neglected and the only two relevant dimensionless parameters characterizing the axial strain system of Fig. 3.4 are $\mathrm{We}_N$ and $\alpha$.

The numerical results depicted in Fig. 3.22 show a slender liquid thread which breaks many diameters downstream the nozzle exit. Moreover, it can be observed that the effect of increasing the Weber number is to increase the breakup time and the breakup length. Figure 3.23 shows a comparison between the shapes of the jets formed after bubble collapse depicted in Fig. 3.18 and those obtained from the simulations of the type illustrated in Fig. 3.22 with $\mathrm{We}_N = \mathrm{We}_0(\tau = 0)$ and $\alpha = s_{0,local}(\tau = 0)$. The good agreement between both type of numerical results corroborates the fact that tip breakup of Worthington jets can be reproduced by means

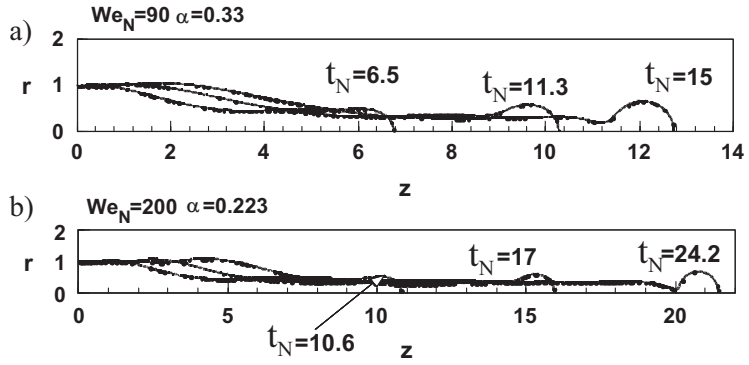


Figure 3.22: Time evolution of jets calculated for two different values of the pair of variables $(\mathrm{We}_N, \alpha)$ but the *same* value of the product $\mathrm{We}_N \alpha^2$.

of the simulations considered in this section if the values of the parameter $\mathrm{We}_N$ and $\alpha$ coincide with the initial values of $\mathrm{We}_0$ and $s_{0,local}$.

However, the numerical code used in this section is unstable for $\mathrm{We}_N \gtrsim O(10^3)$. Consequently, the third type of simulations cannot reproduce, at first sight, the breakup of jets ejected by an impacting disc since, in this case, $\mathrm{We}_0 \gtrsim 10^3$ as depicted in Fig. 3.14. Thus, is it nevertheless possible to describe the breakup process of jets with such high values of $\mathrm{We}_0$ using the numerical simulations of the axial strain type illustrated in Fig. 3.4? The answer to this question is affirmative if we realize that, in a frame of reference moving at the tip velocity, the parametrical dependence on the velocity $U_0(\tau = 0)$ disappears. Consequently, since both the local flow field and the jet radius still depends in this frame of reference on $S_0(\tau = 0)$ (see Eq. (3.7)), dimensional analysis indicates that jet breakup can be described in terms of the dimensionless variables $T\,S_0(\tau = 0)$ (or, analogously, $t_N \alpha$) and $\mathrm{We}_S = \rho\, S_0^2(\tau = 0) R_0^3(\tau = 0)/\sigma = \mathrm{We}\, r_0^3(\tau = 0)\, s_0^2(\tau = 0) = \mathrm{We}_0(\tau = 0)\, s_{0,local}^2(\tau = 0)$ (or, analogously, $\mathrm{We}_N \alpha^2$).

To check this, the results depicted in Fig. 3.22, which correspond to different values of $\mathrm{We}_N$ and $\alpha$ but to the same value of $\mathrm{We}_N \alpha^2$, are represented in Fig. 3.24. Remarkably, the different jet shapes superimpose onto each other for the same values of the dimensionless time $T\,S_0$, what indicates that the breakup process depends solely on $\mathrm{We}_S$ (or, equivalently, on $\mathrm{We}_N \alpha^2$) and on the dimensionless time $T\,S_0$ (or, equivalently, on $t_N \alpha$) for sufficiently large values of $\mathrm{We}_0$. Figure 3.25 illustrates that the volume of the nearly spherical drops formed at breakup, decreases for increasing values of $\mathrm{We}_S$. In Fig. 3.25 note also that the range of values of $\mathrm{We}_S$ investigated is realistic even for the impacting disc, as depicted in 3.26. Consequently, even though

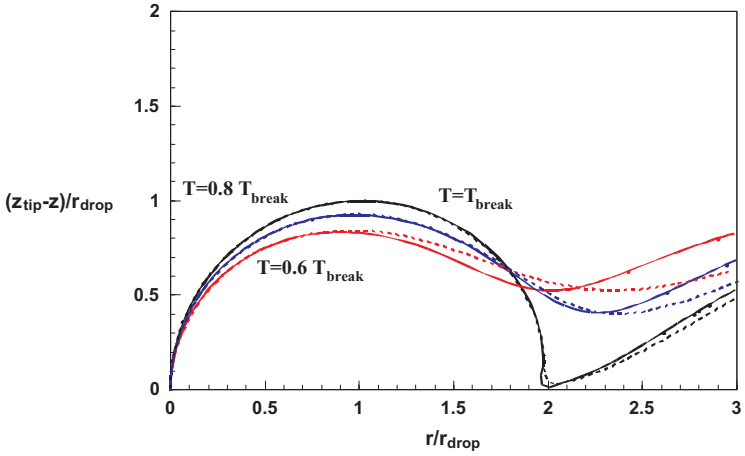


Figure 3.23: Jet shapes of Fig. 3.3 (in continuous lines) at three different instants of time ($0.6T_{break}$, $0.8T_{break}$ and $T_{break}$, with $T_{break}$ the breakup time) compared to those obtained from the type of simulations depicted in Fig. 3.22 (dashed lines) for the same values of $T$. The values of the parameters have been set to $\mathrm{We}_N = 25$ and $\alpha = 0.4$ which are the initial values of the local Weber number and the dimensionless axial strain rate of the simulations depicted in Fig. 3.19. Note that distances are rescaled using the final radius of the drop $R_{drop}$ as the characteristic length scale and that $z_{tip}$ denotes the axial coordinate of the tip of the jet.

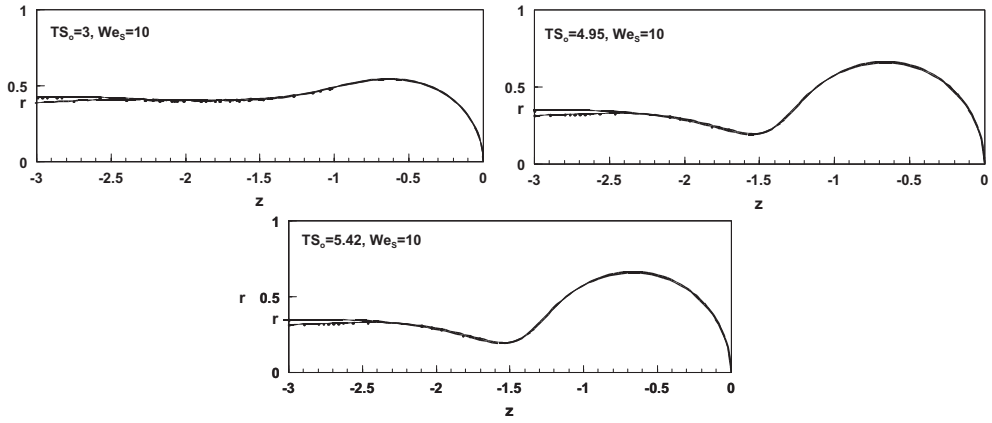


Figure 3.24: Translated jet shapes corresponding to the conditions $\mathrm{We}_N = 90$, $\alpha = 0.33$ and $\mathrm{We}_N = 200$ and $\alpha = 0.223$, depicted in Fig. 3.22 (a) and (b), respectively. Since $\mathrm{We}_S = \mathrm{We}_N\alpha^2 = 10$ in both cases, the time evolution near the tip region is identical in the normalized temporal variable $TS_0$.

$\mathrm{We}_0$ in some situations such as the disc may be very high, the important parameter which is $\mathrm{We}_S = \mathrm{We}_0(\tau = 0)s^2_{0,local}(\tau = 0)$ can be matched to the simulations in this section. We emphasize that Fig. 3.27 describes a universal relation for the breakup of Worthington jets at high Weber numbers which allows one to obtain the breakup time and volume of the first ejected droplet knowing merely the value of $\mathrm{We}_S$ defined at the beginning of jet formation.

Finally, note that, in order for $\mathrm{We}_N < O(10^3)$, the computations have been performed choosing $1 \ll \mathrm{We}_N \ll \mathrm{We}_0$ and, correspondingly, $\alpha > s_{0,local}$. The condition $\mathrm{We}_N \gg 1$ is essential since, if $\mathrm{We}_N$ was not sufficiently large, the jet breakup process of real Worthington jets would depend on the liquid velocity $U_N(0)$ and, thus, on $\mathrm{We}_N$ and $\alpha$ separately.

## 3.4 Modeling the jet ejection and breakup processes

Here we aim to develop a model to explain, in simple terms, the jet ejection and breakup processes for cases (i), (ii) and (iii) in Figs. 3.2, 3.3, 3.4. Our model will be based on the main conclusions of the previous section which are: (i) both $r_b$ and $z_b$ are *local* quantities which, therefore, do not depend on the large scales of the flow, (ii) the velocity field within the jet can be characterized solely in terms of the sink strength intensity at pinch-off, $q_c(z)$ and (iii) the flow field within the jet can be divided in

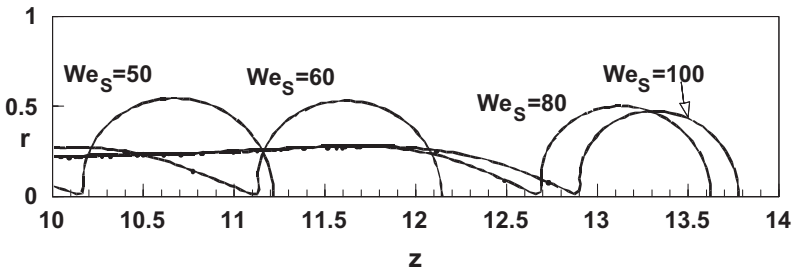


Figure 3.25: Tip region at the instant of breakup for different values of $\mathrm{We}_S$. Observe that the drops generated are nearly spherical and that their volume decreases for increasing values of $\mathrm{We}_S$.

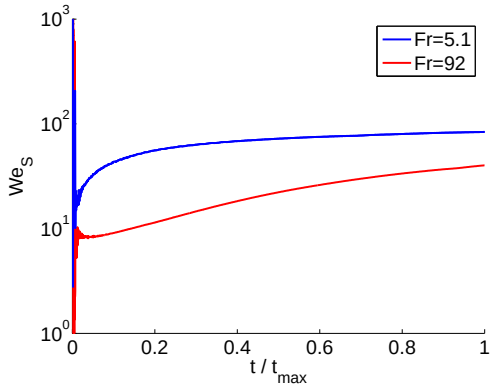


Figure 3.26: Time evolution of the normalized Weber number $\mathrm{We}_S = \mathrm{We}_0\, s^2_{0,local}$ for the impacting disc. As indicated in Fig. 3.14, $t_{\max}$ is the time when the downward jet hits the disc and the simulation stops.

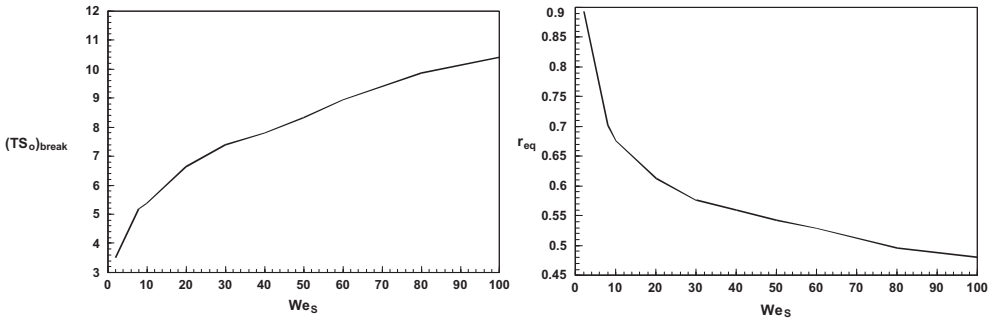


Figure 3.27: Numerical results of the dimensionless breakup time, $(TS_0)_{break}$ (a), and the dimensionless equivalent radius, $r_{eq}$ (b), with $4/3\pi\, r_{eq}^3 R_0^3$ the volume of the drops formed.

three parts: the *acceleration region*, the *ballistic region* and the *jet tip region*.

This section is structured as follows: in Section 3.4.1 $r_b(t)$ and $z_b(t)$ are calculated in terms of *only* $q_c(z)$ using the theory developed in [17]. Then, in Section 3.4.2 the axial velocity and the jet shape within the ballistic portion of the jet are calculated through Eqs. (3.3)-(3.4) using, as initial conditions, $r_0(\tau) = 0.5\, r_b(\tau)$, $u_0(\tau) = B(\mathrm{Fr})\, q_b(\tau)/r_b(\tau)$ and $z_0(\tau) = z_b(\tau) + 0.5 r_b(\tau)$.

### 3.4.1 Reviewing the model for $r_b(t)$ and $z_b(t)$

In this section we will very briefly review our model for jet formation as presented in [17] and show its applications to calculate the flow fields as well as the dynamics of the jet base for the impacting disc at Fr=5.1 and Fr=92 and the Worthington jets created after bubble pinch-off from an underwater nozzle.

The starting point of our model is the description of the cavity collapse using a line of sinks on the axis of symmetry as depicted in Fig. 3.15. After pinch-off most of this distribution remains intact with two notable exceptions: a hole is created between the bases of the up- and downward jet and sinks accumulate around the jet base [17]. These effects are illustrated in Fig. 3.28. Based on this observation we derived in [17] an analytical expression for the flow potential $\phi$ at an arbitrary point in the outer region (note that by construction the model is not valid inside the jet itself):

$$2\phi = \underbrace{-q_b \int_{-\infty}^{\infty} \frac{dz'}{\sqrt{r^2 + (z-z')^2}}}_{\text{collapsing cavity}} + \underbrace{q_b \int_{-z_b}^{z_b} \frac{dz'}{\sqrt{r^2 + (z-z')^2}}}_{\text{hole}} + \underbrace{\frac{C\, q_b\, r_b}{\sqrt{r^2 + (z-(z_b + C_{\mathrm{sink}} r_b))^2}}}_{\text{point sink}} \tag{3.10}$$

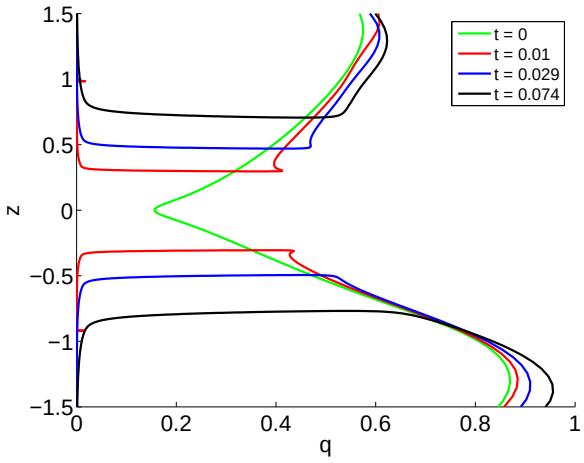


Figure 3.28: The sink distribution $q_c(z)$ at the moment of pinch-off (green) for the impacting disc at Fr=5.1 is the essential ingredient to our jet formation model. The sink distributions at later times (red, blue and black curves) are almost unchanged with respect to the sink distribution at pinch-off, confirming our model assumption that $q_c(z)$ is valid even for jet formation when two additional effects are accounted for: the accumulation of sinks around the base and the hole between the up- and the downward jet.

with the order one constants $C$ and $C_{\text{sink}}$ obtained from a fit of the model to the numerical data.

As shown in [17] this model can be used to calculate the temporal evolution of the jet base, i.e. the widening and upwards motion of the jet base. Here we will restrict ourselves to show the result of this procedure for the different systems studied in this work, which are depicted in Fig. 3.29.

In fact, as shown in Fig. 3.30, Eq. (3.10) can also be used to model the entire flow field in the outer region. Figs. 3.29-3.30 illustrate the rather good agreement between theory and numerics, which we find in all cases studied.

### 3.4.2 Combined modeling

We will now take the model of the previous section one step further by combining its results with the analysis described in Section 3.3.4. This will allow us to calculate not only the flow field in the outer region, but also the flow inside the jet and thus the jet shape as a function of time.

Once $r_b$ and $z_b$ are obtained through the model in Section 3.4.1, the axial velocity

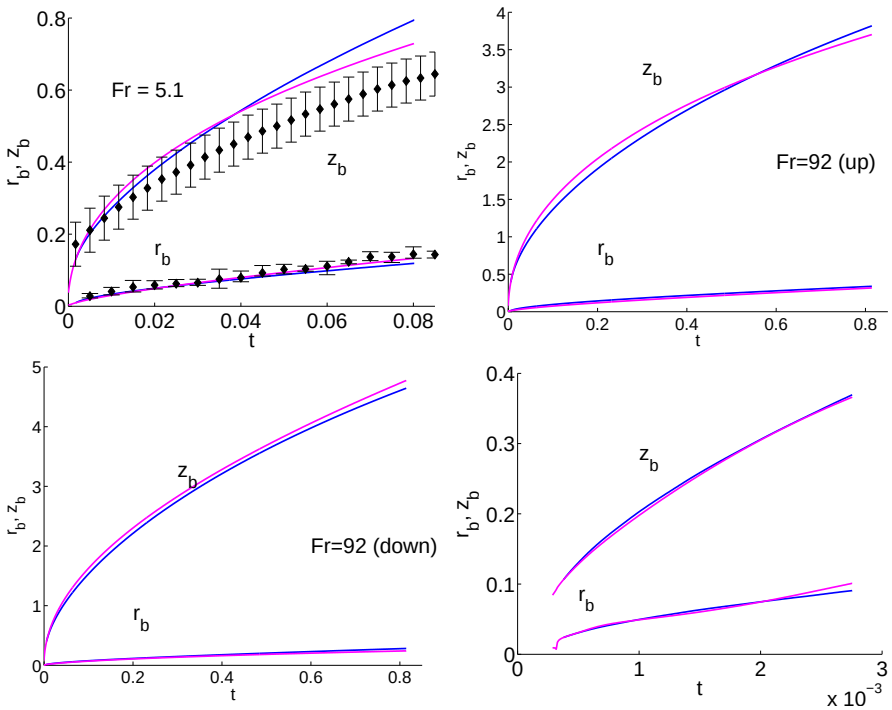


Figure 3.29: Time evolution (after pinch-off at $t = 0$) of the jet base radial and axial positions, $r_b$ and $z_b$ respectively, taken from the simulation (magenta lines) and the analytical model (blue lines). (a) Impacting disc with Fr=5.1 for the upward jet (here black diamonds represent experimental data) with $C = 4.55$ and $C_{\text{sink}} = 0.63$. (b) Impacting disc with Fr=92 (upward jet) with $C = 7.8$ and $C_{\text{sink}} = 0.63$. (c) Impacting disc with Fr=92 (downward jet) with $C = 6.66$ and $C_{\text{sink}} = 0.55$. (d) Upwards jet from the underwater nozzle with $C = 4.9$ and $C_{\text{sink}} = 0.76$.

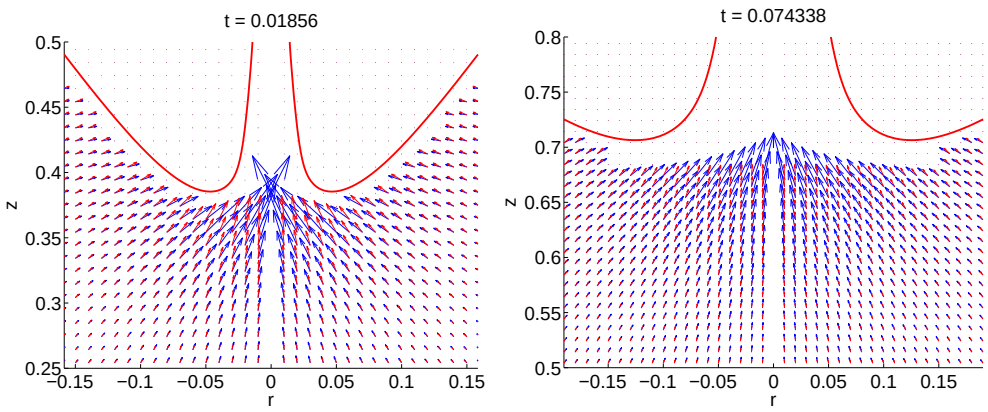


Figure 3.30: The flow field obtained from the model with constants $C = 4.55$ and $C_{\text{sink}} = 0.63$ for the disc impacting at Fr=5.1 (blue arrows) shows very good agreement with the numerically calculated flow field (red arrows). Velocity vectors are in arbitrary units and axis are, as throughout this work, non-dimensionalized with the disc radius. The region inside the jet and very close around the base is excluded since the model is not perfectly reliable there (due to the assumption of the observation point far from the base, see [17]).

at the beginning of the ballistic region can be calculated as a function of known quantities as $u_0(\tau) \simeq B(\text{Fr}) q_b(\tau)/r_b(\tau)$, with $B(\text{Fr})$ the function depicted in Fig. 3.17. Therefore, both the flow field and the jet shape within the ballistic region can be computed from the integration of Eqs. (3.3)-(3.4) using, as initial conditions, $r_0(\tau) = 0.5\, r_b(\tau)$, $u_0(\tau) = B(\text{Fr}) q_b(\tau)/r_b(\tau)$ and $z_0(\tau) = z_b(\tau) + 0.5 r_b(\tau)$. The comparison between the jet shape calculated numerically and that obtained from the model is depicted in Fig. 3.31 and good agreement is found.

The capillary breakup process of the jet can be also modeled making use of our numerical results in Section 3.3.4 since, through Eq. (3.7), both $\text{We}_0(\tau = 0)$ and $s_0(\tau = 0)$ can be easily expressed as a function of $u_0(\tau) = B\, q_b(\tau)/r_b(\tau)$, $z_b(\tau)$ and $r_b(\tau)$, with the latter two functions given by the model as described above. Consequently, using the data in Fig. 3.27 both the ejection and breakup process of the jet can be understood with the only inputs of $q_c(z)$ and $r_{min}$, i.e. quantities defined *before* pinch-off. Here, $q_c(z)$ is determined from the numerical simulations as described in the previous chapter. The cut-off radius $r_{\text{min}}$ must be determined experimentally or from numerical simulations which consider effects such as non-axisymmetric perturbations, air flow, and/or viscosity.

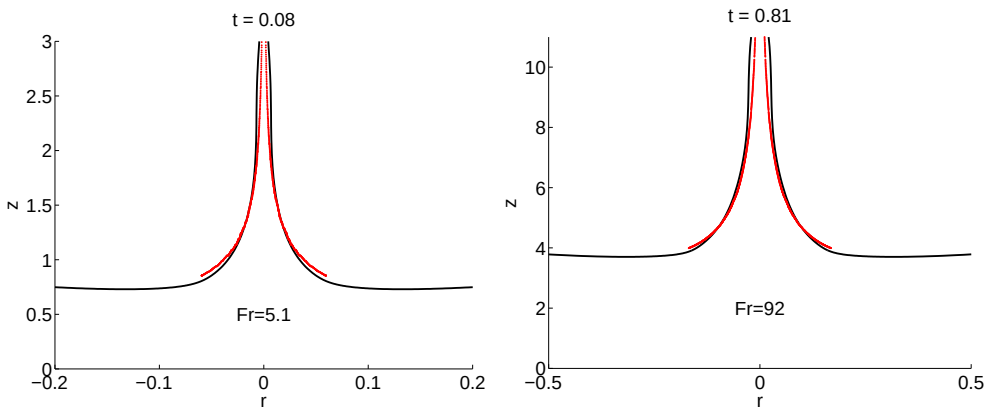


Figure 3.31: Comparison between the jet shape calculated using the boundary integral code (black line) and the one obtained integrating Eqs. (3.3)-(3.4) using the values of $r_b$ and $z_b$ given by the model described in Section 3.4.1 and shown in Fig. 3.29 (red line).

## 3.5 Conclusions

Using detailed boundary-integral simulations together with analytical modeling, we have studied the formation and breakup of the high-speed Worthington jets ejected either after the impact of a solid object on a liquid surface or after the pinch-off of a gas bubble from an underwater nozzle. To describe the phenomenon as a whole we divided the flow structure in two parts separated by the jet base ($r_b$, $z_b$): the *outer region* for $r > r_b$, $z < z_b$ and the jet region, extending from the jet base to the axis i.e, $r < r_b$ and $z \geqslant z_b$. The jet region is further subdivided into the three subregions: The *axial acceleration region*, where the radial inflow induced by the cavity collapse is decelerated radially and accelerated axially, the *ballistic region*, where fluid particles are no longer accelerated vertically and, thus, conserve the axial momentum they possess at the end of the acceleration region and the *jet tip region*, which is where the jet breakup process occurs.

We first show that the flow in the *outer region* is well described by the analytical model presented in [17]. This model further provides a set of equations for the time evolution of the jet base $r_b(t)$ and $z_b(t)$. As depicted in Figs. 3.29 and 3.30, the analytical calculations are in remarkable agreement with numerical simulations for the up- and downwards jets of the disc impact as well as the upwards jet created after the bubble pinch-off from an underwater nozzle. The model uses as its only input parameters the minimum radius of the cavity $r_{min}$ and the sink strength $q_c(z)$, both

taken at the moment of pinch-off.

The axial *acceleration region*, of characteristic length $O(r_b) \ll z_b$ is where the fluid is decelerated in the radial direction which causes an overpressure that accelerates the fluid vertically. This is thus a very narrow region, localized nearby the jet base, of crucial importance for the jet ejection process since it is where the fluid particles transform their radial momentum into axial momentum. We have found the remarkable result that both radial ($v$) and axial ($u$) velocities, when normalized with $q_c(z = z_b)/r_b = q_b/r_b$, nearly collapse onto the same master curves for both the disc and the nozzle. Therefore, the values of the rescaled velocities $(u,v)/(q_b/r_b)$ are almost constant in time for a fixed value of the rescaled position $r/r_b < 1$. We have also found that $v/(q_b/r_b) \simeq 0$ for that part of jet surface whose radius is smaller than $r_0 = 0.5\,r_b$. Therefore, since the source of axial acceleration - radial deceleration of the fluid - is no longer active when $r < r_0$ the corresponding vertical position $z_0$ constitutes the upper boundary of the acceleration region. In addition, we have found that the normalized axial velocity at $z_0$, $u_0/(q_b/r_b) = B$ is a function which depends very weakly on time and on the Froude number for the impacting disc case (see Fig. 3.17).

In the slender *ballistic region* the axial pressure gradients are negligible since $v \simeq 0$ and the Weber number evaluated at the beginning of the ballistic region ($\mathrm{We}_0 = \mathrm{We}\,u_0^2 r_0$) is much larger than unity. Therefore, we have developed a 1D model assuming that, in a first approach, fluid particles conserve their vertical velocities along the ballistic portion of the jet. This model allows us to calculate both the velocity field and the jet shape from Eqs. (3.3)-(3.8). The only input parameters are the radius, vertical position, and axial velocity at the beginning of the ballistic region. For the impacting disc, these values $r_0(t)$, $z_0(t)$, and $u_0(t)$, respectively, can be obtained directly from the analytical model of the outer region together with the function $B(\mathrm{Fr}) \simeq constant$ describing the acceleration region. For the underwater nozzle, the input parameters are provided directly by the numerical simulation. The results of this new model for the jet shape are in remarkable agreement with numerical simulations, as depicted in Figs. 3.21 and 3.31.

Finally, we have analyzed the *tip break-up region* of the stretched jet. The main result is that the jet capillary breakup can be described as a function of two dimensionless parameters: the local Weber number $\mathrm{We}_0$ and the strain rate evaluated at the beginning of the ballistic region, $s_0 = \partial u/\partial z(z = z_0)$. Both quantities can again be obtained either from the numerical simulations or from the models of the outer and acceleration regions. In order to study systematically the jet breakup process as a function of these two values we have simulated the injection of a liquid into the atmosphere from a nozzle of constant radius (see Fig. 3.4). The real jet breakup process can then be reproduced provided that the values of the Weber number and the strain

rate at the nozzle exit coincide with those at the beginning of the ballistic region, as shown in Fig. 3.23.

We have found that the tip breakup in our physical situations is not triggered by the growth of perturbations coming from an external source of noise. Instead, the jet breaks up due to the capillary deceleration of the liquid at the tip, which produces a corrugation to the jet shape. Moreover, for sufficiently large values of $\mathrm{We}_0$, the time evolution of the tip of the jet does not depend on $\mathrm{We}_0$ and $s_0$ separately, but can be described in terms of the dimensionless parameter $\mathrm{We}_S = \mathrm{We}\, r_0^3 s_0^2$ and the rescaled time $TS_0$. This universal description allows us thus to obtain the size of the droplet ejected from the tip (cf. Fig. 3.27) if $\mathrm{We}_0$ and $s_0$ are known from either simulations, measurements, or analytical models such as the one described in [17].

In summary, our description of Worthington jets created by the impact of a solid object on a liquid surface allows us to explain the jet base dynamics, the jet shape, and even the ejection of drops from the tip of the jet based on the knowledge of the minimum radius (e.g. from experiments) of the cavity before the jet emerges and the sink distribution at pinch-off.

## References

[1] A. M. Worthington and R. S. Cole, “Impact with a liquid surface studied by the aid of instantaneous photography”, Phil. Trans. Royal Soc. Series A **189**, 137–148 (1897).

[2] A. M. Worthington and R. S. Cole, “Impact with a liquid surface studied by the aid of instantaneous photography. Paper II”, Phil. Trans. Royal Soc. Series A **194**, 175–199 (1900).

[3] C. Duez, C. Ybert, C. Clanet, and L. Bocquet, “Making a splash with water repellency”, Nature Physics **3**, 180–183 (2007).

[4] J. M. Boulton-Stone and J. R. Blake, “Gas bubbles bursting at a free surface”, J. Fluid Mech. **254**, 437–466 (1993).

[5] L. Duchemin, S. Popinet, C. Josserand, and S. Zaleski, “Jet formation in bubbles bursting at a free surface”, Phys. Fluids **14**, 3000–3008 (2002).

[6] G. Liger-Belair, G. Polidori, and P. Jeandet, “Recent advances in the science of champagne bubbles”, Chem. Soc. Rev. **37**, 2490 (2008).

[7] H. N. Oguz and A. Prosperetti, “Bubble entrainment by the impact of drops on liquid surfaces”, J. Fluid Mech. **219**, 143–179 (1990).

[8] J. Shin and T. A. McMahon, "The tuning of a splash", Phys. Fluids A **2**, 1312–1317 (1990).

[9] M. Rein, "Phenomena of liquid drop impact on solid and liquid surfaces", Fluid. Dyn. Res. **12**, 61–93 (1993).

[10] D. Morton, M. Rudman, and J. L. Liow, "An investigation of the flow regimes resulting from splashing drops", Phys. Fluids **12**, 747–763 (2000).

[11] Q. Deng, A. V. Anilkumar, and T. G. Wang, "The role of viscosity and surface tension in bubble entrapment during drop impact onto a deep liquid pool", J. Fluid Mech. **578**, 119–138 (2007).

[12] D. Bartolo, C. Josserand, and D. Bonn, "Singular jets and bubbles in drop impact", Phys. Rev. Lett. **96**, 124501 (2006).

[13] F. MacIntyre, "Bubbles: A boundary-layer "microtome" for micron-thick samples of a liquid surface", J. Phys. Chem. **72**, 589–592 (1968).

[14] S. T. Thoroddsen, T. G. Etoh, and K. Takehara, "Microjetting from wave focussing on oscillating drops", Phys. Fluids **19**, 052101 (2007).

[15] J. E. Hogrefe, N. L. Peffley, C. L. Goodridge, W. T. Shi, H. G. E. Hentschel, and D. P. Lathrop, "Power-law singularities in gravity-capillary waves", Physica D **123**, 183–205 (1998).

[16] B. W. Zeff, B. Kleber, J. Fineberg, and D. P. Lathrop, "Singularity dynamics in curvature collapse and jet eruption on a fluid surface", Nature **403**, 401–404 (2000).

[17] S. Gekle, J. M. Gordillo, D. van der Meer, and D. Lohse, "High-speed jet formation after solid object impact", Phys. Rev. Lett. **102**, 034502 (2009),
*See Chapter 2 of this thesis.*

[18] C. D. Ohl and R. Ikink, "Shock-wave-induced jetting of micron-sized bubbles", Phys. Rev. Lett. **90**, 214502 (2003).

[19] K. K. Tjan and W. R. C. Phillips, "On impulsively generated inviscid axisymmetric surface jets, waves and drops", J. Fluid Mech. **576**, 377–403 (2007).

[20] A. Antkowiak, N. Bremond, S. L. Dizès, and E. Villermaux, "Short-term dynamics of a density interface following an impact", J. Fluid Mech. **577**, 241–250 (2007).

[21] J. R. Blake, P. B. Robinson, A. Shima, and Y. Tomita, "Interaction of two cavitation bubbles with a rigid boundary", J. Fluid Mech. **255**, 707–721 (1993).

[22] M. S. Longuet-Higgins, "Bubbles, breaking waves and hyperbolic jets at a free surface", J. Fluid Mech. **127**, 103–121 (1983).

[23] M. S. Longuet-Higgins and H. Oguz, "Critical microjets in collapsing cavities", J. Fluid Mech. **290**, 183–201 (1995).

[24] G. D. Birkhoff, D. P. MacDonald, W. M. Pugh, and G. I. Taylor, "Explosives with lined cavities", J. Appl. Phys. **19**, 563–582 (1948).

[25] R. Manasseh, S. Yoshida, and M. Rudman, "Bubble formation processes and bubble acoustic signals", Third International Conference on Multiphase Flow, ICMF'98 Lyon, France 1–8 (1998).

[26] R. Bolaños-Jiménez, A. Sevilla, C. Martinez-Bazán, and J. M. Gordillo, "Axisymmetric bubble collapse in a quiescent liquid pool. II. Experimental study", Phys. Fluids **20**, 112104 (2008).

[27] S. T. Thoroddsen and A. Q. Shen, "Granular jets", Phys. Fluids **13**, 4–6 (2001).

[28] D. Lohse, R. Bergmann, R. Mikkelsen, C. Zeilstra, D. van der Meer, M. Versluis, K. van der Weele, M. van der Hoef, and H. Kuipers, "Impact on soft sand: void collapse and jet formation", Phys. Rev. Lett. **93**, 198003 (2004).

[29] V. Duclaux, F. Caillé, C. Duez, C. Ybert, L. Bocquet, and C. Clanet, "Dynamics of transient cavities", J. Fluid Mech. **591**, 1–19 (2007).

[30] J. W. Glasheen and T. A. McMahon, "Vertical water entry of disks at low froude numbers", Phys. Fluids **8**, 2078–2083 (1996).

[31] R. Bergmann, D. van der Meer, M. Stijnman, M. Sandtke, A. Prosperetti, and D. Lohse, "Giant bubble pinch-off", Phys. Rev. Lett. **96**, 154505 (2006).

[32] R. Bergmann, D. van der Meer, S. Gekle, A. van der Bos, and D. Lohse, "Controlled impact of a disc on a water surface: Cavity dynamics", J. Fluid Mech. **633**, 381–409 (2009).

[33] S. Gekle, A. van der Bos, R. Bergmann, D. van der Meer, and D. Lohse, "Noncontinuous froude number scaling for the closure depth of a cylindrical cavity", Phys. Rev. Lett. **100**, 084502 (2008),
*See Chapter 7 of this thesis.*

[34] M. S. Longuet-Higgins, B. R. Kerman, and K. Lunde, "The release of air bubbles from an underwater nozzle", J. Fluid Mech. **230**, 365–390 (1991).

[35] H. N. Oguz and A. Prosperetti, "Dynamics of bubble growth and detachment from a needle", J. Fluid Mech. **257**, 111–145 (1993).

[36] J. C. Burton, R. Waldrep, and P. Taborek, "Scaling and instabilities in bubble pinch-off", Phys. Rev. Lett. **94**, 184502 (2005).

[37] N. C. Keim, P. Møller, W. W. Zhang, and S. R. Nagel, "Breakup of air bubbles in water: breakdown of cylindrical symmetry", Phys. Rev. Lett. **97**, 144503 (2006).

[38] S. T. Thoroddsen, T. G. Etoh, and K. Takehara, "Experiments on bubble pinch-off", Phys. Fluids **19**, 042101 (2007).

[39] S. Thoroddsen, T. Etoh, and K. Takehara, "High-speed imaging of drops and bubbles", Annu. Rev. Fluid Mech. **40**, 257–285 (2008).

[40] J. M. Gordillo, A. Sevilla, and C. Martínez-Bazán, "Bubbling in a co-flow at high reynolds numbers", Phys. Fluids **19**, 077102 (2007).

[41] J. C. Burton and P. Taborek, "Bifurcation from bubble to droplet in inviscid pinch-off", Phys. Rev. Lett. **101**, 214502 (2008).

[42] J. M. Gordillo, "Axisymmetric bubble collapse in a quiescent liquid pool. I. Theory and numerical simulations", Phys. Fluids **20**, 112103 (2008).

[43] L. E. Schmidt, N. C. Keim, W. W. Zhang, and S. R. Nagel, "Memory-encoding vibrations in a disconnecting air bubble", Nature physics **5**, 343–346 (2009).

[44] J. M. Gordillo, A. Sevilla, J. Rodríguez-Rodríguez, and C. Martínez-Bazán, "Axisymmetric bubble pinch-off at high reynolds numbers", Phys. Rev. Lett. **95**, 194501 (2005).

[45] S. Gekle, I. R. Peters, J. M. Gordillo, D. van der Meer, and D. Lohse, "Supersonic air flow due to solid-liquid impact", preprint (2009),
*See Chapter 4 of this thesis.*

[46] S. Gekle, J. H. Snoeijer, D. Lohse, and D. van der Meer, "Approach to universality in axisymmetric bubble pinch-off", Phys. Rev. E **80**, 036305 (2009),
*See Chapter 6 of this thesis.*

[47] R. Bolanos-Jiménez, A. Sevilla, C. Martínez-Bazán, D. van der Meer, and J. M. Gordillo, "The effect of liquid viscosity on bubble pinch-off", Phys. Fluids **21**, 072103 (2009).

[48] D. Leppinen and J. Lister, "Capillary pinch-off in inviscid fluids", Phys. Fluids **15**, 568–578 (2003).

[49] W. S. Rayleigh, "On the instability of jets", Proc. of the London Math. Soc. **10**, 4–13 (1878).

[50] J. Eggers and E. Villermaux, "Physics of liquid jets", Rep. Prog. Phys. **71**, 036601 (2008).

[51] A. Sterling and C. Sleicher, "The instability of capillary jets", J. Fluid Mech. **68**, 477–495 (1975).

[52] J. M. Gordillo and M. Pérez-Saborid, "Aerodynamic effects in the break-up of liquid jets: on the first wind-induced break-up regime", J. Fluid Mech. **541**, 1–20 (2005).

[53] I. Frankel and D. Weihs, "Stability of a capillary jet with linearly increasing axial velocity (with application to shaped charges)", J. Fluid Mech. **155**, 289–307 (1985).

[54] A. R. Hanson, E. G. Domich, and H. S. Adams, "Shock tube investigation of the break-up of drops by air blasts", Phys. Fluids **6(8)**, 1070–1080 (1963).

[55] E. Villermaux, "Fragmentation", Annu. Rev. Fluid Mech. **49**, 419–446 (2007).

[56] E. Villermaux, "Single-drop fragmentation determines size distribution of raindrops", Nature Physics **5**, 697–702 (2009).

# 4

# Supersonic air flow due to solid-liquid impact

* †

*A solid object impacting on liquid creates a liquid jet due to the collapse of the impact cavity. Using visualization experiments with smoke particles and multiphase simulations we show that in addition a high-speed air-jet is pushed out of the cavity. Despite an impact velocity of only 1 m/s, this air-jet attains supersonic speeds. The cavity pressure nonetheless is merely 1.02 atmospheres and thus much lower than the pressures usually observed in supersonic flow through a rigid nozzle. The high air speeds are shown to result from the "nozzle" being a liquid cavity shrinking rapidly in time.*

## 4.1 Introduction

Taking a stone and throwing it onto the quiescent surface of a lake triggers a spectacular series of events which has been the subject of scientists' interest for more than a century [1–17]: upon impact a thin sheet of liquid (the "crown splash") is thrown

*Submitted as: Stephan Gekle, Ivo Peters, José Manuel Gordillo, Devaraj van der Meer, and Detlef Lohse, "Supersonic air flow due to solid-liquid impact", Phys. Rev. Lett. (2009).

†The numerical simulations in this chapter are part of the present thesis. The experimental work is due to Ivo Peters.

upwards along the rim of the impacting object while below the water surface a large cavity forms in the wake of the impactor. Due to the hydrostatic pressure of the surrounding liquid this cavity immediately starts to collapse and eventually closes in a single point ejecting a thin, almost needle-like liquid jet. Just prior to the ejection of the liquid jet the cavity possesses a characteristic elongated "hourglass" shape with a large radius at its bottom, a thin neck region in the center, and a widening exit towards the atmosphere.

This shape is very reminiscent of the converging-diverging ("de Laval") nozzles known from aerodynamics as the paradigmatic picture of compressible gas flow through, e.g., supersonic jet engines. In this Letter we use a combination of experiments and numerical simulations to show that in addition to the very similar shape, also the structure of the air flow through the impact cavity resembles closely the high-speed flow of gas through such a nozzle. Not only is the flow to a good approximation one-dimensional, but it even attains supersonic velocities. Nevertheless, the pressure inside the cavity is merely 2% higher than the surrounding atmosphere which is much lower than the overpressures commonly used in steady supersonic flow through a normal nozzle. The key difference is that in our case the "nozzle" is a liquid cavity whose shape is evolving rapidly in time.

## 4.2 Experimental setup

Our experimental setup consists of a thin circular disc with radius $R_0 = 2$ cm which is pulled through the liquid surface by a linear motor mounted at the bottom of a large water tank [16] with a constant speed of $V_0 = 1$ m/s. To visualize the air flow we use small glycerin droplets produced by a commercially available smoke machine (skytec) commonly used for light effects in theaters and discotheques. Before the start of the experiment the atmosphere above the water surface is filled with this smoke which is consequently entrained into the cavity by the impacting disc. A laser sheet (Larisis Magnum II, 1500mW) shining in from above illuminates a vertical plane containing the axis of symmetry of the system. A high-speed camera (Photron SA1.1) records the motion of the smoke particles at up to 15,000 frames per second. Cross-correlation of subsequent images allows us to extract the velocity of the smoke which faithfully reflects the actual air speed (see appendix). Our setup obeys axisymmetry and we use cylindrical coordinates with $z = 0$ the level of the undisturbed free surface.

In the beginning of the process (see the snapshot in Fig. 4.1 (a)) air is drawn into the expanding cavity behind the impacting object with velocities of the order of the impact speed. At a later stage, however, this downward flux is overcompensated by the overall shrinking of the cavity volume resulting in a net flux out of the cavity. The

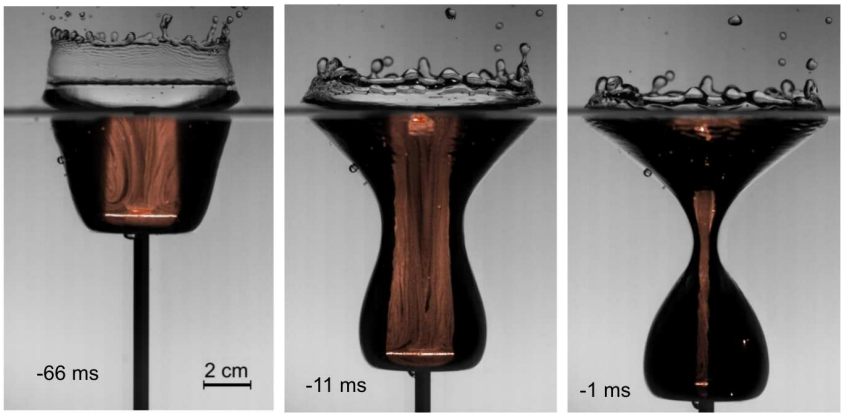


Figure 4.1: (a) After the impact of the disc an axisymmetric cavity is formed in its wake and air is entrained into this cavity. (b) Due to hydrostatic pressure from the surrounding liquid the cavity starts to collapse and the air flow reverses its direction. (c) As the collapse proceeds air is pushed out of the shrinking cavity at very high speeds. In (a)–(c) we overlaid images of the cavity shape (recorded with backlight) and images of the smoke particles (recorded with the laser sheet and artificially colored in orange). In the latter, the area illuminated by the vertical laser sheet is restricted by the minimum cavity radius (see appendix). Times are given relative to the moment of cavity closure.

cavity shape at the moment when the flow through the neck reverses its direction is illustrated in Fig. 4.1 (b). Towards the end of the cavity collapse a thin and fast air stream is pushed out through the cavity neck which is illustrated in Fig. 4.1 (c). From images such as those in Fig. 4.1 we can directly measure the air speed $u$ up to about 10 m/s as is shown in the inset of Fig. 4.2.

## 4.3 Numerical method

In order to determine the flow speed at even higher velocities we revert to multiphase numerical simulations. Our numerical method proceeds in two stages: an incompressible stage at the beginning and a compressible stage towards the end of the impact process. During the first stage both air and liquid are treated as incompressible, irrotational, and inviscid potential fluids. To solve for the flow field and to calculate the motion of the interface we use a boundary integral method (BIM) as described

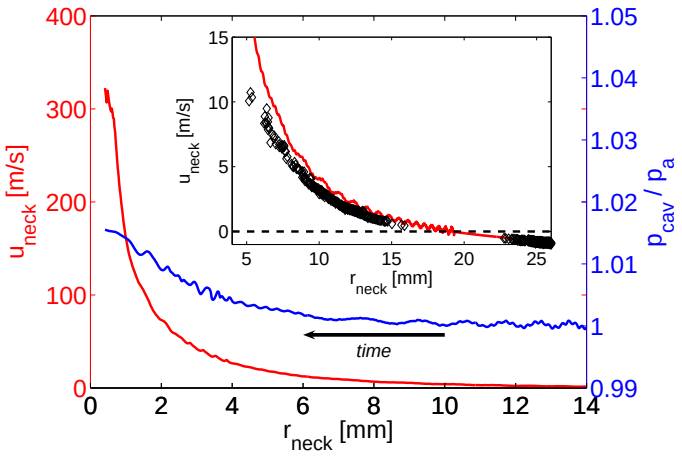


Figure 4.2: The speed of the gas flowing through the neck (red curve) as a function of the shrinking cavity neck taken from the fully compressible simulations. The main plot demonstrates that sonic speeds are attained with the cavity pressure (blue curve) being less than 2% higher than the atmospheric pressure. The inset shows an enlargement demonstrating that the numerical scheme (red curve) agrees very well with the experimentally measured velocity (black diamonds; the hole in the data between $r_{\mathrm{neck}} = 16$ mm and 22 mm is due to measurement uncertainties at low absolute velocities; see appendix). Slight non-axisymmetric perturbations [18, 19] in the experimental setup are responsible for the somewhat slower air speed of the experiment as compared to the simulation. One can clearly see the inversion of the flow direction from negative (into the cavity) to positive (out of the cavity) velocities.

in [16] with extensions to include the gas phase [20]. At the moment that the air flow through the neck reverses, see Fig. 4.1 (b), the simulation enters into the second, compressible stage: from now on only the liquid motion is computed by the incompressible BIM.

To simulate the air flow in the second stage we need to take compressibility into account meaning that a simple potential flow description is no longer possible. Fortunately, at the end of the incompressible stage the air velocity profile is almost perfectly one-dimensional along the axis of symmetry. We can therefore approximate the gas dynamics by the 1D compressible Euler equations [21] in analogy to gas flowing through a converging-diverging nozzle. In the Euler equations we include two additional terms accounting for the variation of the nozzle radius in time and space. For the numerical solution we use a Roe scheme [21, 22] which is highly appreciated for its computational efficiency and ability to accurately capture shock fronts.

The two-way coupling between the gas and the liquid domains is accomplished via (i) the interfacial shape and its instantaneous velocity which is provided by the BIM and serves as an input into the gas solver and (ii) the pressure which is obtained from the solution of the Euler equations and serves as a boundary condition for the BIM. Above the location of the initial free surface the surface pressure of the BIM remains atmospheric. Our combined BIM/Euler method has the advantage that we retain the computational efficiency of the BIM which requires only the modeling of the boundary and not of the entire liquid domain in contrast to, e.g. compressible air/water treatments based on the Volume-of-Fluid method for sloshing tanks [23].

## 4.4 Results

Combining our experiments with these numerical simulations leads to the main result of this Letter contained in Fig. 4.2: the collapsing liquid cavity acts as a rapidly deforming nozzle, so violent that the air which is pushed out through the neck attains supersonic velocities (red line). Remarkably, our simulations show that the pressure inside the cavity which is driving this flow is less than 1.02 atmospheres (blue line). From the inset one can tell that our simulations are in good agreement with the smoke measurements over the entire experimentally accessible range.

To determine more precisely at what point the air flow through the neck becomes sonic we show in Fig. 4.3 (a) the evolution of the local Mach number, $\mathrm{Ma}_{\mathrm{neck}} = u_{\mathrm{neck}}/c$ (with the gas velocity $u_{\mathrm{neck}}$ and the speed of sound $c$), for discs impacting at 1 and 2 m/s. We find that the speed of sound is attained at cavity radii as large as 0.5 mm for the lower impact velocity and 1.2 mm for the higher impact velocity.

In a steady state one could expect from the (compressible) Bernoulli equation that

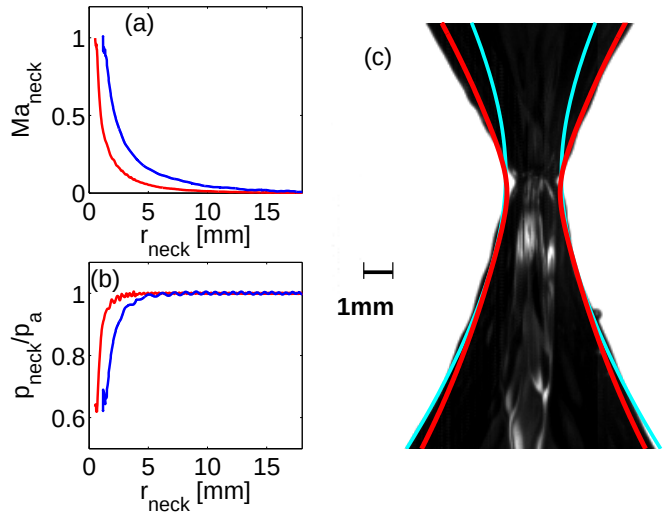


Figure 4.3: (a) The evolution of the local Mach number at the cavity neck for different impact speeds (red: 1 m/s, blue: 2 m/s). For the 2 m/s impact speed sonic flow is attained at a cavity radius of 1.2 mm. (b) The pressure at the neck diminishes due to Bernoulli suction as the neck radius shrinks and air is forced to flow faster and faster. The minimum pressure lies at about $0.6p_a$ which is attained when the Mach number reaches unity. (c) The experimental image shows a pronounced kink at the neck which is not captured by the smoothly rounded curve predicted by the simulation without air (cyan line). Only the inclusion of air effects into the simulations (red line) is able to produce a kink-like shape caused by the low air pressure at the neck as well as the shape of the cavity above the neck.

these very high air speeds would cause a greatly diminished air pressure in the neck region. Despite the unsteadiness of our situation, the data presented in Fig. 4.3 (b) indeed shows that the pressure $p_{\text{neck}}$ decreases significantly once the neck has shrunk to a diameter of roughly 4 mm (for the 1 m/s impact) while before that point it is practically atmospheric throughout. Classical steady-state theory [24] for a converging-diverging nozzle predicts that when $\text{Ma}_{\text{neck}} = 1$ the pressure at the neck reaches a minimum value of

$$p_{\text{neck}}/p_a = \left(1 + \frac{\gamma - 1}{2}\right)^{-\gamma/(\gamma-1)} = 0.53 \tag{4.1}$$

with $p_a$ the atmospheric pressure and $\gamma = 1.4$ the isentropic exponent. As shown in Fig. 4.3 (b) our situation – although highly unsteady – exhibits a similar behavior with $p_{\text{neck}} \approx 0.6 p_a$ as the Mach number becomes of order unity.

In Fig. 4.3 (c) we illustrate how this low pressure gives us a handle to observe the consequences of the supersonic air speed in our experiments: despite the air being three orders of magnitude less dense than water, it is able to exert a significant influence even on the shape of the liquid cavity provided that its speed is high enough [25, 26]. From the experimental image it is clear that the free surface close to collapse no longer possesses a smoothly rounded shape but instead shows a significant increase in curvature at the minimum (a “kink”). While this feature is not present in a simulation neglecting the influence of air as those in [16], the inclusion of air effects allows us to capture quite accurately the cavity shape observed experimentally, although the numerical is not as strongly ”kinked” as the experimental image. This gives strong evidence that in the experiment the air indeed becomes as fast as predicted by the simulations and produces a Bernoulli suction effect strong enough to deform the cavity.

The positive sign of $u_{\text{neck}}$ (see Fig. 4.2) indicates that the gas flow is directed upwards at the neck. At the same time, the air at the bottom of the cavity is pulled downwards by the moving disc. An interesting consequence of this competition between cavity expansion at the bottom and cavity shrinking in the neck is the existence of a stagnation point with $u = 0$ as can readily be observed in Fig. 4.4 (a) and its magnification in Fig. 4.4 (c).

As can be seen in the inset of Fig. 4.5, the distance between the neck and the stagnation point is no larger than roughly 5 mm prior to cavity closure. Nevertheless, the pressure at the stagnation point equals the overall pressure inside the cavity which is roughly atmospheric during the whole process (see Fig. 4.2). Recalling that $p_{\text{neck}} \approx 0.6 p_a$ this results in a tremendous vertical pressure gradient which of course affects the dynamics of the cavity wall: the flow of air is so strong that it can drag

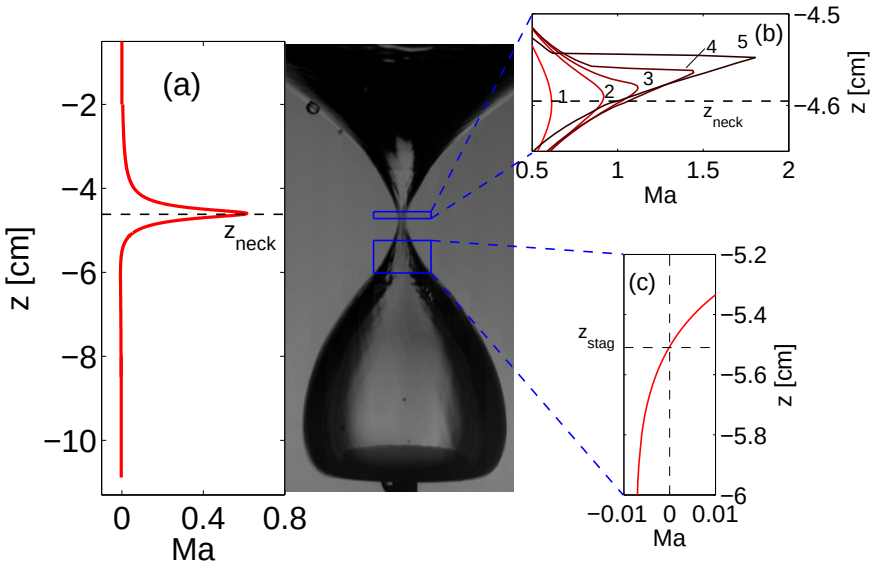


Figure 4.4: (a) The vertical air velocity normalized by the local speed of sound Ma $=$ $u/c$ as a function of the vertical position (the corresponding cavity image is shown in the middle) for $r_{\text{neck}} = 0.9$ mm: the profile exhibits a sharp peak approximately at the height of the neck. (b) A close-up of the zone around the neck illustrates the steepening of the velocity profiles towards pinch-off (numbers 1-5 correspond to neck radii between 0.9 mm (number 1, bright red) and 0.5 mm (number 5, dark brown)) and the development of the shock front at roughly 0.1 ms before pinch-off. The neck position $z_{\text{neck}}$ corresponding to curve 5 is shown by the dashed line. (c) A close-up of the area below the neck shows the location of the gas flow stagnation point $z_{\text{stag}}$ (dashed line).

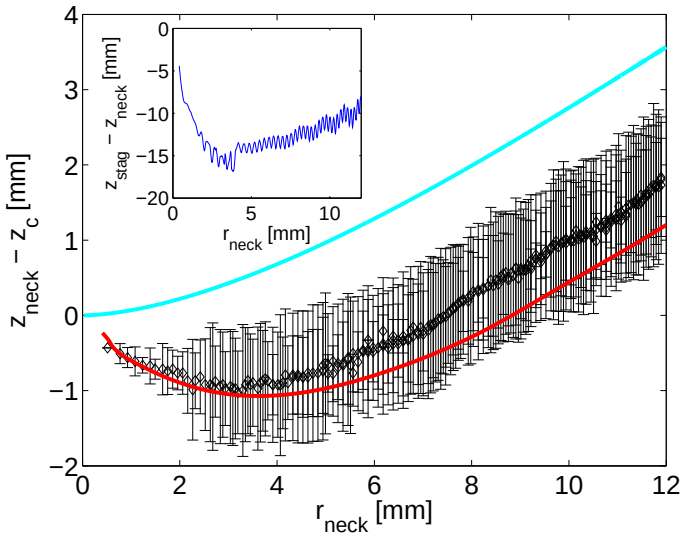


Figure 4.5: The vertical position of the cavity neck relative to the final closure height $z_c$ as a function of the shrinking neck radius from experiments at 30,000 frames per second (black diamonds), simulations with (red line) and without (cyan line) air dynamics. The experimental data is in quantitative agreement with the compressible simulations, while clearly the simulation neglecting air fails to capture the upward motion of the minimum induced by the large pressure gradient between the stagnation point and the cavity neck. Experimental error bars are determined by the number of vertically neighboring pixels all sharing the same minimum radius. The inset shows the approach of the stagnation point to the neck.

the liquid along resulting in an upward motion of the cavity neck just before the final collapse. That this effect is indeed present in the simulations can be seen from the red line in Fig. 4.5. For comparison, the cyan curve demonstrates that a single fluid simulation neglecting the air dynamics would predict a monotonously decreasing position. The experimental data however is in quantitative agreement with the compressible simulations. Together with the cavity shape shown in Fig. 4.3 (c) these results constitute an impressive – albeit indirect – demonstration of the credibility of our numerical predictions despite the fact that, understandably, it is not possible to directly measure (super-)sonic air speeds with our smoke setup.

Looking more closely at the velocity profile above the neck (see Fig. 4.4 (b)) one finds that it possesses a discontinuous jump: the signature of a shock front developing

in the air stream. While such a shock front is a common phenomenon in steady supersonic flows, here we are able to illustrate its development even in our highly unsteady situation when the gas velocity passes from sub- to supersonic. Note that due to our one-dimensional approximation possible cross-shocks are not captured by the present approach.

## 4.5 Conclusion

In conclusion, we showed that the air flow inside the impact cavity formed by a solid object hitting a liquid surface attains supersonic velocities. Surprisingly, we found that the very high air speeds can be reached even though the pressure inside the cavity is merely 2% higher than the surrounding atmosphere. This is due to the highly unsteady gas flow created by the rapidly deforming cavity. We illustrated how the air affects the cavity shape close to the final collapse in two different ways: (i) the initially smoothly curved neck shape acquires a kink-like which can be attributed to a Bernoulli suction effect and (ii) the initially downward motion of the neck reverses its direction and starts to travel upwards. The quantitatively consistent observation of both effects in numerics and experiment makes us confident that our rather involved numerical procedure truthfully reflects reality.

## Appendix: Experimental methods

### Experimental Setup

A large glass tank with a base area of 50 by 50 cm and 100 cm high is half-filled with water. Through the bottom of the tank runs a thin rod (diameter 6 mm) which is attached to a linear motor below the water tank. At the other end of the rod a circular disc is mounted. The linear motor pulls down the disc which then impacts on the water surface at constant speed. Just before the experiment is performed, a small amount of smoke is blown into the tank. As the disc enters the water, it drags along the the smoke which then fills the surface cavity.

A compact diode laser line generator (Larisis Magnum II, 665 nm, 1500 mW) is mounted 14 cm above the water surface, allowing the laser light to enter the cavity without traveling through a water/air interface. The laser illuminates a thin vertical sheet of the smoke inside the cavity. A high speed camera (Photron SA1.1) is placed at the side of the tank, perpendicular to the laser sheet in order to record the light that is reflected by the smoke particles (see Fig. 4.6).

## Inertial effects on smoke particles

In order to demonstrate that inertial effects of the smoke particles can be neglected we perform a simple analysis to predict how well the smoke particles will follow the air flow. The typical size of the spherical smoke particles is measured using a microscope to be roughly 3 $\mu$m. At a velocity difference of 10 m/s the Reynolds number is 2, meaning we can assume Stokes drag $D$, which is for a spherical particle:

$$D = 3\pi\rho_g \nu_g d_p \Delta U \tag{4.2}$$

where $\rho_g$ and $\nu_g$ are the gas density and viscosity respectively, $d_p$ the particle diameter and $\Delta U$ the velocity difference between the particle and the air. Knowing the force on the particles and the mass of the particle we can calculate the movement of a particle in an accelerating flow. We find that the particle follows the flow up to 25 m/s with a velocity lag less than 2%.

## Image processing

The goal of the image processing is to determine the speed of the air inside the cavity. Note that we do not see separate smoke particles, but we rely on visible structures in the smoke. The steps that we take can be divided in pre-processing, correlation and post-processing. While correlation and post-processing are done with standard procedures [27], the pre-processing is not straightforward and is explained here.

While the laser sheet enters the cavity from the top without passing through the air/water interface, the light that is reflected by the smoke particles needs to cross the cavity interface on its way to our camera. This interface, however, is not perfectly smooth but exhibits small disturbances which in turn become visible in our recordings. Regular background subtraction fails in this case because the disturbances are not completely stationary but slowly evolve in time. Since the smoke particles are moving much faster we can subtract subsequent images which eliminates the (almost stationary) disturbances while the rapid motion of the smoke patterns remains visible.

The drawback of this subtraction technique is that it breaks down when the speed of the smoke patterns and the surface disturbances become comparable, see the missing part around $u_{\text{gas}} = 0$ in Fig. 2 of the main article. To some extent we can detect slow movements by not taking subsequent frames, but by taking frame $n$ and $n+m$, where $m$ is 2, 4, 8 or 16.

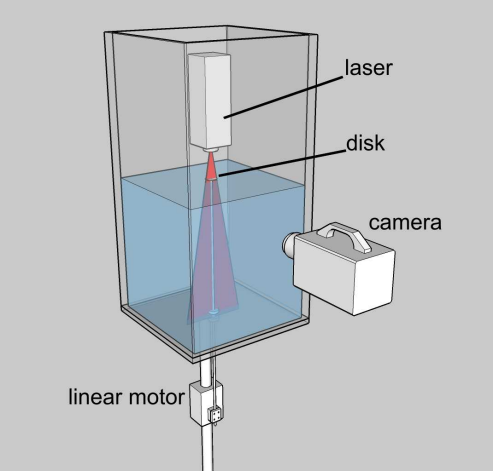


Figure 4.6: Illustration of the experimental setup.

## References

[1] A. M. Worthington, *A study of splashes* (Longmans, Green and Co., London) (1908).

[2] D. Gilbarg and R. A. Anderson, "Influence of atmospheric pressure on the phenomena accompanying the entry of spheres into water", J. Appl. Phys. **19**, 127–139 (1948).

[3] A. May, "Effect of surface condition of a sphere on its water-entry cavity", J. Appl. Phys. **22**, 1219–1222 (1951).

[4] A. May, "Vertical entry of missiles into water", J. Appl. Phys. **23**, 1362–1372 (1952).

[5] H. I. Abelson, "Pressure measurements in the water-entry cavity", J. Fluid Mech. **44**, 129–144 (1970).

[6] J. W. Glasheen and T. A. McMahon, "Vertical water entry of disks at low froude numbers", Phys. Fluids **8**, 2078–2083 (1996).

[7] M. Lee, R. G. Longoria, and D. E. Wilson, "Cavity dynamics in high-speed water entry", Phys. Fluids **9**, 540–550 (1997).

[8] S. Gaudet, "Numerical simulation of circular disks entering the free surface of a fluid", Phys. Fluids **10**, 2489–2499 (1998).

[9] R. Bergmann, D. van der Meer, M. Stijnman, M. Sandtke, A. Prosperetti, and D. Lohse, "Giant bubble pinch-off", Phys. Rev. Lett. **96**, 154505 (2006).

[10] V. Duclaux, F. Caillé, C. Duez, C. Ybert, L. Bocquet, and C. Clanet, "Dynamics of transient cavities", J. Fluid Mech. **591**, 1–19 (2007).

[11] D. Vella and P. D. Metcalfe, "Surface tension dominated impact", Phys. Fluids **19**, 072108 (2007).

[12] C. Duez, C. Ybert, C. Clanet, and L. Bocquet, "Making a splash with water repellency", Nature Physics **3**, 180–183 (2007).

[13] S. Gekle, A. van der Bos, R. Bergmann, D. van der Meer, and D. Lohse, "Non-continuous froude number scaling for the closure depth of a cylindrical cavity", Phys. Rev. Lett. **100**, 084502 (2008),
*See Chapter 7 of this thesis.*

[14] S. Gekle, J. M. Gordillo, D. van der Meer, and D. Lohse, "High-speed jet formation after solid object impact", Phys. Rev. Lett. **102**, 034502 (2009),
*See Chapter 2 of this thesis.*

[15] J. M. Aristoff and J. W. M. Bush, "Water entry of small hydrophobic spheres", J. Fluid Mech. **619**, 45–78 (2009).

[16] R. Bergmann, D. van der Meer, S. Gekle, A. van der Bos, and D. Lohse, "Controlled impact of a disc on a water surface: Cavity dynamics", J. Fluid Mech. **633**, 381–409 (2009).

[17] M. Do-Quang and G. Amberg, "The splash of a solid sphere impacting on a liquid surface: Numerical simulation of the influence of wetting", Phys. Fluids **21**, 022102 (2009).

[18] L. E. Schmidt, N. C. Keim, W. W. Zhang, and S. R. Nagel, "Memory-encoding vibrations in a disconnecting air bubble", Nature physics **5**, 343–346 (2009).

[19] K. S. Turitsyn, L. Lai, and W. W. Zhang, "Asymmetric bubble disconnection: persistent vibration evolves into smooth contact", arXiv:0902.0393v1 [physics.flu-dyn] (2009).

[20] J. Rodríguez-Rodríguez, J. M. Gordillo, and C. Martínez-Bazán, "Breakup time and morphology of drops and bubbles in a high-reynolds-number flow", J. Fluid Mech. **548**, 69–86 (2006).

[21] C. Laney, *Computational gasdynamics* (Cambridge University Press) (1998).

[22] P. L. Roe, "Approximate Riemann solvers, parameter vectors, and difference schemes", J. Comput. Phys. **43**, 357–372 (1981).

[23] B. Godderidge, S. Turnock, C. Earl, and M. Tan, "The effect of fluid compressibility on the simulation of sloshing impacts", Ocean Eng. **36**, 578–587 (2009).

[24] H. W. Liepmann and A. Roshko, *Elements of gas dynamics* (Wiley) (1957).

[25] J. M. Gordillo, A. Sevilla, J. Rodríguez-Rodríguez, and C. Martínez-Bazán, "Axisymmetric bubble pinch-off at high reynolds numbers", Phys. Rev. Lett. **95**, 194501 (2005).

[26] R. Bergmann, A. Andersen, D. van der Meer, and T. Bohr, "Bubble pinch-off in a rotating flow", Phys. Rev. Lett. **102**, 204501 (2009).

[27] M. Raffel, C. Willert, S. Wereley, and J. Kompenhans, *Particle Image Velocimetry, A Practical Guide* (Springer) (2007).

# 5

# Numerical modeling of compressible air flow through a collapsing liquid cavity *

*We present a multiphase approach to simulate the impact of a solid object on a liquid surface: upon impact a thin liquid sheet is thrown upwards all around the rim of the impactor while in its wake a large surface cavity forms. Under the influence of hydrostatic pressure the cavity immediately starts to collapse and eventually closes in a single point from which a thin, needle-like jet is ejected. Existing numerical treatments of liquid impact either consider the surrounding air as an incompressible fluid or neglect air effects altogether. In contrast, our approach couples a boundary-integral method for the liquid with a Roe scheme for the gas domain and is thus able to handle the fully compressible gas stream that is pushed out of the collapsing impact cavity. Taking into account air compressibility is crucial, since, as we show in this work, the impact crater collapses so violently that the air flow through the cavity neck attains supersonic velocities – even though the object impacts at only 1 m/s. At the same time, the cavity pressure is merely 2% higher than the surrounding atmosphere and thus much lower than the overpressures usually observed in supersonic flow through a nozzle in conventional aerodynamics. The key difference is that in our case the confining cavity is a liquid which is rapidly evolving in time. We validate our computational results by comparing with corresponding experimental data.*

*To be submitted as: Stephan Gekle and José Manuel Gordillo, "Numerical modeling of compressible air flow through a collapsing liquid cavity", J. Comput. Phys. (2009).

## 5.1 Introduction

The thin jet ejected after the impact of an object on a liquid surface has been one of the icons of fluid mechanics since the days of Worthington more than a century ago [1]. Since then a fair amount of computational studies on the impact of liquid drops [2–7] or solid objects [8–17] has been reported. In these works a number of different methods have been employed including Arbitrary-Langrangian-Eulerian, Boundary-Integral, Volume-of-Fluid, Level-Set, or combinations thereof. Despite this variety a common feature is that the dynamics of the surrounding air was either neglected altogether [2, 3, 8–16] or it was treated as an incompressible fluid [4–7, 17] in the regime for low Mach numbers.

In this work we report a seemingly simple and harmless situation which nevertheless requires to model the dynamics of the gas phase in a fully compressible way: a circular disc of 2 cm radius which impacts on a liquid surface with a speed of 1 m/s. Figure 5.1 illustrates the sequence of events during the disc impact extracted from high-speed video images [16, 18] and compared to the results of our simulations. Upon impact, first a thin liquid splash is thrown up all around the circumference of the penetrating disc. In the wake of the impactor a large cavity is created which subsequently starts to collapse due to the hydrostatic pressure of the surrounding liquid. When the cavity closes about half-way down its length two very fast and thin jets are observed shooting up- and down from the closure point [15, 19–21].

In the beginning of the process, obviously, air is drawn into the cavity by the moving disc. At a later stage, however, this inward flow is counteracted by the shrinking of the cavity volume itself and the direction of air flow is not a priori clear. We will show that in the competition between cavity expansion (just above the disc) and shrinking (around the neck), eventually the shrinking becomes dominant. Accordingly, the air flow through the neck reverses and air is pushed out of the cavity. The collapse is so violent that the air stream can attain *supersonic* speeds. To handle this situation, we implement an axisymmetric boundary-integral method (BIM) to simulate the motion of the liquid surface which is two-way coupled with a fully compressible Roe solver for the highly unsteady gas flow.

In Section 5.2 we will introduce briefly our BIM and Roe implementations and then describe in detail the two-way coupling between the BIM for the liquid and the Roe scheme for the gas domain. Sections 5.3.1 and 5.3.2 show the main physical results extracted from our simulations and Section 5.3.3 describes the experimental validation of our computational method. Section 5.4 concludes the chapter.

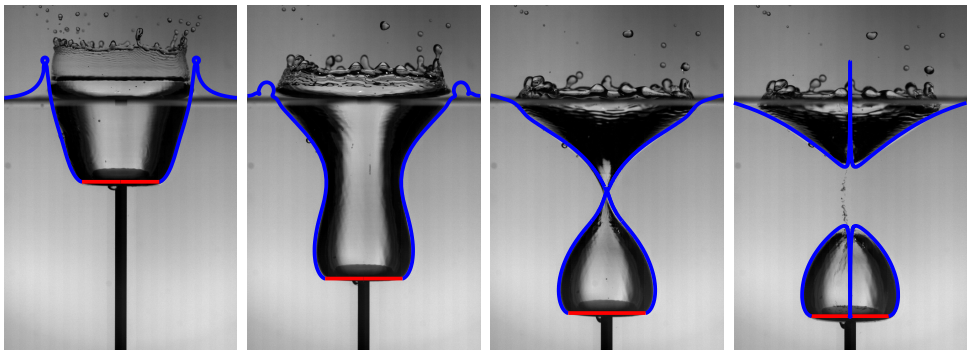

Figure 5.1: The sequence of events as a circular disc of 2 cm radius impacts a water surface at 1 m/s: (a) Immediately after impact a crown splash is thrown up into the air and an impact cavity forms below the free surface. The moving disc draws air into the cavity. (b) Hydrostatic pressure pushes the cavity together and the direction of air flow reverses. (c) Eventually the cavity closes in a single point. (d) After closure two violent jets are ejected up- and downwards from the closure location (simulation data from [15]). The blue and red lines represent the free surface and the disc, respectively, from our numerical simulation.

## 5.2 Numerical methods

In the impact process viscous effects are negligible as can be seen by estimating the Reynolds numbers for gas and liquid as $\mathrm{Re}_{g,l} = V_0 R_0 / \nu_{g,l}$. Here, $V_0 = 1$ m/s is the impact speed, $R_0 = 2$ cm is the disc radius, and $\nu_g = 1.46 \cdot 10^{-5}$ m$^2$/s and $\nu_l = 1.12 \cdot 10^{-6}$ m$^2$/s are the dynamic viscosities of gas and liquid at 15°C, respectively. Both $\mathrm{Re}_g$ and $\mathrm{Re}_l$ are larger than $10^3$ and viscosity is thus negligible. Furthermore, we showed in earlier works [16] that only a negligible amount of vorticity is present in the system. We can thus assume the flow to be inviscid and irrotational as is required for the boundary-integral method and the applicability of the inviscid Euler equations.

Our simulation is split in two stages. In the first, incompressible stage, a two-fluid boundary integral method is used to simulate the first part of the impact and cavity collapse where gas velocities are of the order of the disc velocity. In the second, compressible stage, we use a single-fluid BIM for the liquid coupled to a Roe scheme to solve the compressible Euler equations in the gas domain.

The transition between both stages is fixed at the moment that the air flow through

the cavity neck reverses and $u_{\text{neck}} = 0$. [†]

At the transition moment the liquid cavity has an elongated shape with a neck located roughly at the middle as can be seen in Fig. 5.1 (b). Furthermore, the gas flow is to a very good approximation one-dimensional directed along the symmetry axis of the cavity (as can be verified by flow profiles obtained from the two-fluid BIM shown in Section 5.3.1). This makes the situation reminiscent of gas flow through a converging-diverging de-Laval nozzle frequently encountered in aerodynamics [22]. In this spirit, we remove the inner potential fluid during the compressible stage and replace it with a compressible gas described by the one-dimensional Euler equations. To integrate Euler's equations in time we use the well-known scheme due to Roe [23]. This description is valid along most of the cavity. Above the initial free surface as well as in a small zone above the disc the air dynamics can be neglected as will be described in Section 5.2.3. The pronounced difference to the standard nozzle situation, however, is that in our case the "nozzle" geometry is determined by a *liquid* interface which is changing rapidly in time and thus creates a highly unsteady gas flow.

The two-way coupling between the gas and the liquid domains is accomplished via (i) the interfacial shape and its instantaneous velocity which is provided by the BIM and serves as an input into the gas solver and (ii) the gas pressure which is obtained from the solution of the Euler equations and serves as a boundary condition for the BIM. Above the location of the initial water level the surface pressure of the BIM remains atmospheric.

All quantities are non-dimensionalized with the disc radius $R_0 = 2$ cm and the impact velocity $V_0 = 1$ m/s. As a third quantity for non-dimensionalization we use the density of water $\rho_l = 998.23$ kg/m$^3$ for the equations concerning the liquid domain and the density of air (at rest under atmospheric pressure) $\rho_g = 1.2$ kg/m$^3$ for the gas equations. Since viscosity is neglected we have four dimensionless parameters which are the Froude number, the Weber number, the Euler number for the liquid, and the

[†]The transition point can of course also be taken somewhat later as long as gas velocities are still low enough to neglect compressibility. We tried $u_{\text{neck}} = 10$, 20, and 50 m/s which all give similar results.

Euler number for the gas defined as:

$$\mathrm{Fr} = \frac{V_0^2}{gR_0} \tag{5.1}$$

$$\mathrm{We} = \frac{\rho_l R_0 V_0^2}{\sigma} \tag{5.2}$$

$$\mathrm{Eu}_l = \frac{p_a}{\rho_l V_0^2} \tag{5.3}$$

$$\mathrm{Eu}_g = \frac{p_a}{\rho_g V_0^2}. \tag{5.4}$$

with the atmospheric pressure $p_a = 101.3$ kPa, the acceleration of gravity $g = 9.81$ m/s$^2$, and the air/water surface tension $\sigma = 72.8$ mN/m. We use cylindrical coordinates $r$ and $z$ with $z = 0$ at the height of the initial free surface as is appropriate for our axisymmetric setup. In all computations the disc is assumed to have zero thickness.

The boundary-integral method for a single fluid (liquid) is briefly sketched in 5.2.1 and its extension to two fluids (liquid and air) is given in 5.2.1. Some important aspects of our specific BIM implementation are described in 5.2.1. The Roe solver is, again briefly, presented in Section 5.2.2. In Section 5.2.3 we describe the coupling between the gas and liquid domains during the compressible stage.

### 5.2.1 Boundary integral formulation

#### Boundary integral method for a single fluid

If liquid flow is inviscid and irrotational as is the case in our setup [15, 16] the flow field $\vec{v}$ can be described as the gradient of a scalar potential $\phi$

$$\vec{v} = \nabla\phi \tag{5.5}$$

which satisfies Laplace's equation throughout the liquid domain

$$\Delta\phi = 0. \tag{5.6}$$

From Eq. (5.6) the boundary-integral equation can be derived using Green's identities [24]:

$$\beta\,\phi\left(\vec{r}\right) = \int_S \left[\frac{1}{\left|\vec{r}-\vec{r}'\right|}\phi_n\left(\vec{r}'\right) - \phi\left(\vec{r}'\right)\vec{n}\cdot\nabla'\frac{1}{\left|\vec{r}-\vec{r}'\right|}\right] dS' \tag{5.7}$$

with $S$ denoting the boundary, $\vec{n}$ the normal vector pointing out of the liquid domain, and $\phi_n = \vec{n}\cdot\nabla\phi$ the normal derivative of the potential along the boundary. Equation (5.7) expresses the potential $\phi$ at an arbitrary point $\vec{r}$ inside the domain (then

$\beta = 4\pi$) or on its edge (then $\beta = 2\pi$) merely in terms of quantities that are defined on the surface of the liquid domain. This has the major advantage that it is sufficient to evolve the surface quantities $\phi$ and $\phi_n$ effectively reducing the computational problem by one spatial dimension.

If on every point along the interface either $\phi$ or $\phi_n$ is known, Eq. (5.7) can be solved for the missing quantity such that afterwards both $\phi$ and $\phi_n$ are available along the entire boundary. With this the interfacial velocity can be computed as

$$\vec{v} = \frac{\partial \phi}{\partial s}\vec{t} + \phi_n \vec{n} \tag{5.8}$$

with $\partial/\partial s$ denoting the tangential derivative and $\vec{t}$ the tangential vector along the surface. The numerical procedure for this is sufficiently well described in the literature [24–26] and the details of the present implementation will be given in Section 5.2.1.

The boundary conditions for solving Eq. (5.7) are provided as follows: on the disc the liquid is required to follow the disc's motion meaning that $\phi_n = -1$ in non-dimensional coordinates. On the air/liquid interface the potential $\phi$ is specified by integrating Bernoulli's equation:

$$\frac{D\phi}{Dt} = \frac{1}{2}|\vec{v}|^2 - \mathrm{Eu}_l\left(\mathrm{Eu}_g^{-1} p - 1\right) - \frac{1}{\mathrm{Fr}} z - \frac{1}{\mathrm{We}} C \tag{5.9}$$

with $D/Dt = \partial/\partial t + \vec{v}\cdot\nabla$ denoting the material derivative, $C = \nabla\cdot\vec{n}$ the local curvature of the interface. The dimensionless gas pressure is $p = p_g/\left(\rho_g V_0^2\right)$ with the dimensional gas pressure $p_g$. Here we assume that the pressure is atmospheric at a point far away from the symmetry axis where the flow is quiescent.

In total, the boundary-integral simulation for a single fluid contains three substeps to advance from time step $j$ to $j+1$ [24–26]. First, with the velocity $v^{(j)}$ we integrate Bernoulli's equation (5.9) to compute the potential $\phi_f^{(j+1)}$ along the free surface. Next, we solve the boundary-integral equation (5.7) to obtain the liquid potential over the disc $\phi_d^{(j+1)}$ and the normal derivative of the potential over the free surface $\phi_{n,f}^{(j+1)}$. The third step updates the position of the free surface by integrating

$$\frac{d\vec{r}}{dt} = \vec{v} \tag{5.10}$$

and moves the disc downwards with its prescribed velocity. Then the process repeats.

### Boundary-integral method for two fluids

The BIM can be extended to describe two immiscible fluids with a moving interface separating both phases. Our approach closely follows that of [27, 28] and is thus only

briefly sketched here. The liquid and gas phase both satisfy the boundary-integral equation (5.7) within their respective domains. At the interface between the two fluids tangential stresses vanish since the fluids are inviscid, i.e., the fluids can slip freely along the boundary. To ensure continuity of the interface, however, the normal velocities of both phases must exactly balance

$$\phi_n = -\phi_{n,g} \tag{5.11}$$

with $\phi_{n,g}$ being the normal derivative of the gas potential and $\phi_n$ that of the liquid as defined above. The minus sign is due to the normal vector pointing always out of the respective domains. Furthermore, the pressure jump across the interface is given by the Laplace pressure. These two conditions are sufficient to derive the two-fluid version of the BIM [27, 28].

**Specific implementation of the boundary-integral method**

In our axisymmetric situation the surface integrals in Eq. (5.7) can be reduced to one-dimensional line integrals in the $(r, z)$-plane after analytical integration over the azimuthal angle. Numerical integration is carried out using 8-point Gaussian quadrature with the weak logarithmic singularities removed analytically as in [26]. Between the nodes the interface shape and potentials are interpolated using cubic splines with the node-to-node distance serving as the spline parameter $s$. Natural boundary conditions (i.e. a vanishing second derivative with respect to $s$) are used for all splines, except for the potential at the connection between the disc's edge and the free surface as described below. Once the known integrals in Eq. (5.7) are evaluated we transform Eq. (5.7) into a matrix equation which is solved by LU decomposition [25, 26].

Time-stepping for the integration of Eqs. (5.9) and (5.10) is carried out by an iterative Crank-Nicholson procedure during the incompressible stage. In the compressible stage, we use a simpler forward-Euler scheme for ease of coupling between the BIM and the Roe solver in the two respective domains. The time step in the incompressible stage is determined by the condition that neighboring nodes may not collide even if their velocities were directed exactly towards each other. This leads to:

$$\Delta t' = f \cdot \min_i (d_i / v_i) \tag{5.12}$$

with $i$ running over all nodes, $v_i$ the free surface velocity at node $i$, and $d_i$ the distance to the neighboring node. This quantity is multiplied with a safety factor $f$ which is in most simulations chosen to be 0.1. In the compressible stage the time-step is determined by the stability condition of the Roe solver as described in the next section.

To ensure a continuous boundary of the liquid domain the last node of the free surface remains fixed at the disc's edge. This connection point requires some special consideration. First, the surface is not smooth and thus the prefactor $\beta$ in Eq. (5.7) must be modified to become $\beta = 2\alpha$ for the liquid and $\beta = 2\pi - 2\alpha$ for the gas equations. Here, $\alpha$ is the angle connecting the horizontal disc and the tangent to the free surface at the connection point through the liquid domain (i.e. $\alpha > \pi$ in our situation). Second, the connection point is at the same time the last node $\mathscr{F}$ of the free interface and the first node $\mathscr{D}$ of the disc. To solve Eq. (5.7) we consider it part of the disc, i.e. we impose $\phi_n = -1$ and obtain the corresponding value for $\phi$. Together with the pinning at the disc's edge, the position $\vec{r}$ and the liquid velocity $\vec{v}$ at $\mathscr{D}$ are thus completely determined. We then need to ensure that $\mathscr{F}$ and $\mathscr{D}$ remain identical. For this we first copy the spatial coordinates of $\mathscr{D}$ on $\mathscr{F}$. To ensure further that also the velocity $\vec{v}$ is identical on both nodes we project $\vec{v}$ on the tangential and normal vectors of the free surface at $\mathscr{F}$ which determines the values of $\phi_n$ and $\partial\phi/\partial s$. The latter is imposed as a boundary condition on the spline function for $\phi$. This procedure ensures that the velocity $\vec{v}$ of the connection point is identical when seen from the disc or from the free surface, even though the respective normal and tangent vectors are discontinuous.

In our simulations the free surface extends from the edge of the disc at $r = 1$ out to 100 where any motion is negligible and the surface is cut off. Note that BIMs do not require a closed liquid domain since the portion of $S$ at infinity gives no contribution to Eq. (5.7) provided that $\phi$ goes to zero there. We use an adaptive mesh to ensure that the sensitive areas such as the crown splash or the cavity neck are properly resolved without wasting computation time by placing a large amount of nodes on unimportant parts. During the incompressible stage the local node distance $d$ is inversely proportional to the local curvature $C$ with a proportionality constant between 0.05 and 0.005. We impose a maximum distance ($d_{\max} = 10$) and minimum distance ($d_{\min} = 0.01$) and construct our regridding algorithm such that large gradients in the node density, which might cause instabilities, are avoided. When coupling with the Euler solver during the compressible stage, the BI mesh corresponds to the grid cells used for the Roe scheme as will be described in Section 5.2.3. Note that then we also allow for node distances smaller than $d_{\min}$.

Boundary-integral methods are known to be vulnerable to instabilities (see e.g. [2]) due to the lack of a naturally damping viscosity which prevents small numerical disturbances from building-up over time. To handle such instabilities we use a smoothing algorithm as follows: At every $n$th (usually $2 \leq n \leq 10$) time step the free surface nodes are redistributed such that new nodes fall exactly half-way between old nodes as illustrated in Fig. 5.2 (a). This periodic regridding procedure efficiently ensures

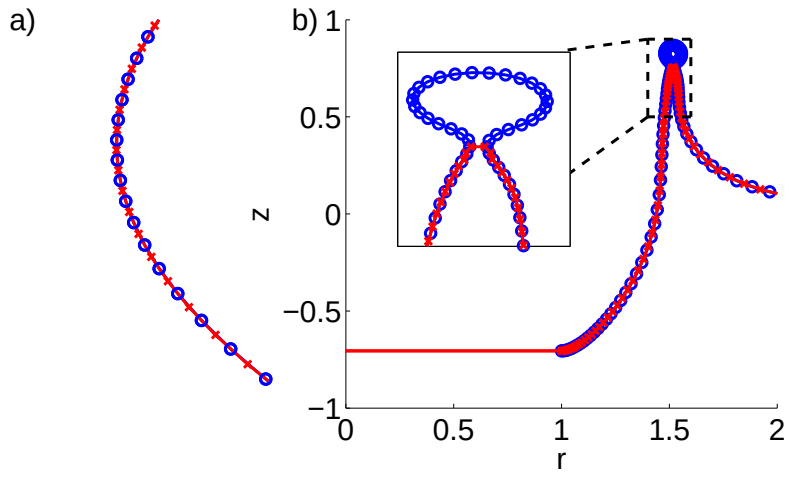


Figure 5.2: (a) Illustration of the regridding procedure: every $n$ time steps the surface is reconstructed with the new nodes (red crosses) shifted to lie halfway between the old nodes (blue circles) in order to avoid amplification of small numerical disturbances. (b) The thin liquid sheet ejected after impact breaks up into droplets which are cut off and discarded as illustrated by the blue line (circles) before and the red line (crosses) after cut-off.

the stability of the numerical scheme [2].

A specific detail of our physical problem is the thin sheet of liquid thrown up around the rim of the impacting disc (see Fig. 5.1 (a)). In reality, this sheet will quickly develop non-axisymmetric instabilities leading to the formation of individual droplets earning it the title of a “crown splash” as seen, e.g., in the famous pictures of [1]. As here we are not interested in the details of this splash and our axisymmetric code is not able to handle the droplet formation in any case, we cut off the splash as soon the distance between the two sides of the liquid sheet at a given point falls below the local node distance as illustrated in Fig. 5.2 (b). The actual surface surgery is similar to the one used in [15] to handle the pinch-off of the cavity prior to jet formation.

### 5.2.2 Roe method for a compressible gas

In the compressible stage the inner gas is described by the one-dimensional Euler equations for conservation of mass, momentum, and energy:

$$\frac{\partial(\rho S)}{\partial t} + \frac{\partial(\rho u S)}{\partial z} = 0 \tag{5.13}$$

$$\frac{\partial(\rho u S)}{\partial t} + \frac{\partial\left(pS + \rho u^2 S\right)}{\partial z} = p\frac{\partial S}{\partial z} \tag{5.14}$$

$$\frac{\partial(\rho E S)}{\partial t} + \frac{\partial(\rho u H S)}{\partial z} = -p\frac{\partial S}{\partial t}. \tag{5.15}$$

All quantities are dimensionless and $S$ is the cross-sectional area of the cavity, $\rho$ the gas density, $u$ the velocity, and $p$ the gas pressure as defined for Eq. (5.9). The total energy $E$ per unit mass is defined as

$$E = \frac{1}{\gamma - 1}\frac{p}{\rho} + \frac{1}{2}u^2 \tag{5.16}$$

and the total enthalpy $H$, again per unit mass, is

$$H = E + \frac{p}{\rho}. \tag{5.17}$$

Note the two source terms $p\partial S/\partial z$ and $-p\partial S/\partial t$ on the right-hand side which account for a cavity radius which is changing in space and time.

Integration of Eqs. (5.13)–(5.15) is carried out using a Roe scheme [22, 23] whose implementation is fairly standard and thus omitted here.

The time step during the compressible stage is restricted by the Courant-Friedrich-Lewy (CFL) stability condition for the Roe solver. We fix a constant CFL number $C^* < 1$ (usually $C^* = 0.5$) and determine the time step by:

$$\Delta t = C^* \frac{\Delta z}{\max_i\left(|u_i| + c_i\right)} \tag{5.18}$$

with the cell size $\Delta z$ and the index $i$ running over all cells.

One detail that is of interest are the boundary conditions at the upper and lower end of the cavity. In contrast to the standard problem of flow through a nozzle which possesses an inlet on one side and an outlet on the other side, in our case gas leaves the (shrinking) cavity on both sides. Since both outflows are subsonic we can prescribe one flow quantity at each boundary [22]. To compute the flux through the lower (upper) face of the first (last) computational cell we add a boundary cell at each end whose state values are calculated as follows.

At the upper exit we impose that the pressure in the boundary cell be atmospheric. In order to compute the density and velocity of the boundary cell, let $\rho_N$, $u_N$, and $p_N$ be the components of the state vector, and $c_N = \sqrt{\gamma p_N/\rho_N}$ the local speed of sound in the last computational cell. Assuming that the discharge proceeds isentropically and that the $I^+$ characteristic

$$I^+ = \frac{2}{\gamma-1}c + u \tag{5.19}$$

transporting information out of the computational domain is conserved, we have for the values of the upper boundary (ub) cell:

$$\rho_{ub} = \rho_N \left(\frac{p_{ub}}{p_N}\right)^{1/\gamma} \tag{5.20}$$

$$u_{ub} = \frac{2}{\gamma-1}(c_N - c_{ub}) + u_N \tag{5.21}$$

$$p_{ub} = \frac{p_a}{\rho_g V_0^2} = \mathrm{Eu}_g. \tag{5.22}$$

At the bottom exit we impose the velocity $u_e$ with which the gas leaves the computational (Euler) domain. Since velocities between this point and the disc are small (see Section 5.2.3) conservation of mass allows us to calculate this velocity from the rate of change in cavity volume between the disc and the boundary cell, i.e. $u_e = \int_{S_b} \phi_n dS_b/R_e^2$ with the surface $S_b$ including the disc itself and $R_e$ the cavity radius at the boundary cell. Similarly as at the upper exit, the state of the lower boundary (lb) cell can then be computed from the state of the first computational cell ($\rho_1$, $u_1$, $p_1$) using conservation of the $I^-$ characteristic:

$$\rho_{lb} = \gamma\frac{p_{lb}}{c_{lb}^2} \tag{5.23}$$

$$u_{lb} = u_e \tag{5.24}$$

$$p_{lb} = \left[\left(\frac{\gamma}{c_{lb}^2}\right)^{\gamma}\frac{p_1}{\rho_1^{\gamma}}\right]^{1/(1-\gamma)} \tag{5.25}$$

$$c_{lb} = c_1 - (u_1 - u_e)\frac{\gamma-1}{2}. \tag{5.26}$$

These boundary conditions cannot completely prevent reflection of waves at the upper and lower ends which causes some small oscillations in the state variables $\rho$, $u$, and $p$ as can be seen for example in Fig. 5.4 (b). The oscillations however remain sufficiently small so that the averaged evolution of the gas dynamics can still reliably be extracted.

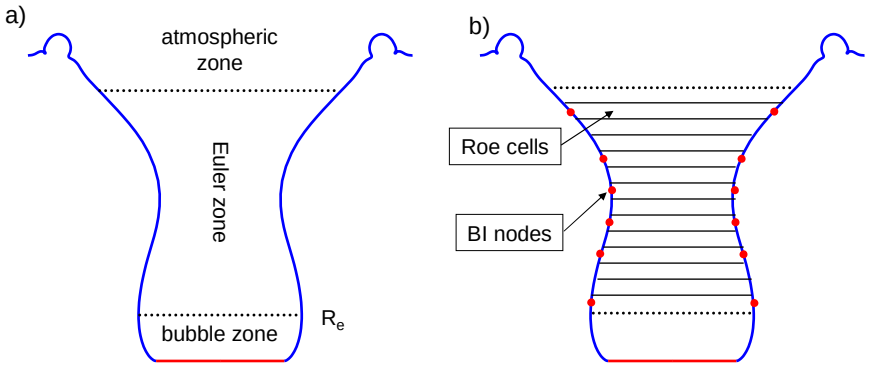


Figure 5.3: (a) Illustration of the three zones in which the gas domain is split during the compressible stage: in the "atmospheric zone" on top, the pressure is always atmospheric and the gas dynamics are neglected. In the "Euler zone" we use the Roe scheme to calculate the fully compressible gas dynamics. In the "bubble zone" again the pressure is constant and given by the pressure at the end of the Euler zone. (b) Schematic illustration of the alignment of Euler cells and BI nodes: the BI nodes are always placed at the height of the center of the Euler cells. In the neck area a BI node is placed in every 2nd Roe cell, while away from the neck the spacing is larger to save computation time.

### 5.2.3 Coupling between boundary-integral and Roe method

During the compressible stage of the simulation, the gas domain is split into three separate zones as illustrated in Fig. 5.3 (a). The gas pressure which is required for coupling to the BIM is obtained in a different way for each zone. First, in the "atmospheric zone" the pressure is taken to be atmospheric since the gas dynamics is negligible. Next, in the "Euler zone" the pressure is provided by the solution of the Euler equations (5.13)–(5.15). Finally, in the "bubble zone" the gas dynamics is again neglected. The pressure, however, cannot be taken to be atmospheric since the zone is not open to the atmosphere. Due to the low gas velocities in that zone (of order of the disc speed) the pressure is taken equal to the pressure at the bottom end of the Euler zone.

The upper end of the Euler zone can remain at a fixed vertical position (between 0 and 1 disc radii below the initial free surface). The bottom end is fixed to be at the maximum radial extension of the cavity below the neck as depicted in Fig. 5.3 (a). Note that the Euler zone cannot be extended all the way down to the disc since the free surface departs almost horizontally from the disc's edge. This leads to large gradients in the cavity radius on the right-hand side of Eq. (5.14) and can thus cause

numerical instabilities. Since the bottom end of the Euler zone is moving downward in time, its length needs to be extended during the simulation. Our algorithm adds a new Roe cell whenever the distance between the desired location (maximum radial extension of the cavity) and the actual position of the last Roe cell becomes larger than the size of a single cell.

For the results presented here, the initial number of cells in the Roe solver is 600 and grows dynamically by extension of the Euler zone. To ensure sufficient resolution for the high air speeds even during the last moments of the simulation, we double the number of cells by splitting each cell in half whenever the minimum cavity radius $r_{\text{neck}}$ falls below a certain value. This is done twice: at $r_{\text{neck}} = 0.2$ and $r_{\text{neck}} = 0.05$. Due to extension and node doubling the number of Roe cells at the end of the simulation is somewhat above 3000. The height of the Roe cells is always constant with $\Delta z = 0.0012$. We find that the number of Roe cells is not crucial for the total computation time which is mainly determined by the BIM calculations.

It is crucial to properly align the positions of the BI nodes with the Euler cells. For this we place a BI node always exactly in the center of every $n$th Euler cell as illustrated in Fig. 5.3 (b). Usually $n = 2$ in a refined zone around the cavity neck and $n$=5 outside this zone. The cross-sectional area $S$ as well as its spatial and temporal derivatives for each cell are calculated at the height of the cell center from the splines interpolating the cavity surface in the BIM. To avoid numerical instabilities of the BIM we use the periodic regridding described above which now makes the BI nodes "jump" between Euler cells. This implies that there must always be at least one Roe cell without a BI node between two cells which contain a node, i.e. $n \geq 2$.

The two-way coupling between the gas and the liquid domain is accomplished as follows. At each time step $j$ we first do a BI step to advance the shape of the free surface from $j$ to $j+1$ using the gas pressure of step $j$. This is followed by a Roe step using the new cavity shape $j+1$ to obtain the new pressure at $j+1$ and so forth.

We performed an extensive set of simulations to verify that the results presented in the next section are numerically robust when changing any of the above mentioned simulation parameters.

## 5.3 Results

### 5.3.1 Justification of the 1D compressible scheme

In Fig. 5.4 (a) we show the gas velocity through the cavity neck as a function of the shrinking cavity neck $r_{\text{neck}}$ for the incompressible two-fluid BIM. We use $r_{\text{neck}}$ instead of time to allow for an easier comparison with experiments in Section 5.3.3

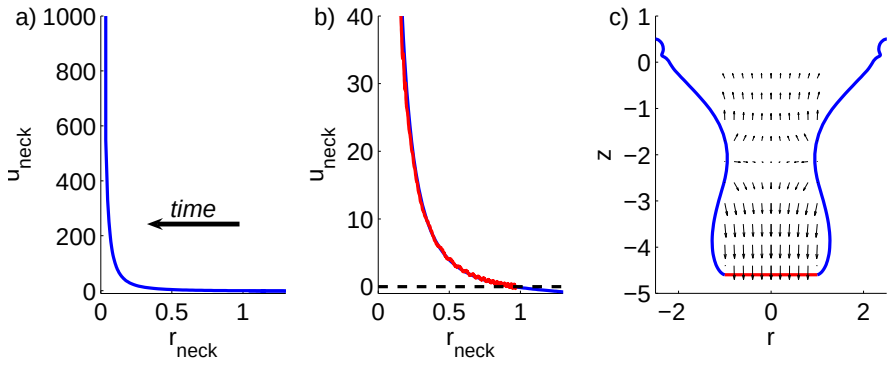


Figure 5.4: (a) The gas velocity at the neck as obtained from an incompressible two-fluid BI simulation. The velocity easily surpasses the speed of sound demonstrating the need for our more sophisticated compressible approach. (b) The velocity obtained from the multiphase simulation (red line) agrees so well with the velocity from the two-fluid BIM (blue line) that both are hardly distinguishable for low velocities where compressibility is negligible. The start of the red curve marks the transition from the incompressible to the compressible stage. The small oscillations in the red curve are due to wave reflections at the ends of the Euler zone. (c) The gas flow field obtained from the two-fluid BIM at the moment when the velocity at the neck reverses and the simulation passes from the incompressible to compressible stage. Except for a rather narrow zone around the neck the flow is to a good approximation one-dimensional.

and [18]. Already at $r_{\text{neck}} = 0.05$ (corresponding to 1 mm) an incompressible gas would surpass the speed of sound. This clearly demonstrates the need for a CFD method which takes the fully compressible gas dynamics into account if one wants to study the ejected air stream close to cavity collapse.

A full two-way coupling is required as both gas and liquid flows occur on similar time scales: We first estimate the typical time scale for the gas flow $T_{\text{gas}}$ as the length of the cavity $L \approx 10$ cm divided by the speed with which a perturbation travels, $c = 330$ m/s, to obtain $T_{\text{gas}} = 0.3$ ms. A typical time scale for the variation of the cavity radius can be derived by considering the time that it takes the cavity to collapse from a neck radius of 4 mm [‡] down to zero which is $T_{\text{cav}} \approx 1$ ms and thus of the same order as $T_{\text{gas}}$.

For some time after switching from the incompressible to the compressible stage

[‡] At $r_{\text{neck}} \approx 4$ mm the vertical neck motion starts to reverse which marks the beginning when air effects become important, see Fig. 4.5 in the previous chapter.

the gas velocities are still moderate and compressibility effects should be negligible. We can thus expect that in the beginning of the compressible stage the gas velocity obtained from our multiphase approach should be similar to the two-fluid BIM in Fig. 5.4 (a). That this is indeed the case is demonstrated in Fig. 5.4 (b) which gives us a first indication that the coupling between the Roe solver and the BIM works correctly. It further gives good evidence that the assumption of one-dimensional gas flow in the compressible stage is justified.

To verify the 1D assumption more explicitly, Fig. 5.4 (c) shows the flow field obtained from the two-fluid BIM at the moment of flow reversal. Except for a small region around the neck where by definition at the moment of flow reversal the vertical velocity is zero, our assumption is well justified.

### 5.3.2 Structure of the compressible gas flow

The intricate structure of the gas flow in the Euler zone is illustrated by the velocity profile in Fig. 5.5 for various instants of time. Here we normalize velocities with the speed of sound to obtain the Mach number Ma=$u/c$. At early times as in Fig. 5.5 (a) one appreciates that at the bottom end of the Euler zone air is entrained by the downward moving disc at velocities of the order of the disc speed. This downflux is however overcompensated by the shrinking of the cavity around the neck so that the total flux is directed upwards as can be seen by the velocity maximum at $z \approx -1.9$. Above the maximum the cavity widens again and the velocity decays towards the upper end of the cavity. The consequence of the competition between cavity expansion at the bottom and cavity collapse around the neck is the creation of a stagnation point with $\mathrm{Ma} = 0$ as is clearly visible in Fig. 5.5 (a).

As the collapse progresses gas is pushed through the rapidly diminishing cavity neck at ever higher and higher speeds leading to a sharp velocity peak at the neck as illustrated in Fig. 5.5 (b). At the top and bottom boundaries of the Euler zone the velocities remain almost unaltered as compared to Fig. 5.5 (a).

Finally, as the flow speed increases even further a shock wave develops upstream of the neck as shown by the magnification in Fig. 5.6. Thanks to the shock-capturing ability of the employed Roe scheme our method is able to handle the shock formation quite well.

Figure 5.7 shows the Mach number at the cavity neck. For our standard configuration of a 2 cm disc impacting at 1 m/s the flow becomes sonic at a neck radius of 0.025 (corresponding to 0.5 mm). Here we also add data for a higher impact speed of 2 m/s which qualitatively shows the same behavior but where sonic flow is attained already at a neck radius of 0.06 (1.2 mm). Once sonic velocities at the neck are reached our numerical scheme becomes unstable which is why do not present any

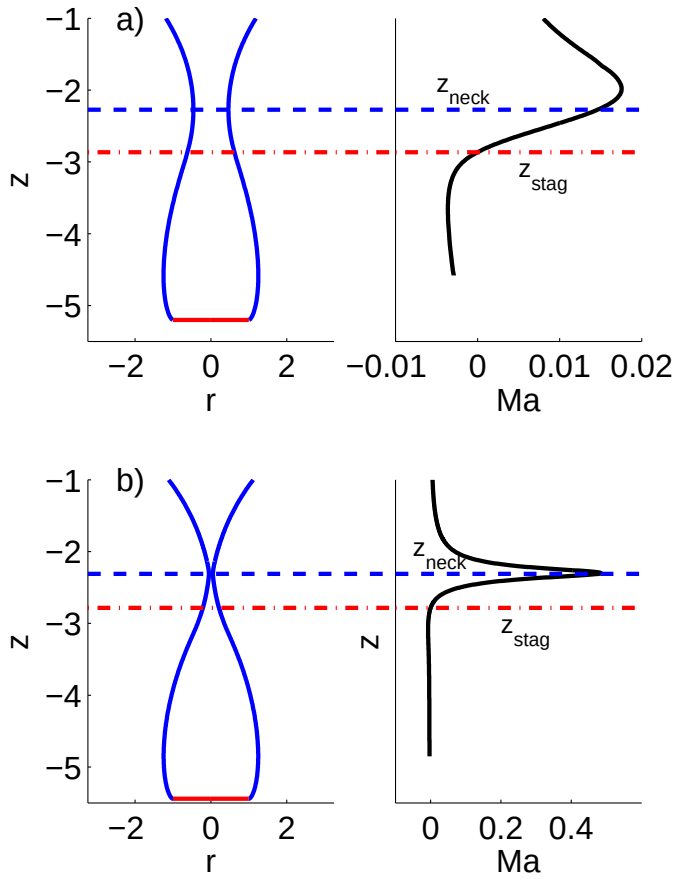


Figure 5.5: The velocity of the gas stream in the Euler zone for various instants of the cavity collapse (right images) with corresponding cavity profiles (left images). (a) In the early stage for neck radii around half a disc radius ($r_{\text{neck}} = 0.46$) the velocity peak is still rather broad. At the bottom end gas leaves the Euler zone with a velocity approximately equal to the disc velocity of -1 which corresponds to Ma=-0.003. Note that the velocity peak is located somewhat upstream of the neck which is marked by the blue dashed line. This is markedly different from steady subsonic flow through a fixed nozzle where both would coincide. The location of the stagnation point is indicated by the red dash-dotted line. (b) At a later time ($r_{\text{neck}} = 0.05$) the velocity peak sharpens and increases in magnitude. The peak is now located almost at the neck.

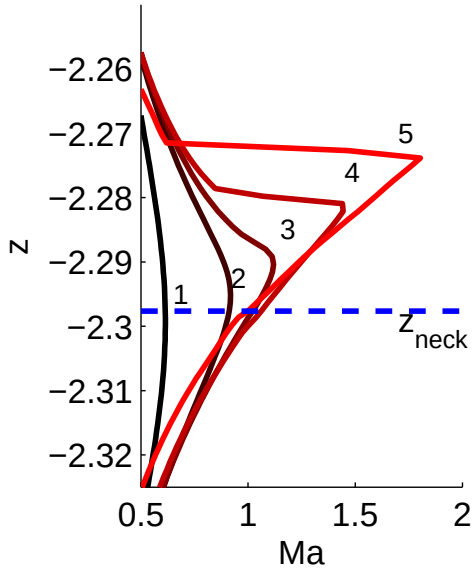


Figure 5.6: A shock wave develops (the numbers 1–5 correspond to neck radii of 0.044, 0.036, 0.034, 0.032 and 0.027; the blue dashed line indicates the neck position for curve number 5). For even smaller neck radii the simulation destabilizes and no reliable data is available.

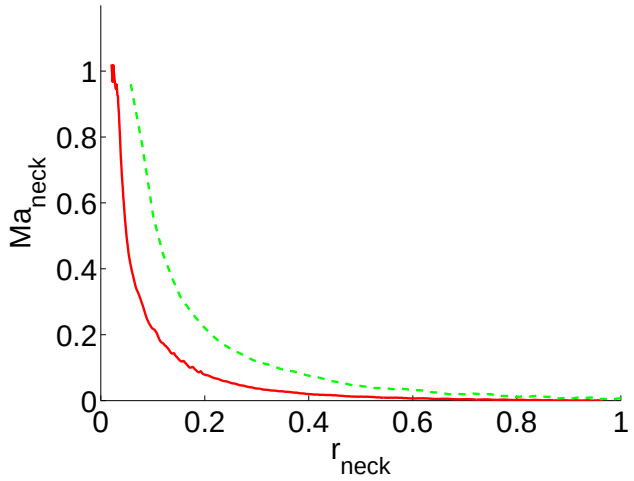


Figure 5.7: The Mach number at the neck for two different impact speeds: 1 m/s (red solid curve) and 2 m/s (green dashed curve). The flow becomes sonic when neck has shrunk to 0.025 or 0.06 disc radii, respectively.

data beyond this point. Note that due to our unsteady situation supersonic speeds are attained even earlier at locations above the neck, cf. Fig. 5.6.

We now turn to study the pressure distribution in the Euler zone which is illustrated in Fig. 5.8. In the early stages of the process (Fig. 5.8 (a)) the pressure remains virtually atmospheric with only a very slight dip around the cavity neck. At a later time, however, the pressure at the neck diminishes substantially as can be seen in Fig. 5.8 (b). In a steady state situation one would expect the neck pressure to reach a minimum value of

$$\frac{p_{g,\mathrm{neck}}}{p_a} = \left(1+\frac{\gamma-1}{2}\right)^{-\gamma/(\gamma-1)} \approx 0.53 \tag{5.27}$$

with $\gamma = 1.4$ the isentropic exponent, as $\mathrm{Ma}_{\mathrm{neck}}$ becomes unity [29]. As shown in Fig. 5.9 (a) our situation – although highly unsteady – exhibits a similar behavior with $p_{g,\mathrm{neck}}/p_a \approx 0.6$ at the final instant before the simulation destabilizes.

Notably, below the neck the pressure is very uniform all the way down to the end of the Euler zone (Fig. 5.9 (a)) which allows us to define a single pressure value for the "bubble" between the neck and the disc. Figure 5.9 (b) demonstrates that in our unique situation of air being pushed through a rapidly shrinking nozzle sonic

speeds can be attained with a bubble pressure which is merely 2% higher than the surrounding atmosphere.

### 5.3.3 Experimental validation

Here we describe briefly the validation of our numerical results with the experimental data of [18] which is achieved in three different ways:

(i) We use smoke particles to directly measure the air speed as it is pushed out of the collapsing cavity. We can reliably measure air speeds up to 10 m/s and very good agreement with the numerical data is found as presented in Fig. 2 of [18].

(ii) In order to confirm the validity of our predictions also for higher gas velocities we compare the numerical cavity shape close to pinch-off with experimental images. We find that the experimental shape is not smoothly curved but exhibits a "kink"-like shape at its neck. This effect – which is due to the low pressure induced by the high gas speeds – is not present in single-fluid simulations, but can be reproduced rather well by the inclusion of air effects as shown in Fig. 3 of [18].

(iii) Finally, we show that the cavity neck in the experiment exhibits a significant upward motion prior to final collapse as the fast air stream pushes the surface minimum upwards. We find very good agreement for this motion between experiment and our multiphase simulations as shown in Fig. 4 of [18].

The quantitatively consistent observation of the above air effects in our compressible simulations and corresponding experiments gives us strong confidence in the reliability of our numerical scheme.

## 5.4 Conclusions

We presented a multiphase model to simulate the impact of a solid object onto a liquid surface. Our focus was on the fast stream of air that is pushed upwards as the impact cavity collapses due to hydrostatic pressure. We showed that in our case of a 2 cm disc impacting at 1 m/s the air attains supersonic velocities and thus requires the use of a fully compressible computational method – in contrast to existing treatments such as Volume-of-Fluid or Level-Set methods [4–7, 17] in which the air flow was considered incompressible.

In our simulations the impact process is split in an incompressible and a compressible stage. During the incompressible stage which covers the first part of the process, air is entrained into the cavity at relatively low speeds (compared to the speed of sound). This allows us to use a two-fluid boundary-integral method for the gas and the liquid domain. The compressible stage starts as the air flow reverses and

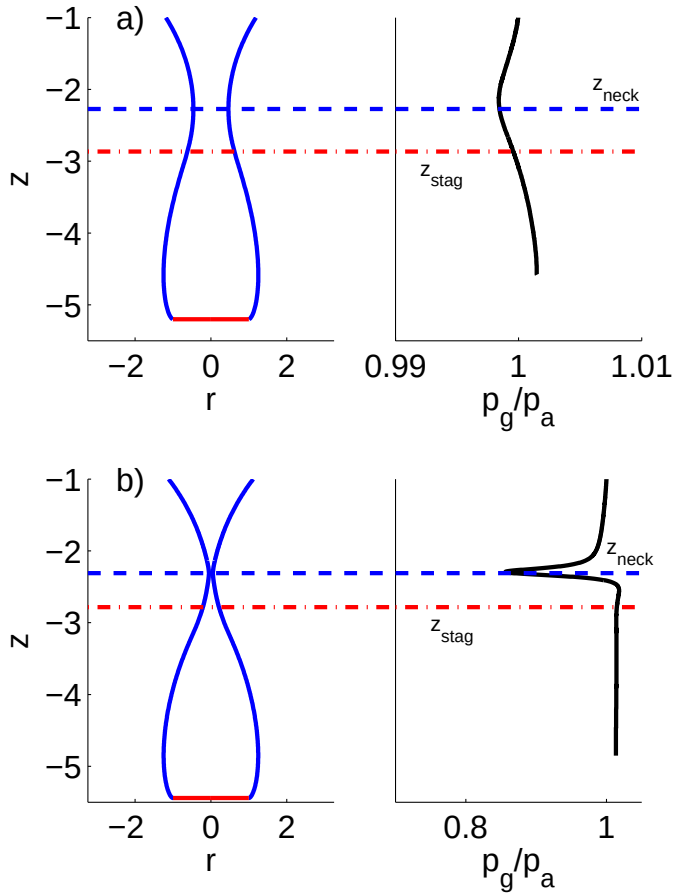


Figure 5.8: The pressure profile in the Euler zone at the same instants as in Fig. 5.5. The low pressure at the neck is caused by the high gas speeds in that region.

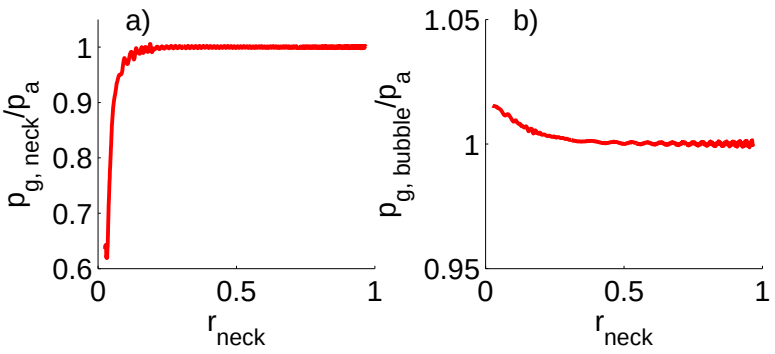


Figure 5.9: (a) The pressure at the neck diminishes over time to reach a minimum value of approx. 0.6 atmospheres. (b) In contrast, the pressure deep inside the bubble rises only slightly above atmospheric towards the end.

air is pushed out through the cavity neck. In this stage we couple two different methods: a Roe scheme to solve the one-dimensional Euler equations in the gas domain and a single-fluid boundary-integral method in the liquid domain. The two domains are connected via the pressure at the free surface.

The predominantly one-dimensional character of the air stream and the shape of the impact cavity make our system reminiscent to the common problem of air flow through a converging-diverging nozzle in aerodynamics. There is, however, an important and fundamental difference: since in our case the confining cavity is a *liquid*, the "nozzle" shape is rapidly evolving in time. We showed that due to this unique feature the air stream can attain supersonic velocities with the cavity pressure being no more than 2% larger than the surrounding atmosphere.

For low gas velocities we find very good agreement between our simulations and direct experimental measurements [18]. The shape of the cavity as well as a final upward motion of the cavity neck [18] give further strong evidence that our multiphase numerical method faithfully reflects reality.

## References

[1] A. M. Worthington, *A study of splashes* (Longmans, Green and Co., London) (1908).

[2] H. N. Oguz and A. Prosperetti, "Bubble entrainment by the impact of drops on liquid surfaces", J. Fluid Mech. **219**, 143–179 (1990).

[3] D. Morton, M. Rudman, and J. L. Liow, "An investigation of the flow regimes resulting from splashing drops", Phys. Fluids **12**, 747–763 (2000).

[4] C. Josserand and S. Zaleski, "Droplet splashing on a thin liquid film", Phys. Fluids **15**, 1650–1657 (2003).

[5] G. Leneweit, R. Koehler, K. G. Roesner, and G. Schäfer, "Regimes of drop morphology in oblique impact on deep fluids", J. Fluid Mech. **543**, 303–331 (2005).

[6] X. Zheng, J. L. A. Anderson, and V. Cristini, "Adaptive unstructured volume remeshing – II: Application to two- and three-dimensional level-set simulations of multiphase flow", J. Comput. Phys. **208**, 626–650 (2005).

[7] E. Coyajee and B. J. Boersma, "Numerical simulation of drop impact on liquid-liquid interface with a multiple marker front-capturing method", J. Comput. Phys. **228**, 4444–4467 (2009).

[8] M. Greenhow and S. Moyo, "Water entry and exit of horizontal circular cylinders", Phil. Trans. R. Soc. London A **355**, 551–563 (1997).

[9] S. Gaudet, "Numerical simulation of circular disks entering the free surface of a fluid", Phys. Fluids **10**, 2489–2499 (1998).

[10] D. Battistin and A. Iafrati, "Hydrodynamic loads during water entry of two-dimensional and axisymmetric bodies", J. Fluid Struct. **17**, 643–664 (2003).

[11] J. Li, M. Hesse, J. Ziegler, and A. W. Woods, "An arbitrary Lagrangian-Eulerian method for moving-boundary problems and its applications to jumping over water", J. Comput. Phys. **208**, 289–314 (2005).

[12] D. Vella and P. D. Metcalfe, "Surface tension dominated impact", Phys. Fluids **19**, 072108 (2007).

[13] P. Lin, "A fixed-grid model for simulations of a moving body in free surface flows", Comput. Fluids **36**, 549–561 (2007).

[14] S. Gekle, A. van der Bos, R. Bergmann, D. van der Meer, and D. Lohse, "Non-continuous froude number scaling for the closure depth of a cylindrical cavity", Phys. Rev. Lett. **100**, 084502 (2008),
*See Chapter 7 of this thesis.*

[15] S. Gekle, J. M. Gordillo, D. van der Meer, and D. Lohse, "High-speed jet formation after solid object impact", Phys. Rev. Lett. **102**, 034502 (2009),
*See Chapter 2 of this thesis.*

[16] R. Bergmann, D. van der Meer, S. Gekle, A. van der Bos, and D. Lohse, "Controlled impact of a disc on a water surface: Cavity dynamics", J. Fluid Mech. **633**, 381–409 (2009).

[17] M. Do-Quang and G. Amberg, "The splash of a solid sphere impacting on a liquid surface: Numerical simulation of the influence of wetting", Phys. Fluids **21**, 022102 (2009).

[18] S. Gekle, I. R. Peters, J. M. Gordillo, D. van der Meer, and D. Lohse, "Supersonic air flow due to solid-liquid impact", preprint (2009),
*See Chapter 4 of this thesis.*

[19] D. Bartolo, C. Josserand, and D. Bonn, "Singular jets and bubbles in drop impact", Phys. Rev. Lett. **96**, 124501 (2006).

[20] Q. Deng, A. V. Anilkumar, and T. G. Wang, "The role of viscosity and surface tension in bubble entrapment during drop impact onto a deep liquid pool", J. Fluid Mech. **578**, 119–138 (2007).

[21] S. Gekle and J. M. Gordillo, "Generation and breakup of worthington jets after bubble collapse", preprint (2009),
*See Chapter 3 of this thesis.*

[22] C. Laney, *Computational gasdynamics* (Cambridge University Press) (1998).

[23] P. L. Roe, "Approximate Riemann solvers, parameter vectors, and difference schemes", J. Comput. Phys. **43**, 357–372 (1981).

[24] C. Pozrikidis, *Introduction to theoretical and computational fluid dynamics* (Oxford University Press) (1997).

[25] J. R. Blake, B. B. Taib, and G. Doherty, "Transient cavities near boundaries: Part I. Rigid boundary", J. Fluid Mech. **170**, 479–497 (1986).

[26] H. N. Oguz and A. Prosperetti, "Dynamics of bubble growth and detachment from a needle", J. Fluid Mech. **257**, 111–145 (1993).

[27] J. Rodríguez-Rodríguez, J. M. Gordillo, and C. Martínez-Bazán, "Breakup time and morphology of drops and bubbles in a high-reynolds-number flow", J. Fluid Mech. **548**, 69–86 (2006).

[28] J. M. Gordillo, A. Sevilla, and C. Martínez-Bazán, "Bubbling in a co-flow at high reynolds numbers", Phys. Fluids **19**, 077102 (2007).

[29] H. W. Liepmann and A. Roshko, *Elements of gas dynamics* (Wiley) (1957).

# 6

# Approach to universality in axisymmetric bubble pinch-off *

*The pinch-off of an axisymmetric air bubble surrounded by an inviscid fluid is compared in four physical realizations: (i) cavity collapse in the wake of an impacting disc, (ii) gas bubbles injected through a small orifice, (iii) bubble rupture in a straining flow, and (iv) a bubble with an initially necked shape. Our boundary-integral simulations suggest that all systems eventually follow the universal behavior characterized by slowly varying exponents predicted in [Eggers et al., PRL **98**, 094502 (2007)]. However, the time scale for the onset of this final regime is found to vary by orders of magnitude depending on the system in question: while for the impacting disc it is well in the millisecond range, for the gas injection needle universal behavior sets in only a few microseconds before pinch-off. These findings reconcile the different views expressed in recent literature about the universal nature of bubble pinch-off.*

*Published as: Stephan Gekle, Jacco H. Snoeijer, Detlef Lohse, and Devaraj van der Meer, "Approach to universality in axisymmetric bubble pinch-off", Phys. Rev. E **80**, 036305 (2009).

## 6.1 Introduction

The precise nature of axisymmetric bubble collapse in a low-viscosity fluid has been a subject of controversy over the last years. Such a collapse may be initiated by a variety of different forces (e.g. surface tension, hydrostatic pressure, and external flows). In a later stage, however, it is only the requirement of mass conservation that forces the liquid to accelerate more and more as the shrinking bubble neck closes in on the axis of symmetry. This purely inertial nature of the final collapse motivated the first hypotheses about universality of the final collapse regime [1, 2]. A simple power-law was predicted with the neck radius scaling as the square root of the time remaining until the pinch-off singularity. Neither numerically nor experimentally could this behavior be confirmed. Instead, for different systems and initial conditions a variety of scaling exponents all slightly above 1/2 have been obtained [3–10] leading to doubts about the universal nature of bubble collapse.

Recently, the idea of universality has been revived by [11, 12] who suggested an intricate coupling between the radial and axial length scale. The authors of [12] explicitly predict the existence of a final universal regime which however is no longer a simple power-law, but characterized by a local exponent that slowly varies in time. The value of 1/2 is recovered in the asymptotic limit infinitesimally close to pinch-off. According to this theory the variety of observed exponents corresponds to different time averages of this local exponent. Note that this is different from the universality as observed for example in the pinch-off of a drop [13] where the behavior of the neck radius can be described by a scaling law whose universal exponent remains constant in time. With the exception of the rather idealized system used in [12], this universality has thus far never been directly observed in neither experiments nor simulations.

In the present work we aim to reconcile the different views about universality in axisymmetric bubble pinch-off expressed over the last years. The key aspect is that we examine in detail how and when different physical realizations of bubble pinch-off reach the universal regime. We present detailed numerical simulations which are able to follow the neck evolution over more than 12 decades in time even for complex realistic systems. With these we demonstrate that all systems that have recently been studied in the context of bubble pinch-off eventually follow the same universal behavior predicted by [12]. The time scale on which universality is reached, however, varies enormously: For an impacting disc [4, 14] universality can be observed during several milliseconds prior to pinch-off and thus on a time scale which is experimentally accessible. However, for gas bubbles injected through a small needle [1, 2, 5–10, 15–17] universality sets in only a few microseconds (or even less, depending on the precise initial conditions) before pinch-off. This may well be the

reason why universality has thus far never been observed even in very precise gas injection experiments and why non-inertial effects like surface tension have been claimed to play a dominant role in this geometry [9, 10]. By specifying the onset times of universality our work thus provides a solid basis to which onset times of non-universal disturbance effects such as viscosity, air flow, or non-axisymmetry can be compared in order to assess whether or not a given system would in reality exhibit such universal behavior.

Four different physical systems have been reported in the literature on bubble pinch-off, numerically and experimentally, and will be compared in this work:

(i) *Impacting disc*. The bubble is created by the impact of a circular disc on a liquid surface [4, 14] as shown in Fig. 6.1(i). Upon impact an axisymmetric air cavity forms and eventually pinches off halfway down the cavity under the influence of hydrostatic pressure. Immediately after pinch-off the ejection of a violent jet can be observed whose formation however is not caused by the singularity alone [18] as one might expect. Since surface tension is negligible [4, 14, 18] the only relevant control parameter is the Froude number $\mathrm{Fr} = V_0^2/gR_0$ with the impact velocity $V_0$, gravity $g$ and the disc radius $R_0$. In the data reported here the disc radius varies between 1 and 3cm and the impact velocity ranges from 1 to 20m/s.

(ii) *Gas injection through an orifice*. A small needle sticks through the bottom of a quiescent liquid pool [1, 2, 5–10, 15–17] as illustrated in Fig. 6.1(ii). A pressure reservoir connected to the needle slowly pushes a gas bubble out of the needle's orifice. The bubble then rises under the influence of buoyancy. When the air thread between the orifice and the main bubble becomes long enough, surface tension causes the thinning of the neck which eventually leads to the pinch-off of the bubble. We present data for three sample configurations A-C corresponding to Figs. 4, 10, and 6 of [2] and characterized by a Weber number $\mathrm{We}_{\mathrm{A,B,C}}$ =0.007, 36 and 173, respectively. (Here, $\mathrm{We} = \rho Q^2/(\pi^2 a^3 \sigma)$ with water density $\rho$, gas flow rate $Q$, needle radius $a$ and surface tension $\sigma$).

(iii) *Bubble in a straining flow*. The initially spherical bubble collapses due to a surrounding hyperbolic straining flow [3, 11, 19, 20], see Fig. 6.1(iii).

(iv) *Initially necked bubble*. Surface tension causes the pinch-off of a bubble starting off with an initially already pronounced neck [12] as illustrated in Fig. 6.1(iv).

## 6.2 Local scaling exponents

In all systems we consider the idealized invisicid, axisymmetric bubble pinch-off neglecting the influence of the inner gas dynamics [3, 8–10, 20–23], viscosity [6, 9, 10, 15], and non-axisymmetric perturbations [16, 17]. For our numerical investigations

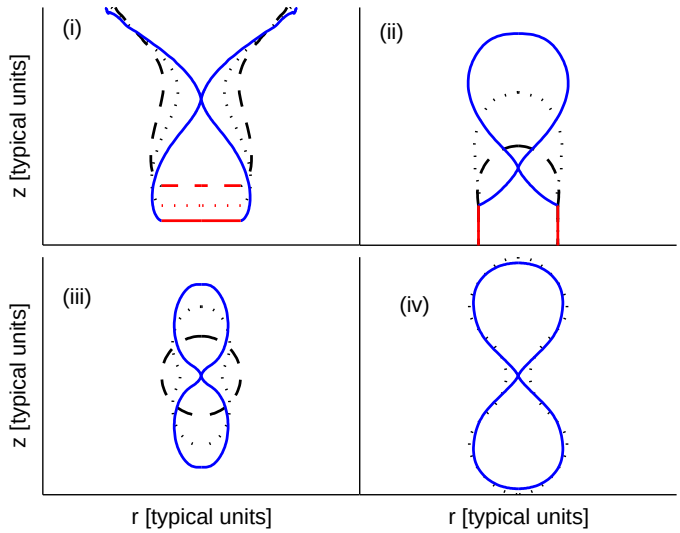


Figure 6.1: Illustration of the bubble collapse in the 4 different systems: impacting disc (i), gas injection through a needle orifice (ii), bubble in a straining flow (iii), and initially necked bubble (iv). Solid blue lines correspond to the free surface at pinch-off, while dashed and dotted black lines represent earlier bubble shapes. The disc and needle are depicted in red (light gray).

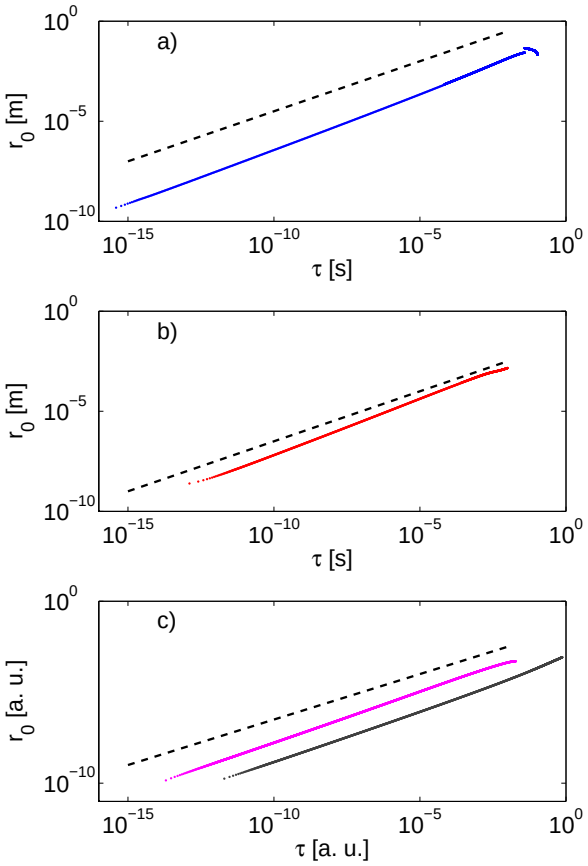


Figure 6.2: "Classical" plot of the neck radius versus the time to pinch-off. (a) for system (i) with Fr=5.1 ($R_0 = 2$ cm, $V_0 = 1$ m/s), (b) for system (ii) in setup A, and (c) for systems (iii) and (iv) shown in dark gray (lower line) and magenta (upper line), respectively. The dashed line represents a slope of 1/2.

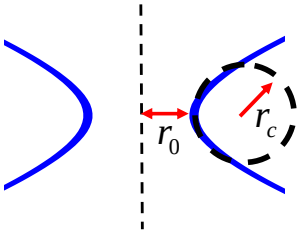


Figure 6.3: Illustration of the cavity surface, the minimal neck radius $r_0$ and the local radius of curvature $r_c$.

we employ an axisymmetric boundary-integral (BI) code similar to the one described in [14] which has shown very good agreement with experiments of system (i) for various impact geometries [4, 14, 24]. The validity of our implementation for the other systems is verified by comparison with the bubble shapes from various earlier works [2, 12, 19]. Some details about the simulation parameters are given in the appendix.

In a first approach to an analytical description of bubble collapse, the bubble shape can be approximated as an infinitely long cylinder (neglecting axial velocities) which yields a two-dimensional version of the well-known Rayleigh equation [2–4, 11, 15] for the neck radius $r_0$

$$\frac{d\left(r_0\dot{r}_0\right)}{dt}\ln\frac{r_0}{R_\infty}+\frac{1}{2}\dot{r}_0^2=\frac{F}{\rho}. \tag{6.1}$$

Here, $\rho$ is the liquid density, $F$ represents the pressure force initiating the collapse, and dots denote the derivative with respect to time $t$. $R_\infty$ is a cut-off radius required to saturate the pressure at large distances. Assuming constant $R_\infty$ leads to the neck radius $r_0$ shrinking as a power-law (possibly with logarithmic corrections [3, 4, 11]) with exponent 1/2 as a function of the time to pinch-off $\tau = t_c - t$, where $t_c$ is the closure time. At first sight, this expectation seems to be very well confirmed for all four systems by the lines in Fig 6.2 which to the naked eye appear perfectly straight over more than 12 decades. The slope which corresponds to the scaling exponent is slightly larger than 1/2, in agreement with previous experiments and simulations which have reported exponents between 0.5 and 0.6 [3–6, 8–11, 15].

A more detailed look at the local exponent, defined as the slope in Fig. 6.2, $\alpha(\tau) = \partial \ln r_0 / \partial \ln \tau$, reveals that the behavior of the neck radius cannot be described by a simple power-law. The local exponent $\alpha$ varies during the approach to pinch-off [12]. In fact, the relevant equation for the time-dependence of $\alpha$ in [12] can be derived directly from Eq. (6.1) by letting $R_\infty = 2\sqrt{r_0 r_c}$. Here $r_c$ is the local axial radius

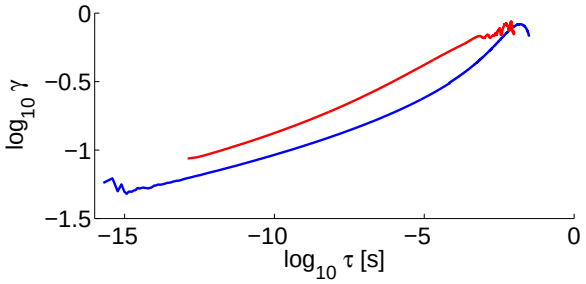


Figure 6.4: The aspect ratio $\gamma$ plotted as a function of the time to pinch-off $\tau$ for system (i) with Fr=5.1 (blue lower line) as well as system (ii) in setup A (red upper line). This shows that one can use $\gamma$ instead of $\tau$ as a measure for the approach to pinch-off.

of curvature (see Fig. 6.3). The combination $\sqrt{r_0 r_c}$ is the scale by which the axial coordinate has to be rescaled in order to collapse neck profiles at different times when rescaling radial coordinates by $r_0$ [4, 6] [†]. This leads to the aspect ratio of the cavity naturally being defined as $\gamma = r_0/\sqrt{r_0 r_c}$. With the above substitutions and working in the limit of vanishing $F$, i. e., in the regime where the influence of the driving force has become subdominant, we obtain from Eq. (6.1):

$$\left(-\frac{d\alpha}{d\ln\tau} + \alpha - 2\alpha^2\right)\ln\left(\frac{4}{\gamma^2}\right) = -\alpha^2 \tag{6.2}$$

which is exactly identical to Eq. (4) in [12] (being $\Gamma_1 = 8$ [25] and $a_0'' = 2\gamma^2$ in the original notation). Equation (6.2) with the $d\alpha/d\ln\tau$ term neglected due to the slow variation of $\alpha$ [‡] represents the universal regime where the only driving is provided by inertia and all external forces have become negligible. We will now proceed to compare the approach of the different systems (i)-(iv) to this universal curve. Equation (6.2) with the above approximation suggests to represent $\alpha$ not as a function of time to pinch-off $\tau$, but instead as a function of the aspect ratio $\gamma$. Since there is a one-to-one correspondence between $\tau$ and $\gamma$ shown in Fig. 6.4 we can use the aspect ratio $\gamma$ as a universal "clock" replacing the time to pinch-off $\tau$ [25]. Note that $\gamma \to 0$ as $\tau \to 0$ meaning that the cavity becomes more and more slender [6, 11]. Another

[†] A Taylor expansion of the cavity profile around the neck yields: $r(z) = r_0 + \partial^2 r/\partial z^2 \cdot \Delta z^2/2 = r_0 + 1/r_c \Delta z^2/2$. To collapse these profiles one can rescale the radial length scale with $r' = r/r_0$ and the axial length scale with $z' = z/\sqrt{r_0 r_c}$ to obtain the time-independent shape $r' = 1 + \Delta z'^2/2$.

[‡] In the BI data we verified that $|d\alpha/d\ln\tau| \ll |\alpha - 2\alpha^2|$.

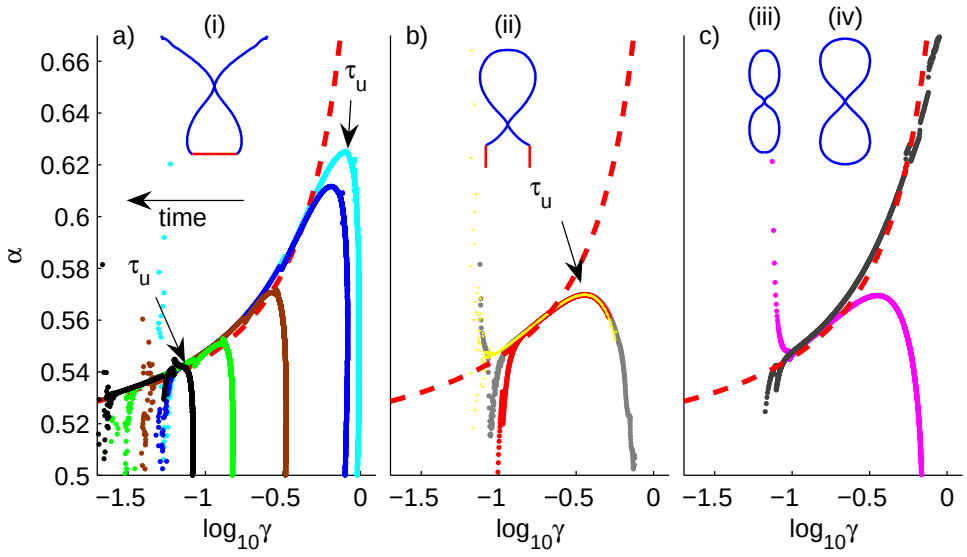


Figure 6.5: (a) The local exponent $\alpha$ as a function of the aspect ratio $\gamma$ for system (i) with Fr=3.4 (cyan, rightmost curve), Fr=5.1 (blue), Fr=46 (brown), Fr=500 (green), and Fr=4000 (black, leftmost curve). After an initial transient all curves follow the same universal regime. The dashed line is Eq. (6.2). The local maxima correspond roughly to the start of the universal regime. (b) The local exponent for system (ii) in the three configurations: A (red, dark gray), B (gray) and C (yellow, very light gray). All curves A-C lie practically on top of each other. (c) The local exponent for system (iii) in dark gray (upper curve) and system (iv) in magenta (light gray, lower curve) follows the same universal behavior close to pinch-off. Small jumps in the data are due to the crossover between different node positioning algorithms employed in the initial and the final stages of the simulation (see appendix) while the deviation of the numerical data away from the universal curve at the very end stems from the uncertainty in determining the exact time of closure.

motivation to use $\gamma$ instead of $\tau$ is that Eq. (6.2) is invariant under a rescaling of time $\tau \to \beta\tau$ reflecting an arbitrariness of the time coordinate in this problem. The aspect ratio $\gamma$ does not possess this arbitrariness.

## 6.3 Approach to universality

One of the key points to address is if and how this behavior can be observed experimentally. Besides the obvious difficulty of obtaining a sufficient number of decades to observe the slow variation of the local exponent, the crucial question is: at what time (before pinch-off) does the system exhibit universal behavior? This is crucial because, firstly, the duration of the universal regime needs to be within the time resolution of the experimental equipment. And secondly, the onset of universality needs to happen before other effects such as air flow, viscosity, non-axisymmetric instabilities, etc. unavoidably destroy the purely inertial regime. We will now provide those time scales for the various systems based on numerical BI simulations which do not have these limitations.

We start by considering the impacting disc system (i) in Fig. 6.5 (a). It is evident that the data for all values of the control parameter follow – after some initial transient – the same universal curve in very good agreement with Eq. (6.2). Our data thus confirms the existence of a universal regime as predicted in [12]. Since from Fig. 6.5 the closure time cannot be determined in a straightforward manner, the closure time has been estimated by fitting straight lines in plots like Fig. 6.2. As this procedure is not exact due to the time-dependence of the local scaling exponent, it leads to a deviation of the numerical data from the universal curve in Fig. 6.5 towards the very end which however is merely an artifact of the uncertainty in the exact closure time.

Figure 6.5 (a) further gives us a good measure at what aspect ratio the universal regime is attained: approximately after passing their respective local maxima all curves follow the same behavior. The aspect ratio of this maximum can then easily be related to the physical time before pinch-off $\tau_u$ using Fig. 6.4. We find $\tau_u \approx 6$ms and $\tau_u \approx 1$ms for Fr=3.4 and Fr=4000, respectively. That the high Froude case reaches universality later can be intuitively understood: at high Froude the cavity closes deeper and therefore the hydrostatic driving pressure is larger and its effects on the neck dynamics can be felt longer. It is remarkable nevertheless that the duration of the universal regime changes only by a factor of less than 10 while the corresponding control parameter varies over three orders of magnitude. At the same time both values are easily within experimentally accessible time scales.

We now compare this to system (ii), the bubble injection through a small needle in Fig. 6.5 (b). While also this system clearly exhibits universal behavior, the approach

to the universal regime is much less abrupt than in system (i). Due to this more gradual approach, it is difficult to specify precisely the time when universality is reached for the gas injection needle. We thus choose to keep our previous definition of $\tau_u$ being the time corresponding to the local maximum in Fig. 6.5 (b). This gives a good upper bound for the time when universality sets in. Surprisingly, we find even these times to be of the order of $5\mu$s in case A, 60ns in case C and as low as 10ns in case B, respectively [§]. Thus, the duration of the universal regime in the needle setup is dramatically (by at least three orders of magnitude) shorter than for the impacting disc. This may well explain why, besides possible disturbing effects (viscosity, gas flow, non-axisymmetry) an observation of the universal regime has thus far never been reported in the literature on this widely used system.

Figure 6.5 (c) confirms that also the systems (iii) and (iv) follow the universal regime. System (iii) does so even over the entire plotted range. Both are somewhat idealized systems for which we are not aware of any experimental investigations regarding the approach to pinch-off. Without a relevant length and time scale it is impossible to specify the physical time to universality in these cases.

The different behaviors of the individual systems can intuitively be understood as follows. System (iii) contains no external driving force other than liquid inertia which makes it the ideal system to compare with Eq. (6.2). Indeed, this entirely inertial system follows the universal regime over the widest range in aspect ratios of all systems studied. Similarly, due to the relatively large dimensions of the collapsing cavity in system (i) a correspondingly large amount of inertia is introduced into the system which consequently follows the universal regime also for a rather long time. On the other hand, the two systems where pinch-off is initiated by surface tension (ii) and (iv) contain little inertia and thus approach the universal regime only relatively late and in a similar fashion.

To make the above arguments more quantitative we realize that the universal regime sets in when the inertial driving of the collapse becomes dominant over the external driving force. This can be expressed by a local balance between inertia and the respective driving force. For system (i) the driving force is hydrostatic pressure and the relevant parameter thus the local Froude number $\mathrm{Fr}_{\mathrm{local}} = \dot{r}_0^2/(gz_c)$ with gravity $g$ and $z_c$ the depth below the surface where the cavity eventually closes. For system (ii) the local Weber number $\mathrm{We}_{\mathrm{local}} = \rho \dot{r}_0^2 r_0/\sigma$ (with density $\rho$ and surface tension $\sigma$ of water) gives the balance between inertia and surface tension as the relevant driving

[§]The long duration of the universal regime for the quasi-static case A can be understood as follows: in case A the maximum diameter of the bubble is only slightly larger than the orifice in contrast to the other two situations where the bubble is much larger than the needle exit. Accordingly, the neck in case A possesses already initially a rather symmetrical shape with its upper half being very similar to the lower one which is prerequisite for the universal solution to be applicable.

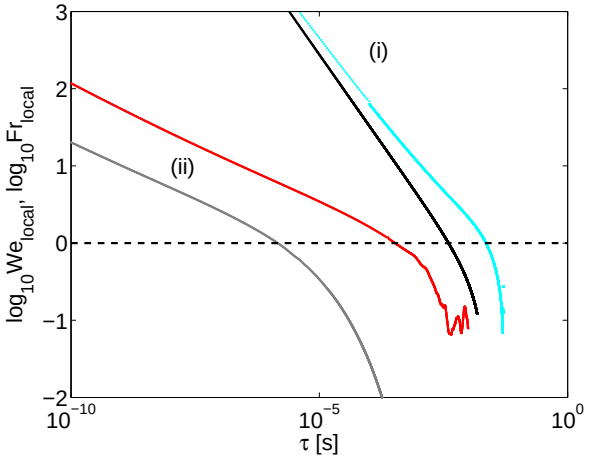


Figure 6.6: The local Froude number for system (i) and an impact Froude number Fr=3.4 (cyan, rightmost curve) and Fr=4000 (black) and the local Weber number for system (ii) with configuration A (red/dark gray) and B (gray, leftmost curve). The onset of the universal regime can be located roughly after the respective non-dimensional quantities have become larger than order unity (horizontal dashed line).

force. The duration of the universal regime can then be estimated as the time before pinch-off when these local quantities become of order unity. Figure 6.6 shows the local Froude and Weber numbers as a function of time to pinch-off $\tau$ for a number of representative cases of system (i) and (ii), respectively. One can clearly appreciate that $We_{local}$ for the needle system becomes unity later than $Fr_{local}$ for the impacting disc. This explains the large discrepancy in $\tau_u$ for the two systems.

At the same time the distance between the two disc impacts with Fr=3.4 and Fr=4000 is smaller than that between the two needle setups A and B. Accordingly, the duration of the universal regime varies only between $\sim$1ms and $\sim$6ms for the disc while in the needle setup it depends much stronger on initial conditions varying from micro- down to several nanoseconds as seen above.

## 6.4 Relation to earlier work on disc impact

We will now explain the Froude-dependence of the experimentally and numerically observed exponents in [4] for the impacting disc. Based on Fig. 6.5 (a) these exponents can be viewed as a time-average of the local exponent. Due to the limited

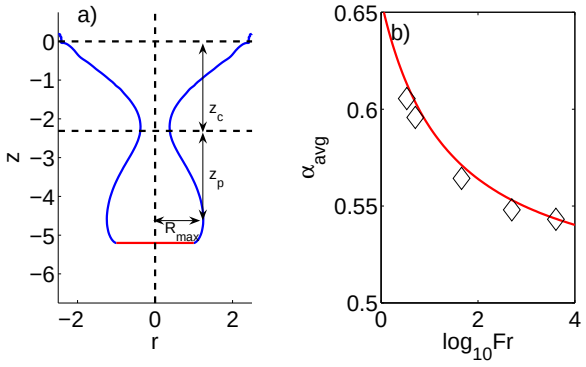


Figure 6.7: (a) Illustration of the characteristic aspect ratio of the cavity. (b) The averaged exponent measured in [4] (black diamonds) is reproduced very well by our model with the constant $K = 0.46$ (red line).

resolution and the onset of other effects (e.g. air flow) only the right part of these plots is accessible in experiments and the time-average will be heavily weighted towards the beginning of the universal regime, i. e., to a region just around and left of the maximum in Fig. 6.5 (a). We can thus assume the experimentally observed effective exponent to be roughly equal to the maximum value of the local exponent which is where universal behavior sets in. As can be seen in Fig. 6.5 (a) the approach to the maximum is almost vertical which implies that $\gamma$ remains constant during a certain time before pinch. This allows us to approximate the aspect ratio where universality is reached by the macroscopic aspect ratio $\gamma_i$ of the cavity at the start of the universal regime. Using Eq. (6.2) we can predict this value once the characteristic initial aspect ratio $\gamma_i$ for each cavity is known.

This quantity $\gamma_i$ however is not straightforward to determine since the configuration before impact is simply a flat surface and the only value available to characterize the initial conditions is the Froude number. We are nevertheless able to provide an estimate for $\gamma_i$ as illustrated in Fig. 6.7 (a) which shows the cavity shape at the beginning of the universal regime. The horizontal size of this cavity is its maximum radial expansion $R_{\max}$. The characteristic vertical length scale can be assumed to be proportional to the depth of eventual closure $z_c$. For both quantities the dependence on initial conditions can be written in terms of scaling laws with the impact Froude number. The horizontal length scales approximately as $R_{\max} \sim \mathrm{Fr}^{1/4}$ [14] while the vertical length behaves as $z_c \sim \mathrm{Fr}^{1/2}$ [14, 26].

With these two quantities in hand we can estimate the characteristic initial aspect

ratio as

$$\gamma_i = C\frac{R_{\max}}{z_c} \approx 2K^{-1/4}\mathrm{Fr}^{-1/4} \tag{6.3}$$

with $C$ and $K$ constants of order unity. Inserting this $\gamma_i$ into Eq. (6.2) and solving for $\alpha(\mathrm{Fr})$, again neglecting $d\alpha/d\ln\tau$ gives:

$$\alpha = \frac{\ln(K\mathrm{Fr})}{2\ln(K\mathrm{Fr}) - 2}. \tag{6.4}$$

We can thus predict the experimentally observable averaged exponent which is found in very good agreement with [4] as demonstrated by Fig. 6.7 (b). Thus, the way how the experimentally and numerically observed exponents depend on the global impact parameters [4] constitutes an impressive manifestation of universal behavior in this system.

## 6.5 Conclusion

In conclusion, we have demonstrated that the universal theory of [12, 25] faithfully predicts the approach of the neck radius for inviscid, axisymmetric bubble pinch-off in four different systems widely studied in the literature over the past years. Remarkably, however, the duration of the final regime is shown to be strongly dependent on the type of system and the various control parameters employed. While it lies easily within experimentally accessible time scales (∼ms) for an impacting circular disc, it can be as low as a few nanoseconds for gas bubbles injected through a small orifice into a quiescent liquid pool. We were able to trace this difference back to the relative importance of the respective driving forces. Our findings reconcile the prediction of universality in bubble pinch-off [11, 12] with an apparent dependence on initial conditions [4], an apparently constant scaling exponent [5, 6, 8], and with the observation that non-inertial forces can be dominant in many experimental settings [9, 10, 20].

## Appendix: Simulation details

Simulations are conducted using an axisymmetric boundary-integral code similar to [14]. In order to obtain reliable data over more than 12 time decades in complex physical situations such as the impacting disc or the injection needle it is necessary to split each simulation in an initial and a final part. In the former the node density along the surface is adapted proportional to the local curvature. Smoothing is required to ensure stability of the numerical scheme and is achieved by periodic regridding [14]. In the second part close to pinch-off the node density around the neck is taken to

be inversely proportional to the neck radius to achieve a high enough resolution and the regridding procedure is turned off to avoid numerical noise. At the crossover small jumps in the simulation data may result when plotting derived quantities such as $\alpha = d\ln r_0/d\ln\tau$. We checked carefully that our results are independent of the location of this jump.

The control parameters for the four systems are as follows:
(i) Initial conditions for the disc impact are characterized by the disc radius $R_0$ and the impact velocity $V_0$ which can be combined with gravity $g$ into the Froude number $\mathrm{Fr} = V_0^2/(gR_0)$ as the only relevant control (surface tension is included but irrelevant [14, 18]). Length and time scales are non-dimensionalized by the disc radius $R_0$ and the typical time $T_0 = R_0/V_0$. Five different cases are reported in this chapter: $R_0 = 3$cm and $V_0 = 1$m/s (Fr=3.4); $R_0 = 2$cm and $V_0 = 1$m/s (Fr=5.1); $R_0 = 2$cm and $V_0 = 3$m/s (Fr=46); $R_0 = 1$cm and $V_0 = 7$m/s (Fr=500); $R_0 = 1$cm and $V_0 = 20$m/s (Fr=4000). The pressure inside the cavity is atmospheric throughout.
(ii) For the gas injection needle each realization is characterized by the needle radius $a$, the gas flow rate $Q$, the overpressure in the chamber $p_c - p_\infty$, and the effective needle length $l$ [2]. Three different cases A-C are presented: $a_{\mathrm{A,B,C}}$=2mm, 0.1mm, 0.27mm; $Q_{\mathrm{A,B,C}}$=198mm$^3$/s, 162mm$^3$/s, 1564mm$^3$/s; $p_{c;\mathrm{A,B,C}} - p_\infty$=73.73Pa, 1494.8Pa, 546.410Pa; and $l_{\mathrm{A,B,C}}$=128m, 20mm, 40mm. If the Weber number defined as $\mathrm{We} = \rho Q^2/(\pi^2 a^3 \sigma)$ with the water density $\rho$ and surface tension $\sigma$ is small the bubble growth proceeds in a quasi-static regime. We find for our cases $\mathrm{We}_{\mathrm{A,B,C}}$=0.007, 36, and 173, respectively, meaning that case A represents a quasi-static case while the other two go beyond the quasi-static regime. Units are non-dimensionalized by the needle radius $a$ and the typical time $T_0 = a/V_0$ with $V_0 = Q/(\pi a^2)$. The air inside the bubble is assumed to be incompressible during the entire process and the bubble pressure is modeled as described in [2].
(iii) The bubble in a straining flow is characterized by the non-dimensional Euler number: $\mathrm{Eu} = p_0/(\rho V^2)$ (with $V$ a typical velocity, $\rho$ the density and $p_0$ the initial absolute pressure inside the bubble). Here we choose Eu=1000, that is an almost incompressible bubble. Other values have been tried and show qualitatively similar results. The bubble is filled with an ideal gas obeying an adiabatic relation and surface tension is not included in the simulations presented in the main text. It is worth noting though, that the inclusion of surface tension leads to the curve in Fig. 2 (e) bending down, assuming a shape more similar to the surface-tension driven scenario of system (iv).
(iv) For the initially necked bubble only the Weber number is of relevance which we choose to equal unity. Due to the short duration of the collapse in this system the gas phase inside the bubble can safely be neglected. Different shapes have been tried and

yield qualitatively similar results.

## References

[1] M. S. Longuet-Higgins, B. R. Kerman, and K. Lunde, "The release of air bubbles from an underwater nozzle", J. Fluid Mech. **230**, 365–390 (1991).

[2] H. N. Oguz and A. Prosperetti, "Dynamics of bubble growth and detachment from a needle", J. Fluid Mech. **257**, 111–145 (1993).

[3] J. M. Gordillo, A. Sevilla, J. Rodríguez-Rodríguez, and C. Martínez-Bazán, "Axisymmetric bubble pinch-off at high reynolds numbers", Phys. Rev. Lett. **95**, 194501 (2005).

[4] R. Bergmann, D. van der Meer, M. Stijnman, M. Sandtke, A. Prosperetti, and D. Lohse, "Giant bubble pinch-off", Phys. Rev. Lett. **96**, 154505 (2006).

[5] N. C. Keim, P. Møller, W. W. Zhang, and S. R. Nagel, "Breakup of air bubbles in water: breakdown of cylindrical symmetry", Phys. Rev. Lett. **97**, 144503 (2006).

[6] S. T. Thoroddsen, T. G. Etoh, and K. Takehara, "Experiments on bubble pinch-off", Phys. Fluids **19**, 042101 (2007).

[7] J. M. Gordillo, A. Sevilla, and C. Martínez-Bazán, "Bubbling in a co-flow at high reynolds numbers", Phys. Fluids **19**, 077102 (2007).

[8] J. C. Burton and P. Taborek, "Bifurcation from bubble to droplet in inviscid pinch-off", Phys. Rev. Lett. **101**, 214502 (2008).

[9] J. M. Gordillo, "Axisymmetric bubble collapse in a quiescent liquid pool. I. Theory and numerical simulations", Phys. Fluids **20**, 112103 (2008).

[10] R. Bolaños-Jiménez, A. Sevilla, C. Martinez-Bazán, and J. M. Gordillo, "Axisymmetric bubble collapse in a quiescent liquid pool. II. Experimental study", Phys. Fluids **20**, 112104 (2008).

[11] J. M. Gordillo and M. Pérez-Saborid, "Axisymmetric breakup of bubbles at high reynolds numbers", J. Fluid Mech. **562**, 303–312 (2006).

[12] J. Eggers, M. A. Fontelos, D. Leppinen, and J. H. Snoeijer, "Theory of the collapsing axisymmetric cavity", Phys. Rev. Lett. **98**, 094502 (2007).

[13] J. Eggers, "Nonlinear dynamics and breakup of free-surface flows", Rev. Mod. Phys. **69**, 865 (1997).

[14] R. Bergmann, D. van der Meer, S. Gekle, A. van der Bos, and D. Lohse, "Controlled impact of a disc on a water surface: Cavity dynamics", J. Fluid Mech. **633**, 381–409 (2009).

[15] J. C. Burton, R. Waldrep, and P. Taborek, "Scaling and instabilities in bubble pinch-off", Phys. Rev. Lett. **94**, 184502 (2005).

[16] L. E. Schmidt, N. C. Keim, W. W. Zhang, and S. R. Nagel, "Memory-encoding vibrations in a disconnecting air bubble", Nature physics **5**, 343–346 (2009).

[17] K. S. Turitsyn, L. Lai, and W. W. Zhang, "Asymmetric bubble disconnection: persistent vibration evolves into smooth contact", arXiv:0902.0393v1 [physics.flu-dyn] (2009).

[18] S. Gekle, J. M. Gordillo, D. van der Meer, and D. Lohse, "High-speed jet formation after solid object impact", Phys. Rev. Lett. **102**, 034502 (2009),
*See Chapter 2 of this thesis.*

[19] J. Rodríguez-Rodríguez, J. M. Gordillo, and C. Martínez-Bazán, "Breakup time and morphology of drops and bubbles in a high-reynolds-number flow", J. Fluid Mech. **548**, 69–86 (2006).

[20] J. M. Gordillo and M. A. Fontelos, "Satellites in inviscid breakup of bubbles", Phys. Rev. Lett. **98**, 144503 (2007).

[21] D. Leppinen and J. Lister, "Capillary pinch-off in inviscid fluids", Phys. Fluids **15**, 568–578 (2003).

[22] M. Nitsche and P. H. Steen, "Numerical simulations of inviscid capillary pinch-off", J. Comput. Phys. **200**, 299–324 (2004).

[23] R. Bergmann, A. Andersen, D. van der Meer, and T. Bohr, "Bubble pinch-off in a rotating flow", Phys. Rev. Lett. **102**, 204501 (2009).

[24] S. Gekle, A. van der Bos, R. Bergmann, D. van der Meer, and D. Lohse, "Noncontinuous froude number scaling for the closure depth of a cylindrical cavity", Phys. Rev. Lett. **100**, 084502 (2008),
*See Chapter 7 of this thesis.*

[25] M. A. Fontelos, J. H. Snoeijer, and J. Eggers, "The spatial structure of bubble pinch-off", preprint (2009).

[26] V. Duclaux, F. Caillé, C. Duez, C. Ybert, L. Bocquet, and C. Clanet, "Dynamics of transient cavities", J. Fluid Mech. **591**, 1–19 (2007).

# 7

# Non-continuous Froude number scaling for the closure depth of a cylindrical cavity *

*A long, smooth cylinder is dragged through a water surface to create a cavity with an initially cylindrical shape. This surface void then collapses due to the hydrostatic pressure, leading to a rapid and axisymmetric pinch-off in a single point. Surprisingly, the depth at which this pinch-off takes place does not follow the expected Froude$^{1/3}$ power-law. Instead, it displays two distinct scaling regimes separated by discrete jumps, both in experiment and in numerical simulations (employing a boundary integral code). We quantitatively explain the above behavior as a capillary waves effect. These waves are created when the top of the cylinder passes the water surface.*

## 7.1 Introduction

Many phenomena in fluid dynamics are known to be self-similar [1] and universal, allowing physicists to describe their final outcome without precise knowledge of the initial conditions. Prime examples for such universality are the break-up of an elongated fluid filament inside another viscous fluid [2] and the pinch-off of a liquid

*Published as: Stephan Gekle, Arjan van der Bos, Raymond Bergmann, Devaraj van der Meer, and Detlef Lohse, "Non-continuous Froude number scaling for the closure depth of a cylindrical cavity", Phys. Rev. Lett. **100**, 084502 (2008).

droplet in air [3–5]. For the inverse problem [6–10], i.e., when an air-bubble pinches off inside a liquid, the dynamics retains a memory of its creation until the very end, indicating that at least no simple universal behavior exists. As an example for such a break-up, we examine the air-filled cavity created when a solid object is rapidly submerged through a water surface. The walls of the cavity subsequently collapse due to hydrostatic pressure from the liquid bulk. When the colliding walls meet, a violent jet shoots up into the air. Regardless of the behavior of the pinch-off [7], the location at which it takes place has been reported (experimentally and theoretically) to scale in a continuous fashion with the object velocity for such different systems as spheres on fluidized sand [11], solid disks [12], spheres and cylinders [13] on water and even water columns on water [14]. Our experimental and numerical evidence shows the lower limit where this scaling is broken through the interference of a second phenomenon unrelated to hydrostatic pressure. Surface waves created as the object passes the water surface significantly alter the pinch-off location in a non-continuous manner. Similar effects for the breakdown of a universal behavior due to waves interaction have been observed in, e.g., magnetohydrodynamics [15] and turbulence [16].

## 7.2 Experimental results

In our experiment we drag a cylinder with radius $R_0 = 20$ mm and length $l = 147$ mm through the surface of a large water tank using a linear motor connected to the cylinder bottom by a rod. We prescribe a constant cylinder velocity $V$ between 0.5 and 2.5 m/s. With the kinematic viscosity $\nu$ the global Reynolds number $\mathrm{Re} = R_0 V/\nu$ is of the order of $10^4$, while the local Reynolds number $\mathrm{Re} = R\dot{R}/\nu$ defined with the cavity radius $R$ for the point of minimum radius lies between $10^2$ and $10^5$ demonstrating that inertia dominates viscous effects. Further, with the surface tension coefficient $\sigma$, $\rho g R_0 \gg \sigma/R_0$, i.e. gravity dominates over surface tension. The relevant dimensionless parameter is thus the Froude number $\mathrm{Fr} = V^2/(R_0 g)$ with $g = 9.81$ m/s$^2$, which in our experiment ranges between 1.2 and 32.

The shape of the axisymmetric cavity is imaged with a high speed camera at up to 10,000 frames/sec, with the vertical coordinate $z$ pointing upwards along the cylinder axis and $r$ being the radial coordinate. Figure 7.1 shows a typical sequence of the cavity dynamics. We choose the starting position of the lower edge of the cylinder slightly below the water surface to suppress the splash. From there it is pulled downwards with high acceleration such that it has reached its prescribed speed before the top passes the water surface at $t = 0$. The submerging cylinder creates an air-filled cavity with an initially cylindrical shape whose side walls immediately

start to collapse (a). Magnification of the cavity walls as in (b) shows that they are not smooth surfaces, but exhibit pronounced ripples. Note that these ripples are of different origin than those observed after pinch-off [17].

From the high-speed video images we extract the closure depth of the cavity $z_c$ for cylinder velocities up to 2.5 m/s. Plotting the closure depth over the Froude number as in Fig. 7.2, we find two asymptotic regimes. The regime for low Froude numbers obeys a scaling behavior $z_c \sim \mathrm{Fr}^{\alpha}$ with an exponent $\alpha = \alpha_1 \approx 0.1$. This is in contrast to earlier experiments [13] which showed a single continuous scaling behavior with $\alpha \approx \frac{1}{3}$, for which a theoretical explanation in terms of inertia and gravity could be given [11, 13, 14]. At the end of the low Froude regime the data abruptly departs to an intermediate regime without any experimentally clearly discernable structure. After a pronounced jump we find a third regime, which due to experimental limitations can be observed only between Fr=22.4 and 35.5. While this is too short to ascribe a definite power-law behavior, we can nevertheless conclude that this last regime – in contrast to the preceding two regimes – is not disagreeing with the theoretically predicted value of a scaling exponent of 1/3.

## 7.3 Numerical results

To understand the underlying mechanism leading to this discontinuous behavior, we conducted boundary integral simulations. Our numerical results match very well with the high-speed videos without the use of any adjustable parameter, see Fig. 7.1. The agreement of the wave pattern in Fig. 7.1 (b) can even further be improved when at the expense of introducing a free parameter we allow for a deviation from the precise ninety degrees angle between the cylinder wall and the free surface accounting for the free surface being dragged down and resulting in a slightly curved profile close to the cylinder wall.

The numerical simulations allow us to study the ripples in Fig. 7.1 (b) in great detail. As the cylinder top passes the water surface, the rectangular corner between the cylinder wall and the water surface is no longer held in place by the solid boundary of the cylinder. The newly created free surface thus possesses a corner with very high (initially infinite) curvature. Surface tension immediately tries to flatten this surface by pulling the corner diagonally inwards into the fluid bulk. This results in a shock similar to throwing a stone onto a lake, which consequently leads to the formation of capillary waves travelling out- and downward on the free surface. The downward waves can be observed in Fig. 7.1 (b). The shock creates a wave packet containing waves of different frequencies. Each of these waves spreads with a velocity $c = \omega/k$ given by the dispersion relation $\omega^2 = (\sigma/\rho)k^3$, where we assume plane capillary

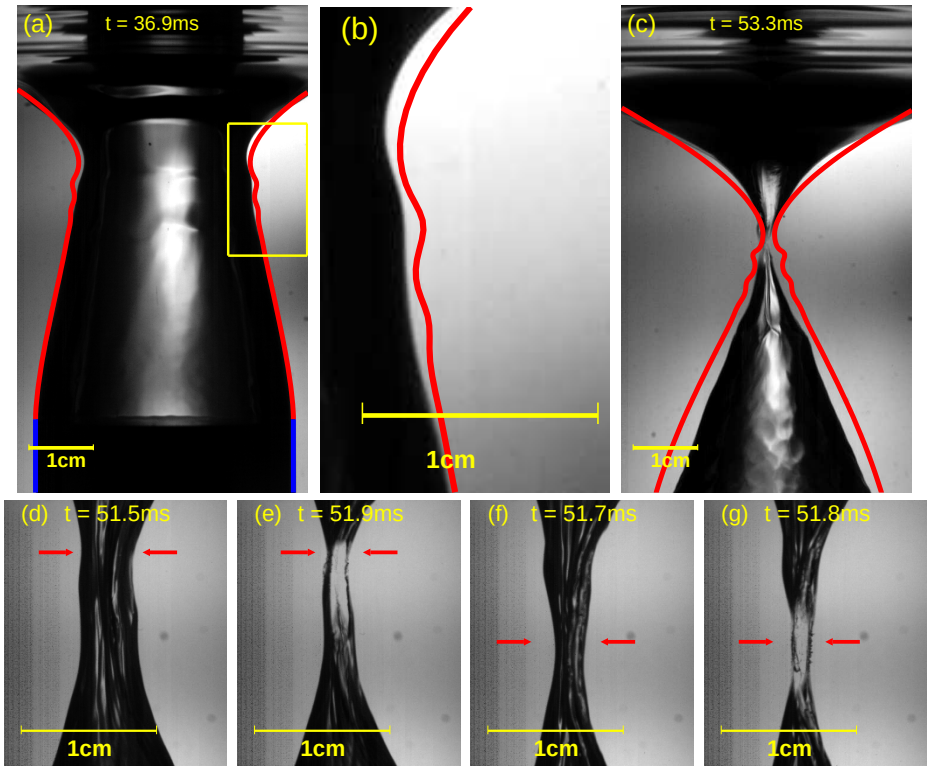


Figure 7.1: (a) - (c) Snapshots of the cavity for Fr=11.5. The area designated by the yellow rectangle in (a) is magnified in (b) illustrating the rippled surface of the cavity walls. Red lines show the numerical simulation. In (a) and (b) video frames are connected to simulation time by matching the cylinder position, for (c) it was more convenient to match the cavity closure times instead. (d) - (g) The transition from one closing ripple to the other. At Fr=18.8, (d) and (e), the upper of the two marked ripples closes. At Fr=20.6, (f) and (g), it is the lower of the two ripples which pinches.

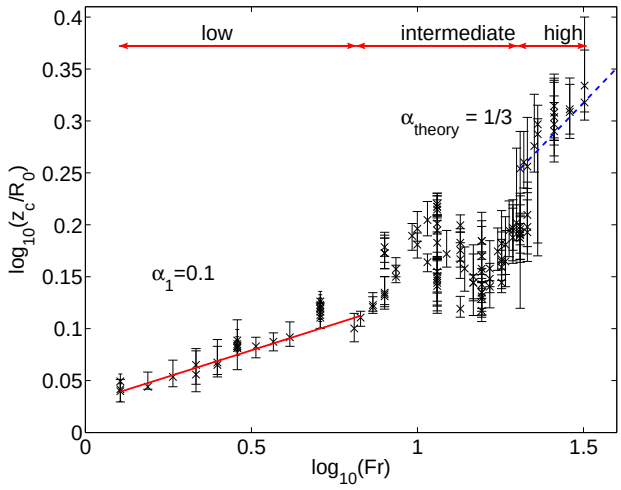


Figure 7.2: The experimental closure depth as a function of the Froude number. The asymptotic regime for low Froude numbers scales with $\alpha_1 \approx 0.1$ (red solid line). Only in the limit of high Froude numbers does the data not contradict an exponent of $\frac{1}{3}$ (blue dashed line). For the intermediate regime the experiments show no systematic behavior.

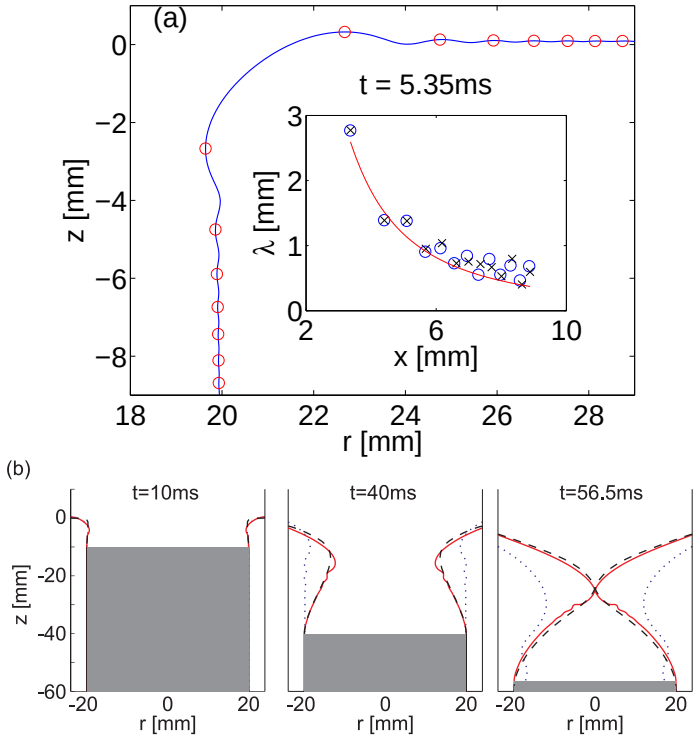


Figure 7.3: (a) Capillary waves for $V = 3$ m/s (Fr $= 45.9$) as obtained from the simulation. Wave crests are marked by red circles and allow an estimate of the dominant wave length $\lambda = 2\pi/k$ at a given position. The inset compares these wave lengths for the downward (blue circles) and outward (black crosses) waves to the theoretically expected behavior for capillary waves (red line). (b) The natural cavity dynamics (red solid) as a superposition of two hypothetical settings: without surface tension (black dashed) and without gravity (blue dotted) for $V = 1$ m/s (Fr $= 5.1$).

waves (since $kR \gg 1$ during all but the very rapid collapse at the end of the cavity evolution) and $\omega$ designates the angular frequency, $k$ the wave vector and $\rho$ the density.

Using stationary phase approximation we calculate the dominant wave vector $k^*$ at a given distance $x$ from the source at time $t$: $k^* = \left(\frac{2}{3}x/t\right)^2 \rho/\sigma$. Our simulations allow for an accurate estimate of the dominant wave length $\lambda$ from the shape of the surface, cf. Fig. 7.3 (a). Comparison with the above equation as in the inset of Fig. 7.3 (a) confirms that the observed ripples on the surface are indeed capillary waves originating from the corner point as the cylinder top passes the water surface. The damping for capillary waves can be estimated as $t_{\text{damp}} \sim 1/(\nu k^2)$ obtaining, with a wave length of the order of 6mm (see Fig. 7.1 (b)), a damping time of 900ms, which is well beyond the closure time of the cavity.

The closing of the cavity is driven by hydrostatic pressure acting on every point of the free surface accelerating it inward as soon as the cylinder has passed. This accelerating force increases with the depth. Thus, points near the top surface start moving early with a small acceleration, while deeper points start with increasing delay, but higher acceleration [11, 13]. On a rippled surface this process favors the wave crests over the other points. The resulting closure depth will thus be determined by a combination of (i) hydrostatic pressure induced by gravity and (ii) capillary waves created by surface tension.

The numerically obtained closure depth shown in Fig. 7.4 reasonably reproduces the experimental results. The final regime scales with $\alpha_2 \approx 0.43$. Considering that the theory from [11, 13, 14] assumes a purely radial flow pattern and an initially perfectly cylindrial cavity shape, the prediction of $\frac{1}{3}$ is reasonably close to our observed exponent. Our simulations even make the identification of an intermediate regime possible, which due to its small range in Froude numbers cannot be clearly observed in experiments. The shift between numerical and experimental data on the Froude axis can be attributed to the fragility of the measurement process in and around the intermediate regime as well as to small contaminations which lower the surface tension of the water.

The insets in Fig. 7.4 elucidate precisely how the capillary waves lead to the discontinuous jumps between the different regimes of the closure depth: For Froude numbers near the transition point three different local minima of the radius come very close to meeting their counterpart on the opposite side. In the first regime the uppermost of the three minima closes first and thus determines the closure depth, while in the second regime the one located in the middle is the fastest to reach the central axis. Finally, when the lowest minimum closes before the other two, the third regime is attained. Figure 7.1 (d) – (g) show experimental photographs of this effect

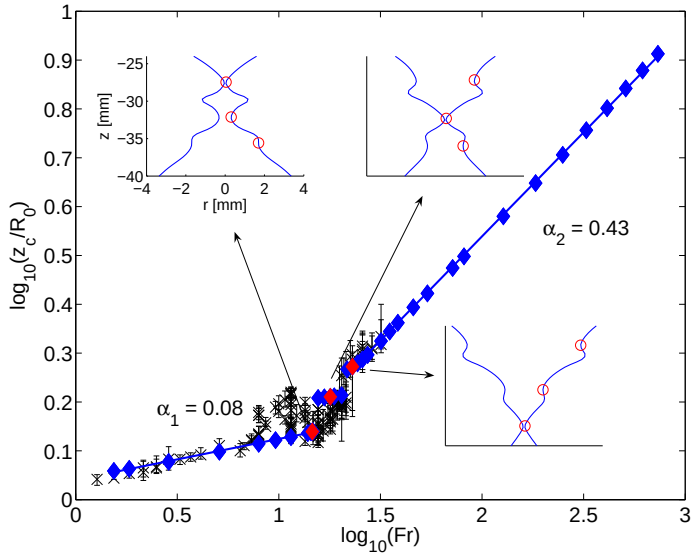


Figure 7.4: Comparison of the experimental closure depth (black crosses) with the numerical data (blue diamonds). The insets illustrate the shape of the cavity at pinch-off for one representative of each regime (axis are the same for all insets). The regimes are determined by which local minimum first meets its counterpart on the central axis.

at the transition point from the intermediate to the high Froude regime.

Since the behavior of capillary waves is determined by surface tension, one expects that modifications of the surface tension coefficient $\sigma$ should significantly alter the closure depth in the first and any intermediate regimes. For the last regime capillary waves are irrelevant and the scaling behavior of the closure depth can be derived independent of surface tension [11, 13, 14]. We have performed simulations with a ten-fold increase and decrease of $\sigma$ as compared to the natural value of 72.8mN/m for water as well as for a hypothetical liquid without any surface tension ($\sigma = 0$). As Fig. 7.5 demonstrates, the Froude number ranges for the three regimes are found to depend indeed strongly on the value of the surface tension coefficient. The length of the first regime significantly enlargens for a higher surface tension coefficient. As expected, the last regime is almost uninfluenced by changes in surface tension. For low surface tension merely the two asymptotic regimes exist and the intermediate regime is not observed anymore. The limiting case completely without surface tension possesses only one regime in reasonable agreement with the theoretical $\mathrm{Fr}^{1/3}$-scaling.

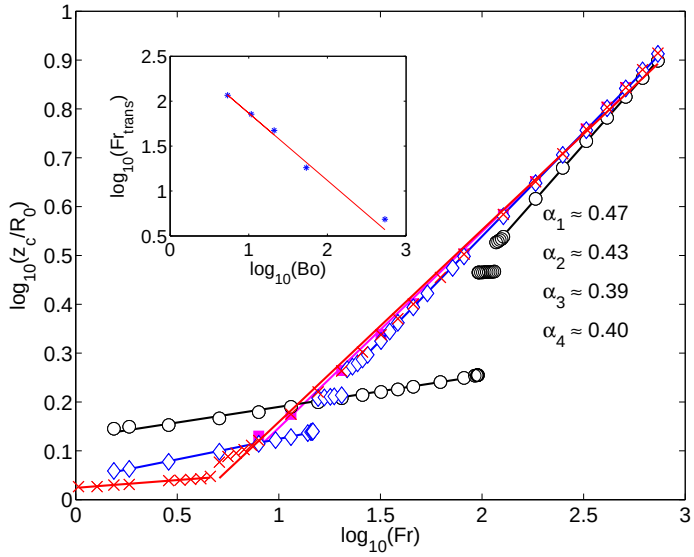


Figure 7.5: The numerical closure depth as a function of the Froude number and corresponding scaling exponents for different surface tension coefficients: $\sigma_1 = 728$ mN/m (black circles), $\sigma_2 = 72.8$ mN/m (blue diamonds), $\sigma_3 = 7.28$ mN/m (red crosses) and $\sigma_4 = 0$ (magenta squares). For $\sigma = 0$ no data at low Froude numbers is shown, since axial velocity components during the collapse prohibit the application of the $\mathrm{Fr}^{1/3}$-theory. The inset shows the onset of the high Froude number regime as a function of the Bond number with the red line depicting the expected scaling law $\mathrm{Fr}_{\mathrm{trans}} \sim \mathrm{Bo}^{-3/4}$.

With $x = z_c$ and $k^* \sim 1/z_c$ we estimate the relevant time scale for the capillary waves as $t_w \sim \sqrt{\rho/\sigma} z_c^{3/2}$ while the time scale for cavity closure is $t_c \sim z_c/V$. The onset of the high Froude number regime is now readily found by equating the ratio $t_w/t_c$ to a constant of order 1. Introducing the Bond number $\mathrm{Bo} = gR_0^2\rho/\sigma$ and making use of the theoretically expected scaling $z_c \sim \mathrm{Fr}^{1/3}$ this yields $\mathrm{Fr}_{\mathrm{trans}} \sim \mathrm{Bo}^{-3/4}$ which is in good agreement with our observations as shown in the inset of Fig. 7.5.

The cavity dynamics completely *without surface tension* and thus deprived of all capillary waves is illustrated by the black dashed lines in Fig. 7.3 (b). The blue dotted lines depict the evolution of a free surface starting with a (nearly) rectangular corner *without gravity* allowing us to study the formation of capillary waves in an isolated setting. The cavity dynamics under realistic conditions ($g = 9.81$ m/s$^2$ and $\sigma = 72.8$ mN/m) is shown in red and can clearly be identified as a superposition of the above

mentioned limiting cases. In the first instants, the real dynamics is almost identical to the one without gravity with its main feature being the capillary waves. Later, hydrostatic pressure becomes more important until finally the cavity approaches the shape of the pure gravity simulation with the capillary waves superposed on the cavity walls.

## 7.4 Conclusion

In conclusion, we have shown that capillary waves created when a submerging object passes the water surface have a strong and lasting influence on the dynamics of the cavity. This influence remains observable until the very end of the cavity collapse manifesting itself in clearly distinct regimes of the closure depth as a function of the submerging velocity. We have thus illustrated the lower limit to the continuous inertial-gravitational scaling regime observed in [11–14]. Since capillary waves are an unavoidable consequence of disturbances on a water surface, we expect that the effects elaborated in this Chapter will be of relevance to a wide range of related phenomena.

## References

[1] G. I. Barenblatt, *Scaling, self-similarity, and intermediate asymptotics* (Cambridge University Press) (1996).

[2] M. Tjahjadi, H. A. Stone, and J. M. Ottino, "Satellite and subsatellite formation in capillary breakup", J. Fluid. Mech. **243**, 297–317 (1992).

[3] M. P. Brenner, X. D. Shi, and S. R. Nagel, "Iterated instabilities during droplet fission", Phys. Rev. Lett. **73**, 3391–3394 (1994).

[4] J. Eggers, "Nonlinear dynamics and breakup of free-surface flows", Rev. Mod. Phys. **69**, 865 (1997).

[5] P. Doshi, I. Cohen, W. W. Zhang, M. Siegel, P. Howell, O. A. Basaran, and S. R. Nagel, "Persistence of memory in drop breakup: The breakdown of universality", Science **302**, 1185–1188 (2003).

[6] J. C. Burton, R. Waldrep, and P. Taborek, "Scaling and instabilities in bubble pinch-off", Phys. Rev. Lett. **94**, 184502 (2005).

[7] R. Bergmann, D. van der Meer, M. Stijnman, M. Sandtke, A. Prosperetti, and D. Lohse, "Giant bubble pinch-off", Phys. Rev. Lett. **96**, 154505 (2006).

[8] J. M. Gordillo and M. Pérez-Saborid, "Axisymmetric breakup of bubbles at high reynolds numbers", J. Fluid Mech. **562**, 303–312 (2006).

[9] N. C. Keim, P. Møller, W. W. Zhang, and S. R. Nagel, "Breakup of air bubbles in water: breakdown of cylindrical symmetry", Phys. Rev. Lett. **97**, 144503 (2006).

[10] J. Eggers, M. A. Fontelos, D. Leppinen, and J. H. Snoeijer, "Theory of the collapsing axisymmetric cavity", Phys. Rev. Lett. **98**, 094502 (2007).

[11] D. Lohse, R. Bergmann, R. Mikkelsen, C. Zeilstra, D. van der Meer, M. Versluis, K. van der Weele, M. van der Hoef, and H. Kuipers, "Impact on soft sand: void collapse and jet formation", Phys. Rev. Lett. **93**, 198003 (2004).

[12] J. W. Glasheen and T. A. McMahon, "Vertical water entry of disks at low froude numbers", Phys. Fluids **8**, 2078–2083 (1996).

[13] V. Duclaux, F. Caillé, C. Duez, C. Ybert, L. Bocquet, and C. Clanet, "Dynamics of transient cavities", J. Fluid Mech. **591**, 1–19 (2007).

[14] H. N. Oguz, A. Prosperetti, and A. R. Kolaini, "Air entrapment by a falling water mass", J. Fluid Mech. **294**, 181–207 (1995).

[15] A. Basu and J. K. Bhattacharjee, "Universal properties of threedimensional magnetohydrodynamic turbulence: do alfven waves matter?", J. Stat. Mech. P07002 (2005).

[16] F. Cioffi, F. Gallerano, and G. Troiani, "An experimental study of the turbulence statistics in a lagoon", Journal of Hydraulics Research **44**, 155–169 (2006).

[17] T. Grumstrup, J. B. Keller, and A. Belmonte, "Cavity ripples observed during the impact of solid objects into liquids", Phys. Rev. Lett. **99**, 114502 (2007).

# 8

# Nucleation threshold and deactivation mechanisms of nanoscopic cavitation nuclei *

†

*The acoustic nucleation threshold for bubbles trapped in cavities has theoretically been predicted within the crevice theory by Atchley & Prosperetti [J. Acoust. Soc. Am. 86, 1065-1084 (1989)]. Here, we determine this threshold experimentally, by applying a single pressure pulse to bubbles trapped in cylindrical nanoscopic pits ("artificial crevices") with radii down to 50 nm. By decreasing the minimum pressure stepwise, we observe the threshold for which the bubbles start to nucleate. The experimental results are quantitatively in excellent agreement with the theoretical predictions of Atchley & Prosperetti. In addition, we provide the mechanism which explains the deactivation of cavitation nuclei: gas diffusion together with an aspherical bubble collapse. Finally, we present superhydrophobic nuclei which cannot be deactivated, unless with a high-speed liquid jet directed into the pit.*

*To be published as: Bram M. Borkent, Stephan Gekle, Andrea Prosperetti, and Detlef Lohse, "Nucleation threshold and deactivation mechanisms of nanoscopic cavitation nuclei", Phys. Fluids *accepted* (2009).

†The numerical simulations in this Chapter are part of the present thesis. The experimental and theoretical work is due to Bram Borkent.

## 8.1 Introduction

Water can be ruptured at much smaller tensile stresses than theoretically is expected [1]. The reason for this discrepancy could be the existence of small inhomogeneities in the liquid, which may exist even when special care on the cleanliness of the water has been taken [2]. The inhomogeneities, whatever their origin might be, have received the generic name "cavitation nuclei", while the bubble generation produced in this way is termed heterogeneous nucleation. Cavitation nuclei are generally long-lived and it is believed that they consist at least in part of a volume of gas [3]. This observation excludes the possibility of the inhomogeneities being free spherical gas bubbles, as these are unstable. To account for stable gaseous cavitation nuclei, two types are distinguished in the literature: bubbles stabilized by a skin (see Ref. [3] and references therein) and bubbles trapped inside a surface defect ("crevice model") [4–9].
The principle of the crevice model dates back to 1944 [4] and has found extensive qualitative experimental evidence over the years. Greenspan and Tschiegg [10], for example, reported that removing particles larger than $0.2\mu$m in diameter increased the tensile strength of water to about 200 bar (see also Refs. [2, 11]). Others found that the addition of suspended particles lowers the nucleation threshold [12–17], while pre-experimental pressurization of water increases the nucleation threshold [5, 18]. Although these findings are in line with the general idea of the crevice model, none of the experiments could quantitatively verify the theoretical crevice model as developed by Atchley & Prosperetti [8] in 1989. One of the reasons is that their predictions are valid for a single cavity of a well-defined shape, while in practice the liquid usually contains a wide variety of nuclei of different sizes and shapes. Even in ultrapure water with a controlled number of microparticles, the sizes of the nuclei present on the microparticles can exhibit size variations yielding a wide range of thresholds [18].
A step forward was achieved by Bremond *et al.* who were able to create monodisperse cavitation nuclei by trapping gas inside cylindrical holes of well-defined shape etched in silicon surfaces using standard lithography techniques [19–21]. Not only was the position and size of the nuclei perfectly controlled, but the nucleation event itself was also highly reproducible, so that it could be followed in time with stroboscopic methods without the need of expensive high-speed cameras.
Both conditions, the reproducibility of the experiment and the monodispersity of the nuclei present at fixed positions, are important ingredients of this Chapter. Here, we have downscaled the micropits of Bremond *et al.* two orders of magnitude, so that it becomes possible to experimentally verify the theoretical predictions made in the framework of the crevice model. This is the first aim of this Chapter. Secondly, we explore the mechanisms leading to the deactivation of nuclei after a single nucleation

event. In addition, we show that superhydrophobic cavitation nuclei can nucleate hundreds of times, without being deactivated. Our observations and interpretations have implications for an increased understanding of the behavior of cavitation nuclei down to length scales of a few tens of nm ("surface nanobubbles") [22].

## 8.2 Brief theoretical description

A comprehensive description and development of the crevice model can be found in the paper of Atchley & Prosperetti [8] with extensions to any axisymmetric geometry, including cylindrical cavities, given by Chappell & Payne [23]. In both papers, the authors predict the various nucleation thresholds as function of crevice shape, gas tension, and receding contact angle. Atchley & Prosperetti argue that a true nucleation event must be the result of the loss of mechanical stability of the nucleus, and calculated the threshold for two situations: the first threshold denotes the pressure at which the nucleus *inside* a crevice begins its unstable growth, and is the lowest pressure value belonging to a bubble reaching either the critical radius of curvature $R_c$, or the receding radius of curvature $R_R$, i.e. the radius of curvature at which the receding contact angle $\theta_R$ is reached. The second threshold is equivalent in definition, but holds for the bubble growing *outside* of the crevice mouth. The lower value of the first and second nucleation threshold is the one for which the bubble grows explosively out of the cavity. For the case of a bubble trapped in a cavity with volume $V_c$ with its interface at the crevice mouth, the (second) nucleation threshold is given by

$$p_L + \frac{2\sigma}{R} = p_v + \frac{V_0 p_{g,0}}{V_c + (\pi/3)g(\theta)R^3}, \tag{8.1}$$

with $p_L$ the liquid pressure, $p_v$ the vapor pressure, $V_0$ the initial volume of the gas, $p_{g,0}$ the initial gas pressure in the bubble, $\sigma$ the liquid-gas surface tension, and $(\pi/3)g(\theta)R^3$ the volume of the spherical-cap-shaped bubble with radius $R$ as it expands above the cavity [8] (see Fig. 8.1). Here, $g(\theta) = \left(2 + (2 + \sin^2\theta)\cos\theta\right)$ is a geometric function depending on the contact angle $\theta$. The right-hand side of Eq. 8.1 represents the expanding forces caused by the vapor and gas pressure, $p_v + p_g$, respectively, while the left-hand side represents the collapsing forces due to the liquid pressure and surface tension, respectively. Eq. 8.1 implies that, for nucleation to occur, the expanding forces should exceed the collapsing forces (condition 1). Secondly, this condition should persist for increasing $R$, i.e. $\mathrm{d}(p_g + p_v)/\mathrm{d}R > \mathrm{d}(p_L + 2\sigma/R)/\mathrm{d}R$ (condition 2).

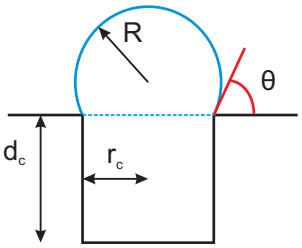


Figure 8.1: Cylindrical cavity with its dimensions. The initial gas-liquid interface is flat (dashed line), while the expanding bubble has a radius of curvature $R$ and contact angle $\theta$ with the flat surface.

Let us now consider the case - which we will examine experimentally - of a cylindrical cavity with radius $r_c$ and depth $d_c$, under the assumption that the initial gas-liquid interface at the crevice mouth is approximately flat (i.e. we assume a negligible effect of the hydrostatic pressure and gas-saturated water), so that we can write $V_0 = V_c = \pi r_c^2 d_c$. For $\theta_R \geq \pi/2$ the nucleation threshold is the pressure needed to pull the bubble beyond its minimum radius while it expands from the cavity, i.e. $R_{\min} = R_R = r_c/\sin\theta_R$. Now, Eq. 8.1 can be rewritten as

$$p_L = p_v + \frac{3p_{g,0}}{3+(r_c/d_c)g(\theta_R)/\sin^3\theta_R} - \frac{2\sigma\sin\theta_R}{r_c}. \tag{8.2}$$

This prediction will be verified experimentally in this Chapter. At the point $R = R_{\min} = R_R$ the bubble experiences the maximum collapsing force. Any further reduction of the liquid pressure will make the bubble expand, thus reducing the surface tension pressure, and the bubble will grow explosively with the contact angle fixed at $\theta_R$. Equations 8.1 and 8.2 are illustrated in Fig. 8.2, for an air bubble trapped in a cylindrical pit with dimensions $r_c = 250\,\text{nm}$ and $d_c = 500\,\text{nm}$ and with $p_{g,0} = 10^5\,\text{Pa} - p_v$, $p_v = 73\cdot 10^2\,\text{Pa}$ and $\theta_R = 100^\text{o}$. The graph shows the expanding and the collapsing forces for two cases: 1) $p_L = -0.20\,\text{MPa}$ (Blake threshold [24, 25] for a free bubble with $R_0 = r_c$) and 2) $p_L = -0.486\,\text{MPa}$ (prediction of Eq. 8.2). From this plot it is readily seen that the expanding pressure in the second case is always larger than the collapsing pressure, and that $\mathrm{d}(p_g + p_v)/\mathrm{d}R > \mathrm{d}(p_L + 2\sigma/R)/\mathrm{d}R$.

For $\theta_R < \pi/2$ the nucleation threshold is much more complicated to calculate. At $R = R_{\min} = r_c$ the collapsing force due to surface tension is indeed maximum, but now $\mathrm{d}(p_g + p_v)/\mathrm{d}R < \mathrm{d}(p_L + 2\sigma/R)/\mathrm{d}R$ and therefore $p_L(R_{\min})$ cannot be the nucleation threshold. Also $p_L(R_R)$ is not the correct threshold, as this gives a stable equilibrium in the upper branch of the compressive force curve. Instead, the threshold needs to

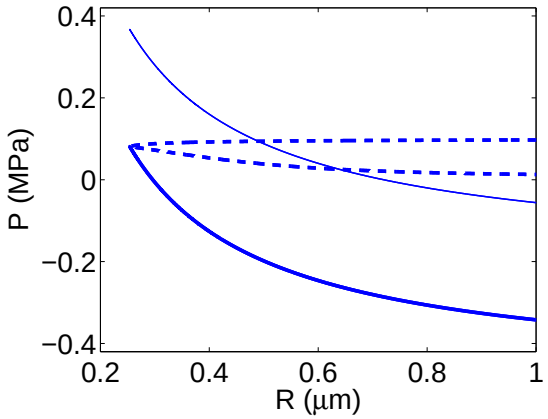


Figure 8.2: Graph of the expanding forces (right-hand side of Eq. 8.1, dashed line) and the collapsing forces (left-hand side of Eq. 8.1, solid lines) for a bubble expanding from a cylindrical pit with $r_c = 250\,\text{nm}$, $d_c = 500\,\text{nm}$, $p_{g,0} = 10^5\,\text{Pa} - p_v$, $p_v = 73 \cdot 10^2\,\text{Pa}$ and $\theta_R = 100^\text{o}$. The expanding forces (dashed line) show two branches corresponding to the possible solutions of $R$. The upper branch reflects the initially flat bubble during its first expansion phase: $R$ decreases from $R = R_\infty$ to $R = R_R$; the lower branch shows the solutions for the bubble expanding during its second phase: $R$ increases from $R = R_R$ to larger sizes. The collapsing forces are shown for two cases: 1) $p_L = -0.20\,\text{MPa}$ (thin solid line) and 2) $p_L = -0.486\,\text{MPa}$ (thick solid line). For case 1, the expanding forces dominate over the collapsing forces and the bubble will expand, until at $R = 0.49\mu\text{m}$ a stable equilibrium is reached. No nucleation will occur in this case. In case 2 the expanding forces are larger than the collapsing forces for all possible solutions of $R$, and as a result the bubble will grow explosively.

be found by numerically solving $\mathrm{d}(p_g + p_v)/\mathrm{d}R = \mathrm{d}(p_L + 2\sigma/R)/\mathrm{d}R$, which is an implicit equation as the contact angle depends on the radius $R$, through $\sin\theta = r_c/R$, as long as the receding contact angle has not yet been reached.
In the prediction of $p_L$ the gas term is significant for cavities down to a few hundred nm in radius and will therefore be taken into account in the present analysis.

## 8.3 Materials & methods

### 8.3.1 Experimental setup

The experimental setup to investigate the nucleation behavior of bubbles trapped in well-defined cavities is similar to that used by Bremond *et al.* [19–21] and sketched in Fig. 8.3. Cavitation is induced by a focused shock wave generator (Piezoson 100, Richard Wolf GmbH) consisting of piezoelectric elements mounted on a spherical cap at the bottom of the liquid bath, which is filled with 1 liter of air-saturated water (Milli-Q Synthesis A10, Millipore). The cavitation activity is recorded optically with a CCD camera (Flowmaster, LaVision) through a long-distance microscope (Model K2, Infinity). Illumination is provided by a flash lamp in reflection mode. The liquid pressure $p_L$ is obtained with the help of a calibrated glass fiber hydrophone (FOPH 500, RP Acoustics). The pressure is derived by measuring the reflected intensity of the laser beam at the fiber tip, which depends on the density of the water as affected by the local pressure [26]. At the acoustic focus the pressure signal is typically characterized by a pressure peak (duration $\sim 1\,\mu$s) followed by a negative pressure phase ($\sim 5\mu$s). The intensity of the pressure pulse can be varied in twenty discrete steps. Since the smallest possible pressure decrease at the acoustic focus $\min(p_L) = -3.2$ MPa is already too large for our purpose, the samples are translated horizontally (away from the acoustic focus) along the line of sight, until the pressure signal is sufficiently weak that nucleation does not occur at the smallest pressure drop, but only at larger pressure decreases. The hydrophone tip (diameter: $100\,\mu$m) is positioned $\sim 0.1$ mm in front of the chip surface, at an angle with the vertical plane of $10-20^\circ$. We took care of the close proximity between tip and surface by checking: 1) that the hydrophone tip end was not touching the chip surface (as this gave noisy data); 2) that the tip was in the optical focus of the camera (differences of 0.1 mm could be detected by comparing sharpness of the pictures). The corresponding pressure signals are recorded using a low pass filter (cutoff frequency 2.2 MHz) and averaged over 25 recordings to reduce the noise. A typical recording of the averaged pressure signal obtained 25 mm out of focus is shown in Fig. 8.4 and corresponds to the experiment with the sample containing pits of 246 nm in radius.

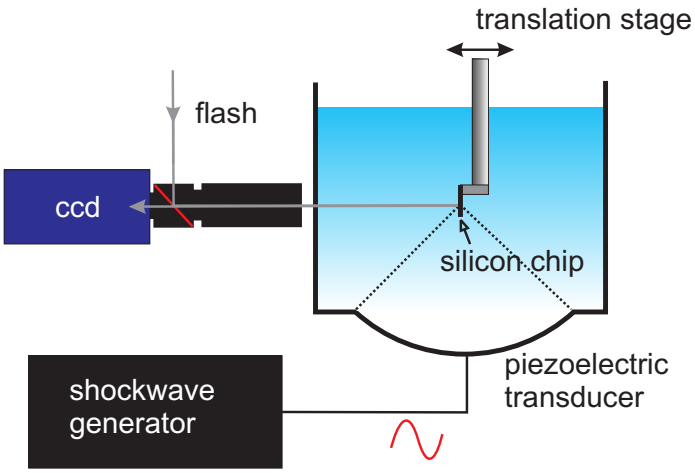


Figure 8.3: Sketch of the experimental setup.

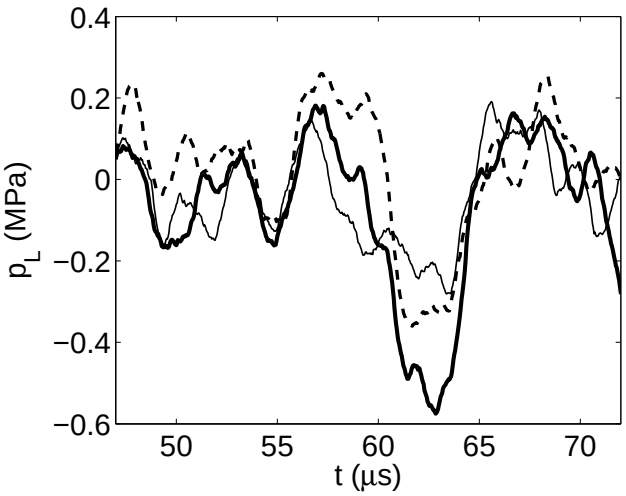


Figure 8.4: Three pressure signals with increasing strength recorded at the chip surface 25 mm out of focus, corresponding to the experiment with sample B ($r_c$ = 246 nm). Each line is the mean of 25 recordings. From these signals the minimum pressure can be extracted: -0.24 MPa (thin solid line), -0.35 MPa (dashed line) and -0.54 MPa (thick solid line)

### 8.3.2 Samples with nanopits

The substrates of interest are silicon pieces of $5 \times 5\,\mathrm{mm}^2$ diced from a Si(100) wafer. The nanoscopic cylindrical pits are directly etched into the substrate by a focused ion beam (FIB) in a $6 \times 6$ square pattern, with $200\,\mu$m distance between the pits. The resulting $1 \times 1\,\mathrm{mm}^2$ pattern is located at the center of the chip. In order to facilitate detailed imaging by atomic force microscopy (AFM) and scanning electron microscopy (SEM) identical pits are etched near the chip corner. Four samples (A-D) were studied with the following dimensions (determined with SEM) of the nanopits: A) $r_c = 495\,\mathrm{nm}$; B) $r_c = 246\,\mathrm{nm}$; C) $r_c = 53\,\mathrm{nm}$; D) $r_c = 50 - 60\,\mathrm{nm}$. In sample A-C the pattern consisted of uniformly sized pits, with depth $d_c = 2r_c$, while in sample D each column of pits had different depths (75, 100, 200, 300, 500, and 1000 nm), which influenced the radial pit size per column by a few nm (50, 50, 50, 55, 57, and 60 nm resp.); see Fig. 8.5 for the corresponding SEM pictures. Notice that $r_c$ has been measured precisely with SEM, while $d_c$ could not be measured and should therefore be regarded as an indicative value of the depth. In contrast to $r_c$, the exact depth of the pits (which only determines the initial gas volume) does not matter too much for the overall bubble dynamics, provided that the radius $r_c$ is small enough, which is the case in our experiments. After production the samples were cleaned ultrasonically in ethanol (15 minutes), followed by an oxygen plasma (5 min.), a chemical cleaning step using a fresh (5:1) Piranha mixture (30 min.) and again an ultrasonic bath in ethanol (15 min.). This yielded clean and completely wetting substrates, which were characterized by a smoothly dewetting contact line (if not, the whole process was repeated). Subsequently, the samples were hydrophobized with 1-*H*,1-*H*,2-*H*,2*H*-perfluorodecyltrichlorosilane following Ref. [27]. The advancing and receding contact angles on the surface were $\theta_a = 124^\mathrm{o}$ and $\theta_r = 100^\mathrm{o}$. After immersion in water it was confirmed with AFM in tapping mode that a horizontal gas-liquid meniscus was present at the mouth of the pits.

## 8.4 Results

### 8.4.1 Nucleation from gas-filled nanopits

To see whether it is possible to nucleate bubbles from nanopits as small as 53 nm in radius, samples A-C were immersed in the liquid bath allowing air to be entrapped in the pits. In successive experiments the samples were put at the acoustic focus of the shock wave generator and subjected to a pressure pulse with $p_m = \min(p_L) = -3.2\,\mathrm{MPa}$. This value is sufficiently below the nucleation thresholds of the three samples, i.e. $-0.23\,\mathrm{MPa}$, $-0.48\,\mathrm{MPa}$, and $-2.59\,\mathrm{MPa}$ respectively (see Eq. 8.2), to

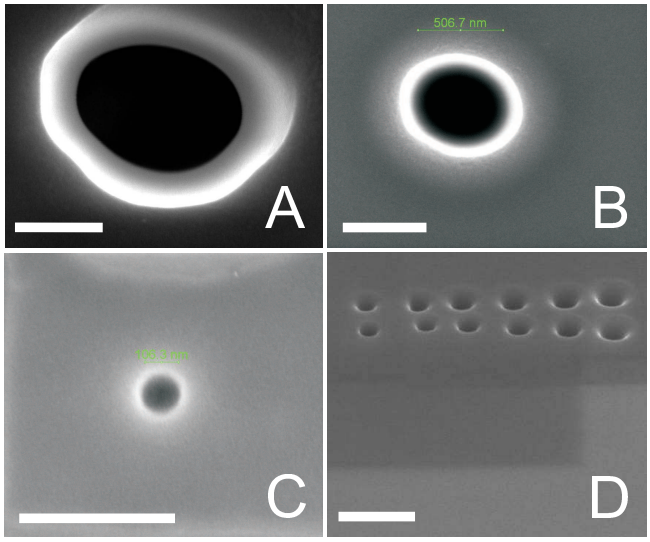


Figure 8.5: SEM images of samples A-D, respectively. The bars in each picture denote 500 nm. The ellipsoidal shapes for sample A and B are due to drift in the SEM chamber, i.e. the pits have circular cross-sections in reality.

expect nucleation of bubbles from the nanopits. The camera and flash were triggered a few $\mu$s after passage of the negative part of the shock wave to capture the expanding bubbles at maximum sizes. The result is depicted in Fig. 8.6 for the samples A-C, respectively. Sample A and B showed almost perfect bubble patterns, with each bubble corresponding to the position of the nanoscopic cavitation nucleus. In each experiment, the cavitation nuclei had to be 're-activated' (filled with air again), since it was not possible to nucleate bubbles a second time without taking the sample out of the water first [20]. With sample C a maximum amount of 34 bubbles could be nucleated in the first experiment, implying that it is indeed possible to nucleate bubbles from such small cavities. While sample A and B showed perfect reproducibility, the number of bubbles nucleating from sample C declined dramatically in later experiments, even when the negative pressure amplitude was increased to -7 MPa. Presumably, small contaminant molecules had decreased the contact angle locally, leading to completely wetted nanopits. To test this possibility, the old hydrophobic coating was stripped off with an oxygen plasma and the sample was hydrophobized again through the cleaning and coating steps described before. This process indeed re-activated part of the nuclei ($\sim$ 80% of the pits) though the number of bubbles declined again in successive experiments.

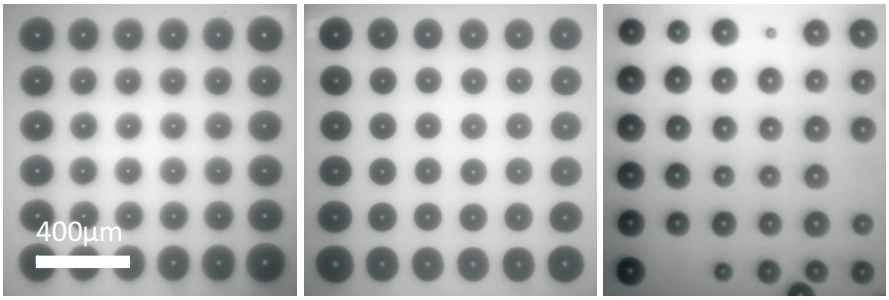


Figure 8.6: Cavitation bubbles nucleated from cylindrical pits with radius $r_c =$ 495 nm (left), $r_c = 246$ nm (middle) and $r_c = 53$ nm (right), and depth $d_c = 2r_c$ for a pressure pulse with $p_m = -3.2$ MPa.

### 8.4.2 Determination of the experimental nucleation threshold

The experimental nucleation threshold of the nanosized cavities can be obtained by moving the samples to a position in the liquid bath where the pressure drop $p_m$ is sufficiently small that no nucleation occurs. By lowering $p_m$ stepwise the cavities will nucleate at a certain negative pressure amplitude which is the experimental nucleation threshold. To observe the bubbles optically, it is not sufficient for the negative pressure to be low enough, but it should also last long enough in time. A lower limit to the time $\Delta t$ the bubble needs to grow to visible size is estimated, by first estimating the critical size $R_{c,o}$ to be optically observable. We take $R_{c,o} \sim 3$ image pixels = 3 pix $\times$ 2.9 $\mu$m /pix = 8.7 $\mu$m. Now, using [21, 28] $\dot{R} = \left(\frac{2}{3}\frac{p_v - p_m}{\rho}\right)^{1/2}$ with $\rho$ the liquid density and $\dot{R}$ the bubble wall velocity, it follows that $\Delta t = R_{c,o}/\dot{R} = 0.9\,\mu s$ (sample A), $0.6\,\mu s$ (sample B) and $\sim 0.3\,\mu s$ (sample C and D). The minimum pressure level which lasts $\Delta t$ is the negative pressure amplitude $p_m$ of interest. Note that the difference with the absolute minimum pressure level is in most cases only a few percent, much smaller than the typical statistical error, which is $\sim 0.2$ MPa in the cases of sample A and B, and $\sim 0.4 - 0.6$ MPa in the case of sample C.

Let us first consider the case of sample B ($r_c = 246$ nm, $d_c = 2r_c$). The sample was put 25 mm out of the acoustic focus, and three pressure pulses with increasing strength (Fig. 8.4) were applied successively, without taking the sample out of the water. A typical result is shown in Fig. 8.7. With the first pulse ($p_m = -0.24$ MPa) no cavitation bubbles could be observed (Fig. 8.7a). The second pressure pulse ($p_m = -0.35$ MPa), resulted in a few nucleated bubbles (always in the top rows of the pattern), but the majority of the nuclei in the pattern still did not cavitate (Fig. 8.7b). The third pressure pulse, with $p_m = -0.54$ MPa, was able to nucleate all remain-

| $p_m$ (MPa) | Amount of bubbles in exp. 1-8 | | | | | | | | mean |
|---|---|---|---|---|---|---|---|---|---|
| | 1 | 2 | 3 | 4 | 5 | 6 | 7 | 8 | |
| -0.24 | 0 | 0 | 0 | 0 | 0 | 0 | 0 | 0 | 0 |
| -0.35 | 11 | 9 | 8 | 15 | 10 | 8 | 8 | 7 | 10 |
| -0.54 | 23 | 27 | 28 | 19 | 25 | 27 | 27 | 29 | 26 |

Table 8.1: Results of eight experiments with sample B ($r_c = 246\,\text{nm}$, $d_c = 2r_c$). In each experiment the minimum pressure $p_m$ is decreased in three successive steps. The majority of the pits nucleates at $p_m = -0.54\,\text{MPa}$.

ing nuclei (Fig. 8.7c). Note that the nuclei which nucleated with the second pulse could not be nucleated with the stronger third pulse, implying that the nuclei can be used only once. Nuclei which were not nucleated during the second pulse, however, survived and were nucleated with the stronger third pulse. The experiment was repeated eight times with reproducible results (Table 8.1): on average 0, 10, and 26 bubbles were counted for the three applied pressure pulses, respectively.When the third pulse ($p_m = -0.54\,\text{MPa}$) was applied without the other two preceding ones, the full pattern became visible (Fig. 8.7d). Since the majority of the pits nucleated at $p_m = -0.54\,\text{MPa}$ it is reasonable to assume that this pressure amplitude is above the experimental nucleation threshold for sample B, while the weaker pulse ($p_m = -0.35\,\text{MPa}$) is (just) below the experimental nucleation threshold.

Since it was always the top row of pits plus some part of the second top row that nucleated at an apparently less negative $p_m$, it could very well be that there was a pressure variation along the chip surface in the vertical direction (i.e. direction of wave propagation), so that the most negative pressure occurred at the top row of the pits. In Fig. 8.7c and d we can indeed see that bubbles become slightly larger in the vertical direction, indicating a more negative pressure along this direction. With our setup we have not been able to measure a difference in pressure between top and bottom location of the pattern.

A similar experiment was carried out with sample A ($r_c = 495\,\text{nm}$, $d_c = 2r_c$, Fig. 8.8). Again the sample was subjected to three successive pressure signals of decreasing negative pressure without being taken out of the water. For the lowest pressure amplitude ($p_m = -0.20\,\text{MPa}$) no cavitation bubbles could be detected optically (Fig. 8.8a). A larger amplitude of $p_m = -0.23\,\text{MPa}$ yielded 14 bubbles of different sizes, with some of them barely visible (Fig. 8.8b), while a further reduction of the liquid pressure ($p_m = -0.34\,\text{MPa}$) resulted in no visible bubbles at all (Fig. 8.8c). What happened with the remaining $36 - 14 = 22$ pits? As the lowest negative pressure was not able to nucleate them, they must already have been nucleated during the first two

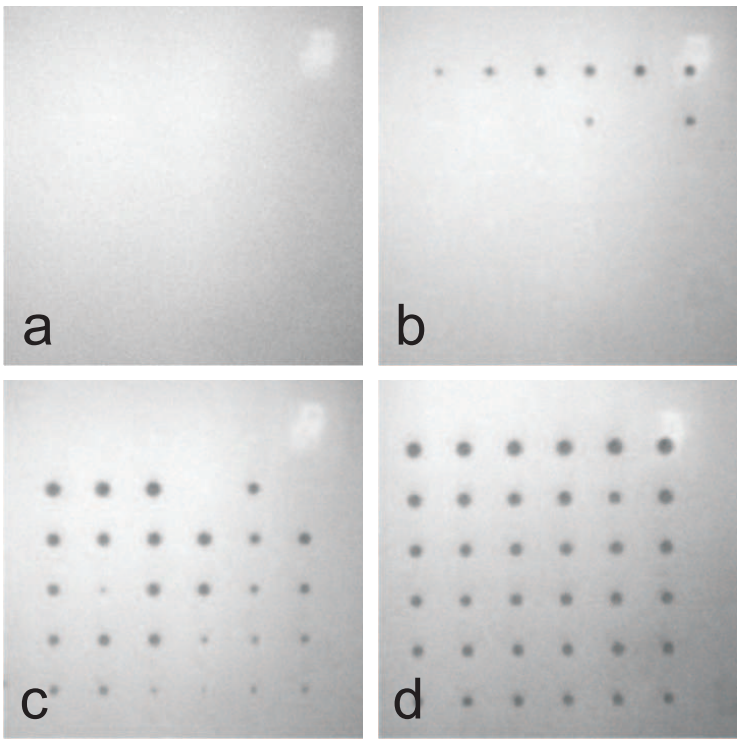


Figure 8.7: Cavitation bubbles emerging from $6 \times 6$ cylindrical pits with $r_c = 246\,\text{nm}$ (sample B), for three successively applied pressure pulses: a) $p_m = -0.24\,\text{MPa}$; b) $p_m = -0.35\,\text{MPa}$; c) $p_m = -0.54\,\text{MPa}$. The full pattern develops when $p_m = -0.54\,\text{MPa}$ is applied without the other two preceding pulses (d).

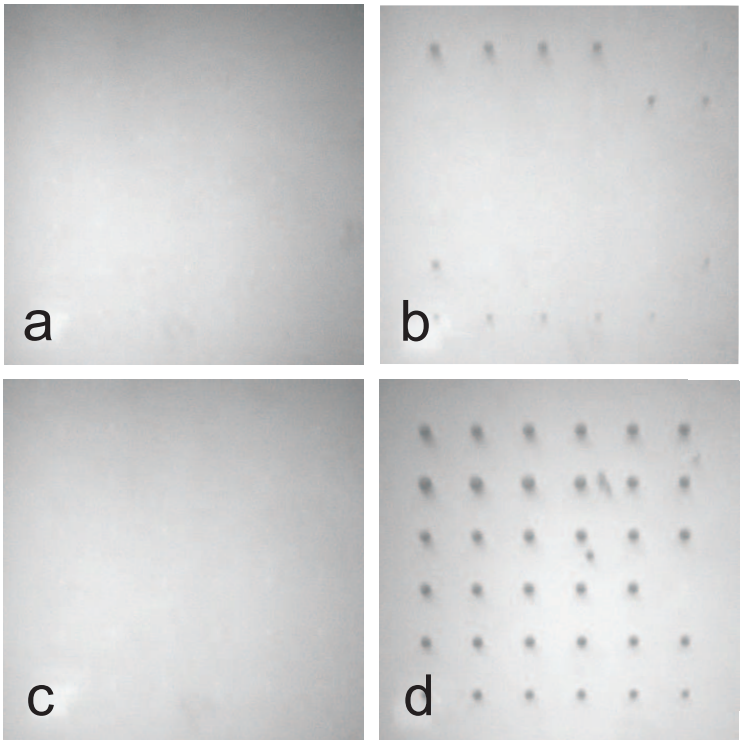


Figure 8.8: Cavitation bubbles emerging from $6 \times 6$ cylindrical pits with $r_c = 495\,\text{nm}$ (sample A), for three successively applied pressure pulses: a) $p_m = -0.20\,\text{MPa}$; b) $p_m = -0.23\,\text{MPa}$; c) $p_m = -0.34\,\text{MPa}$. The full pattern develops when $p_m = -0.34\,\text{MPa}$ is applied without the other two preceding pulses (d).

pulses, i.e. the nucleation took place below optical resolution. This is possible as the resolution of our optical detection is limited and the pressure pulse in this case is relatively weak (i.e. $\dot{R}$ is small). Therefore, in contrast with case B, we are not able to measure the pressure for which nucleation does *not* take place. When the third pulse ($p_m = -0.34\,\text{MPa}$) was applied without the other two preceding pulses, the full pattern became visible (Fig. 8.8d). Hence, this is the pressure level for which we are sure that nucleation of the full pattern takes place.

Finally, sample D was studied, which consists of nanopits with $50\,\text{nm} \leq r_c \leq 60\,\text{nm}$ and varying depths. Just like sample C, the shallow pits on sample D nucleated only a few times, and could not be nucleated in later experiments. Fortunately, two columns with the deepest pits ($d_c = 500\,\text{nm}$ & $r_c = 57\,\text{nm}$, and $d_c = 1000\,\text{nm}$ & $r_c = 60\,\text{nm}$) could be nucleated repeatedly, and the nucleation threshold could be measured for

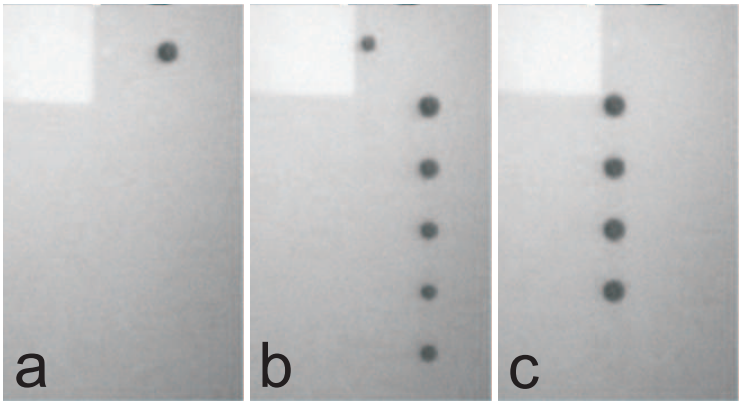


Figure 8.9: Cavitation bubbles emerging from $2 \times 6$ cylindrical pits (sample D) with $r_c = 57\,\text{nm}$, $d_c = 500\,\text{nm}$ (left column) and $r_c = 60\,\text{nm}$, $d_c = 1000\,\text{nm}$ (right column), for three successively applied pressure pulses: a) $p_m = -2.3\,\text{MPa}$; b) $p_m = -2.6\,\text{MPa}$; c) $p_m = -3.0\,\text{MPa}$.

these pits. The experiment was very similar to the ones described before, but now the sample was 12 mm away from the acoustic focus. A typical experimental result is depicted in Fig. 8.9. First, a pressure pulse with $p_m = -2.3\,\text{MPa}$ was applied and 1 pit from the right column ($r_c = 60\,\text{nm}$) was nucleated. A stronger second pulse ($p_m = -2.6\,\text{MPa}$) was able to nucleate the remaining 5 pits from this column, though other pits in the sample did not nucleate, as they were smaller. Reducing the negative pressure further ($p_m = -3.0\,\text{MPa}$) resulted in the nucleation of the left column of pits with $r_c = 57\,\text{nm}$. Hence, a small variation in pit sizes of just a few nm is reflected in a different nucleation threshold. It is also observed that the pits did not nucleate a second time, despite their huge aspect ratios.

### 8.4.3 Comparison with theoretical prediction

How do the experimental results compare with theoretical predictions? In Fig. 8.10 the theoretical nucleation threshold (line), based on Eq. 8.2, is plotted as a function of the pit radius $r_c$ together with the experimental results (symbols). We used $d_c = 2r_c$ as is the case in sample A and B. Note that for the pits present in sample D the gas pressure term is negligible: the difference between $d_c = 2r_c$ and $d_c = 20r_c$ changes the theoretical prediction for pits of $r_c = 50\,\text{nm} < 1\%$. The experimental data points at which full nucleation was detected for samples A, B and D are depicted by crosses, while the experimental pressures where nucleation of the full pattern (just)

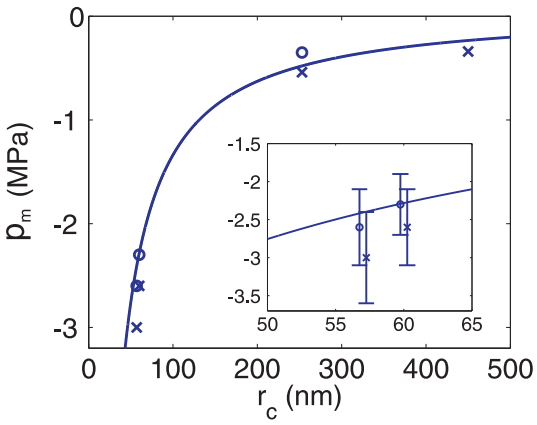


Figure 8.10: Nucleation threshold as function of the pit radius for both theory (line) and experiment (symbols, crosses: nucleation, circles: no nucleation). The inset shows a zoom in with errorbars. For visibility overlapping points are shifted $\pm 0.25$ nm with respect to each other.

did not happen are marked with circles. The inset shows the experimental results for sample D including typical error bars depicting the standard deviation of the pressure recordings.

We observe a striking quantitative agreement between theory and experiment for all samples. Pressure amplitudes for which nucleation was first detected are below the line marking the nucleation threshold. Pressure amplitudes for which nucleation did not occur are either above this line, i.e. in the regime where nucleation is not expected, or the line is within experimental errorbars. For sample D it was observed that the nucleation threshold strongly depends on the size of the pits: pit radii just a few nm smaller resulted in a significantly lower nucleation threshold, in agreement with the steep slope of $p_m(r_c)$ around these values.

### 8.4.4 Deactivation of cavitation nuclei

It is well known that artificial nucleation sites in boiling continue to be active for a long time, emitting many bubbles [29]. Similarly, the microscopic wall cracks and scratches in a glass full of beer or champagne are seen to emit bubbles for a very long time [30]. Even in cavitation studies on bare hydrophobic substrates, bubbles trapped in localized defects could be nucleated more than a hundred times [19]. Thus, there is something special in the deactivation of nuclei observed here which makes this

situation different from the others. What is the physical mechanism responsible for the deactivation of the nuclei?

The main mechanism responsible for the deactivation of nuclei is encountered during the collapse phase of the bubble, where a wall-directed jet is formed. In the case of a single bubble (or weak interaction among bubbles) the jet momentum is expected to be directed mostly normal to the wall [31, 32]. When bubble-bubble interaction is non-negligible, on the other hand, the jet momentum may be deflected away from the normal [21].

In order to shed light on this proposed deactivation mechanism, numerical simulations were carried out to elucidate the shape of the air-liquid interface during the bubble collapse. For this we used the boundary-integral method described in Ref. [33] based on a potential flow description of the liquid dynamics. The liquid-solid angle was prescribed to be $\theta_a = 124^\circ$ which corresponds to the experimentally determined advancing contact angle of water on the substrates. At the starting point of the simulations the bubble was assumed to be a segment of a sphere with a radius significantly larger than the cavity radius $r_c$, see Fig. 8.11 (a). The pressure inside the bubble was assumed to be uniform, satisfying the adiabatic relation $p_0/V_0^{1.4} = p_{bub}/V_{bub}^{1.4}$ with the initial pressure $p_0$ and $V_0$ the volume of the crevice, and $p_{bub}$ and $V_{bub}$ the instantaneous pressure and volume of the bubble, respectively. After release the bubble begins to shrink rapidly due to both surface tension and the low internal pressure. Eventually it evolves into an almost cylindrical shape as illustrated in Fig. 8.11 (c). This air cylinder collapses radially and finally closes in a single point on the axis of symmetry, leaving a small air bubble entrapped above the pinch-off point, see Fig. 8.11 (d). Towards pinch-off the liquid rushing radially inwards has to accelerate more and more to satisfy the requirement of mass conservation. When the advancing liquid front reaches the axis of symmetry a high pressure develops and the flow is deflected up and down to form two fast, needle-like water jets. The continuing collapse of the air cavity below and above the pinch-off point provides additional momentum to the two jets[34]. The downward jet protrudes deeply into the cavity until it hits the bottom of the cavity as illustrated in Fig. 8.11 (e)-(f). For simplicity we neglected the upper bubble here which is expected to have only negligible influence on the downward jet. Upon reaching the bottom the impacting jet would form a violent, non-axisymmetric splash which cannot be captured by our numerical technique. Nevertheless, one can easily imagine the continuation of the process: as more and more liquid enters the cavity through the jet, the cavity is flooded with liquid, making a second nucleation impossible. We checked that the jet mechanism is present for pits in the size range studied here ($50\,\text{nm} < r_c < 500\,\text{nm}$) and is independent of the initial bubble size, pit depth, and contact angle.

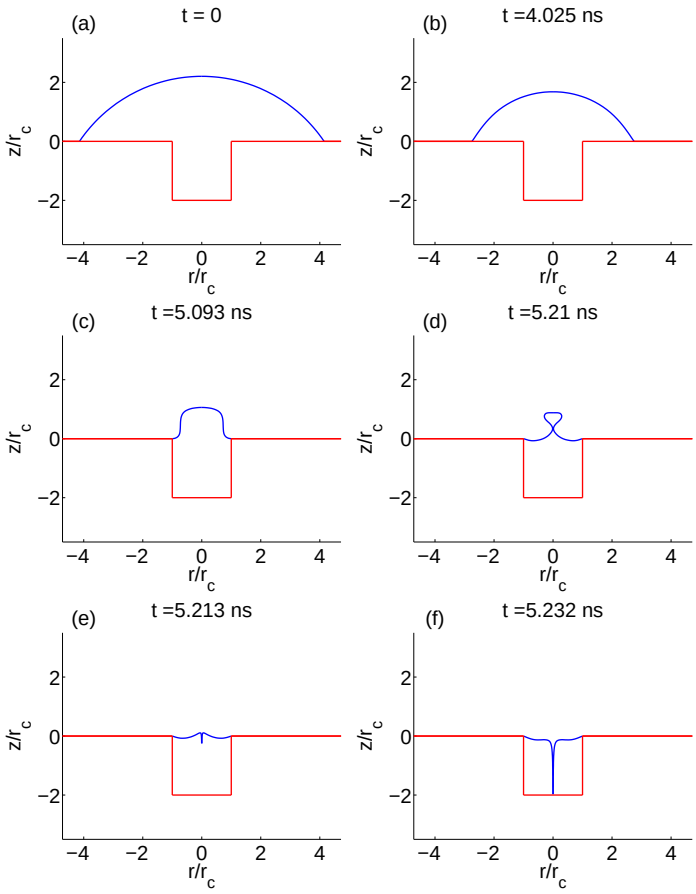


Figure 8.11: (a) Initial configuration for a spherical bubble (blue) with radius $5r_c$ on top of the cavity (red). The (advancing) contact angle is $\theta = 124°$. Due to the low pressure inside the cavity the bubble starts to collapse (b) evolving into an almost cylindrical shape (c), which eventually closes on the axis of symmetry in a single point (d). From the pinch-off location a downward jet protrudes into the cavity (e) eventually hitting the cavity bottom (f). Here it would cause a splash filling the cavity with liquid.

The previous explanation is not applicable to the case of strong mutual interaction between the bubbles, when the jet tends to be deflected away from the wall-normal [21], although the nuclei are still observed to be de-activated after emission of the first bubble. We estimated that within the typical lifetime of the bubble (typically $t_b \sim 10\mu$s), the gas molecules have ample time to fill the bubble volume to reach a uniform gas pressure. The gas transport is probably a combination of convection and diffusion, although the latter mechanism alone would already be sufficient to move all the gas: The typical diffusion length scale is $\sim \sqrt{Dt_b} = 10\mu$m, using the diffusion coefficient $D \sim 10^{-5}$m$^2$/s. In the cases studied here the pits are $< 1\mu$m deep, i.e. much smaller than the typical diffusion length scale. Also, the volume of a typical bubble is $10^5 - 10^7$ larger than the volume of the nanopits, allowing the majority of the gas to move from the pit into the bubble [‡]. During collapse, the interaction between bubbles breaks the bubble in such a way that a large gas-vapor bubble goes away from the sample, and only a tiny fraction ($< 0.001\%$) of the initial gas remains in the pit, which therefore remains essentially full of vapor and is easily filled by the liquid. Suppose that during this filling process a tiny amount of gas remains in the pit. The contact angle being larger than 90° would force the meniscus to be curved towards the gas and consequently the bubble would grow by diffusion. We estimated that the waiting time in between two successive shots (in our case: 15 s) would then be enough to refill the pits completely with gas by diffusion, and a second nucleation event should then be possible. Since we never have observed a second nucleation, we conclude that the pits have to be filled with liquid completely during bubble collapse.
These conclusions agree with our experimental results. In the cases A-D we observed no differences between strong (Fig. 8.6) and weak (Figs. 8.7, 8.8 & 8.9) bubble interaction: in both situations the pits were emptied after one nucleation event, in line with the explanations provided here.
This situation can be compared with the previously mentioned continuous and long-lived emission of bubbles in carbonated beverages and the related phenomena observed with enhanced surfaces frequently used in boiling heat transfer [35, 36]. In none of these cases the bubbles collapse and therefore the primary mechanism for the filling up and consequent de-activation of the pits is present.

### 8.4.5 Superhydrophobic nuclei

To show the importance of the liquid jet into the pits, experiments using superhydrophobic nuclei are illustrative. Cylindrical pits, etched in Si(100) with a diameter

[‡]Notice that this estimation does not take into account the confinement of the nanopits and their large aspect ratios (case D), which may lead to lower values of the diffusion coefficient.

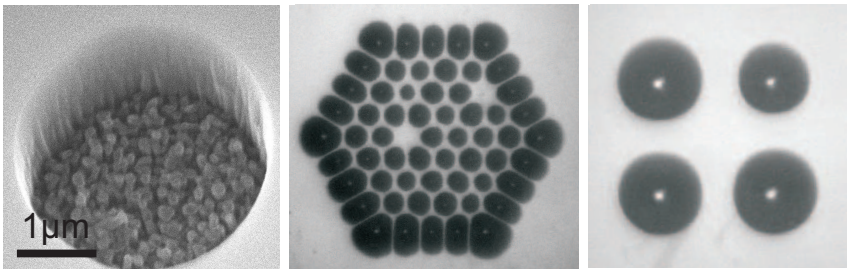


Figure 8.12: A superhydrophobic pit (left) can be nucleated hundreds of times, provided that the liquid jet in the bubble collapse phase is not directed into the pit. Center: a hexagonal pattern of superhydrophobic pits (100 $\mu$m in between the pits) after 230 nucleation events shows only 2 defects. Right: a square pattern (300 $\mu$m in between the pits) is completely intact after 100 shots.

of 4 $\mu$m, were created with a superhydrophobic bottom layer (see Fig. 8.12), consisting of hydrophobic pillars of $\sim 100$ nm in diameter (created through a black silicon etching process [37] and a hydrophobic fluoro-carbon top layer). The combination of hydrophobicity with roughness is known to create superhydrophobicity [38] with typical contact angles $> 160^{o}$. When the bubbles were strongly interacting (leading to wall-parallel jets), we observed that the pits remained active nucleation sites even after hundreds of shots (see Fig. 8.12). On the contrary, in the case of a single bubble (wall-normal jet) we observed that the micropits were deactivated after a few nucleation events. To explain this striking difference one really has to take the direction of the liquid jet into account. Apparently, the wall-parallel jet is not able to wet the superhydrophobic bottom of the pits, while the vigorous, ultra-thin jet directed towards the superhydrophobic bottom layer presumably pushes the liquid from the dewetted into the wetted state. From other work it is indeed known that a force may be required to overcome the energy barrier associated with this wetting transition [39]. Once in the wetted state, the superhydrophobic pit is deactivated and cannot be nucleated again, apart of course from drying the whole sample.

## 8.5 Conclusion

In conclusion, Atchley & Prosperetti's 1989 crevice model of cavitation nuclei is experimentally verified using nanoscopic well-defined nuclei. Advanced etching techniques allowed us to create cylindrical pits down to 50 nm in radius with high ac-

curacy in both their size, depth and mutual position. Upon immersion in water, the hydrophobic nanopits trapped air and served as nucleation sites. Stepwise lowering of the acoustic minimum pressure allowed us to determine the nucleation threshold at which the pits start to cavitate. We found that the experimental results are in very good agreement with the theoretical predictions. This implies that in shock wave experiments the size of cavitation nuclei can be determined by measuring the pressure at which they start to nucleate, provided that either the cavity geometry is known, so that one can incorporate the effect of the expanding gas from the pit, or that the gas content of the pit can be neglected, which is roughly the case for $r_c < 200\,\mathrm{nm}$ (in case $d_c = r_c$).

Cavitation nuclei were deactivated after a single nucleation event, despite differences in width, depth and aspect ratios of the pits. The two mechanisms contributing to this effect are diffusion of gas out of the pit during the lifetime of the bubble and the subsequent aspherical collapse of the bubble. Numerical simulations show that in the case of weak bubble-bubble interaction, a sharp wall-normal liquid jet is formed which hits the bottom of the cavities, thus vigorously wetting the pits. Superhydrophobic nuclei can only be wetted thanks to this wall-normal jet. For strong bubble-bubble interactions with wall-parallel jets, superhydrophobic pits remain active nucleation sites, even after hundreds of nucleation events, in contrast to standard hydrophobic pits. In systems where one wants to control the number of cavitation nuclei which do not deactivate, superhydrophobic pits may find applications.

# References

[1] F. Caupin and E. Herbert, “Cavitation in water: a review”, C. R. Physique **7**, 1000–1017 (2006).

[2] E. Herbert, S. Balibar, and F. Caupin, “Cavitation pressure in water”, Phys. Rev. E **74**, 041603 (2006).

[3] K. A. Mørch, “Reflections on cavitation nuclei in water”, Phys. Fluids **19**, 072104 (2007).

[4] E. N. Harvey, D. K. Barnes, W. D. McElroy, A. H. Whiteley, D. C. Pease, and K. W. Cooper, “Bubble formation in animals”, J. Cell. Compar. Physl. **24**, 1–22 (1944).

[5] M. Strasberg, “Onset of ultrasonic cavitation in tap water”, J. Acoust. Soc. Am. **31**, 163–176 (1959).

[6] R. E. Apfel, "The role of impurities in cavitation-threshold determination", J. Acoust. Soc. Am. **48**, 1179–1186 (1970).

[7] L. A. Crum, "Tensile strength of water", Nature **278**, 148–149 (1979).

[8] A. A. Atchley and A. Prosperetti, "The crevice model of bubble nucleation", J. Acoust. Soc. Am. **86**, 1065–1084 (1989).

[9] K. A. Mørch, "Cavitation nuclei and bubble formation – a dynamic liquid-solid interface problem", J. Fluids Eng. **122**, 494–498 (2000).

[10] M. Greenspan and C. E. Tschiegg, "Radiation-induced acoustic cavitation: Apparatus and some results", J. Res. Natl. Bur. Stand., Sect. C **71**, 299–312 (1967).

[11] L. J. Briggs, "Limiting negative pressure of water", J. Appl. Phys. **21**, 721 (1950).

[12] R. A. Roy, S. I. Madanshetty, and R. E. Apfel, "An acoustic backscattering technique for the detection of transient cavitation produced by microsecond pulses of ultrasound", J. Acoust. Soc. Am. **87**, 2451–2458 (1989).

[13] S. I. Madanshetty and R. E. Apfel, "Acoustic microcavitation: Enhancement and applications", J. Acoust. Soc. Am. **90**, 1508–1514 (1991).

[14] S. I. Madanshetty, R. A. Roy, and R. E. Apfel, "Acoustic microcavitation: its active and passive acoustic detection", J. Acoust. Soc. Am. **90**, 1515–1526 (1991).

[15] S. I. Madanshetty, "A conceptual modeal for acoustic microcavitation", J. Acoust. Soc. Am. **98**, 2681–2689 (1995).

[16] C. X. Deng, Q. Xu, R. E. Apfel, and C. K. Holland, "Inertial cavitation produced by pulsed ultrasound in controlled host media", J. Acoust. Soc. Am. **100**, 1199–1208 (1996).

[17] H. B. Marschall, K. A. Mørch, A. P. Keller, and M. Kjeldsen, "Cavitation inception by almost spherical solid particles in water", Phys. Fluids **15**, 545–553 (2003).

[18] B. M. Borkent, M. Arora, and C. D. Ohl, "Reproducible cavitation activity in water-particle suspensions", J. Acoust. Soc. Am. **121**, 1406–1412 (2007).

[19] N. Bremond, M. Arora, C. D. Ohl, and D. Lohse, "Cavitation on surfaces", J. Phys.: Condens. Matter **17**, S3603–S3608 (2005).

[20] N. Bremond, M. Arora, C. D. Ohl, and D. Lohse, "Controlled multibubble surface cavitation", Phys. Rev. Lett. **96**, 224501 (2006).

[21] N. Bremond, M. Arora, S. M. Dammer, and D. Lohse, "Interaction of cavitation bubbles on a wall", Phys. Fluids **18**, 121505 (2006).

[22] B. M. Borkent, S. M. Dammer, H. Schönherr, G. J. Vancso, and D. Lohse, "Superstability of surface nanobubbles", Phys. Rev. Lett. **98**, 204502 (2007).

[23] M. A. Chappell and S. J. Paine, "The effect of cavity geometry on the nucleation of bubbles from cavities", J. Acoust. Soc. Am. **121**, 853–862 (2007).

[24] C. E. Brennen, *Cavitation and Bubble Dynamics* (Oxford University Press, New York) (1995).

[25] T. G. Leighton, *The Acoustic Bubble* (Cambridge University Press, Cambridge) (1994).

[26] J. Staudenraus and W. Eisenmenger, "Fiberoptic probe hydrophone for ultrasonic and shock-wave measurements in water", Ultrasonics **31**, 267 (1993).

[27] T. M. Mayer, M. P. de Boer, N. D. Shinn, P. J. Clews, and T. A. Michalske, "Chemical vapor deposition of fluoroalkylsilane monolayer films for adhesion control in microelectromechanical systems", J. Vac. Sci. Technol. B **18**, 2433–2440 (2000).

[28] M. S. Plesset and A. Prosperetti, "Bubble dynamics and cavitation", Annu. Rev. Fluid Mech. **9**, 145 (1977).

[29] V. K. Dhir, "Boiling heat transfer", Ann. Rev. Fluid Mech. **30**, 365–401 (1998).

[30] G. Liger-Belair, G. Polidorib, and P. Jeandeta, "Recent advances in the science of champagne bubbles", Chem. Soc. Rev. **37**, 2490–2511 (2008).

[31] T. B. Benjamin and A. T. Ellis, "The collapse of cavitation bubbles and the pressure thereby produced against solid boundaries", Philos. Trans. R. Soc. London, Ser. A **260**, 221 (1966).

[32] M. S. Plesset and R. B. Chapman, "Collapse of an initially spherical vapor cavity in the neighborhood of a solid boundary", J. Fluid Mech. **47**, 283 (1966).

[33] R. Bergmann, D. van der Meer, S. Gekle, A. van der Bos, and D. Lohse, "Controlled impact of a disc on a water surface: Cavity dynamics", J. Fluid Mech. **633**, 381–409 (2009).

[34] S. Gekle, J. M. Gordillo, D. van der Meer, and D. Lohse, "High-speed jet formation after solid object impact", Phys. Rev. Lett. **102**, 034502 (2009), *See Chapter 2 of this thesis.*

[35] A. D. Messina and E. L. Park, "Effects of precise arrays of pits on nucleate boiling", Int. J. Heat Mass Transfer **24**, 141–145 (1981).

[36] Y. Qi, J. F. Klausner, and R. Mei, "Role of surface structure in heterogeneous nucleation", Int. J. Heat Mass Transfer **47**, 3097–3107 (2004).

[37] H. Jansen, M. de Boer, R. Legtenberg, and M. Elwenspoek, "The black silicon method: a universal method for determining the parameter setting of a fluorine-based reactive ion etcher in deep silicon trench etching with profile control", J. Micromech. Microeng. **5**, 115–120 (1995).

[38] D. Quéré, "Surface chemistry – fakir droplets", Nat. Mater. **1**, 14–15 (2003).

[39] N. A. Patankar, "Transition between superhydrophobic states on rough surfaces", Langmuir **20**, 7097–7102 (2004).

# 9 Conclusions and Outlook

In this thesis we studied – mainly – the impact of thin circular discs with radii between 1 and 3 cm on a liquid surface at speeds between 0.5 and 20 m/s. Using a powerful combination of high-speed video and numerical simulations we could elucidate various aspects of this strikingly beautiful event.

In Chapter 2 we studied the mechanism behind the formation of the high-speed jets ejected after the closure of the impact cavity. Our main finding was the vital importance of the radial energy focussing along the entire wall of the impact cavity. In contrast to other situations [1–4], the hyperbolic flow around the pinch-off point turned out to be not the relevant mechanism behind jet formation. We proposed an analytical model which we found in very good quantitative agreement with experimental data and numerical simulations. The only ingredients to the model are two constants of order one and a sink distribution $q_c(z)$ describing the collapsing cavity at pinch-off. Further, we could show that the liquid forming the jet originates from a thin layer straddling the surface of the impact cavity.

In Chapter 3 we derived explanations for the entire shape of the jet including the final, surface-tension driven break-up at the jet tip. For this we divided the flow structure into three different regions: The *axial acceleration region*, where the radial momentum of the incoming liquid is converted into axial momentum, the *ballistic region*, where fluid particles experience no further acceleration and move constantly with the velocity obtained at the end of the acceleration region and the *jet tip region* where the jet eventually breaks into droplets. We applied these three modeling steps

to jets formed after the collapse of an impact cavity as well as to jets created after the pinch-off of a bubble injected through an underwater nozzle [5–7] and found good agreement in both cases.

In Chapter 4 we showed that just prior to cavity closure the air is pushed out of the shrinking cavity so violently that it attains supersonic velocities. For this we extended our boundary-integral method into a full multiphase scheme combining it with a compressible Euler solver to account for the gas dynamics which was described in Chapter 5. Surprisingly, we found that the very high air speeds can be reached even though the pressure inside the cavity is merely 2% higher than the surrounding atmosphere. We illustrated how the air affects the cavity shape close to the final collapse in two different ways: (i) the initially smoothly curved neck shape acquires an almost "kinked" shape which can be attributed to a Bernoulli suction effect and (ii) the initially downward motion of the neck reverses its direction and starts to travel upwards. The quantitatively consistent observation of both effects in numerics and experiment made us confident that our rather involved numerical procedure truthfully reflects reality.

In Chapter 6 we demonstrated that the final universal regime predicted in [8, 9] for the pinch-off of a bubble surrounded by liquid indeed exists for a variety of different realizations under idealized conditions neglecting air flow. Its duration, however, depends strongly on the type of system. Our simulations showed that for the impacting disc it is in the range of milliseconds while for gas bubbles grown from an underwater nozzle the duration can be as short as a few nanoseconds. With these findings we were able to reconcile the claim of universality in bubble pinch-off [8–10] with an apparent dependence on initial conditions [11], an apparently constant scaling exponent [6, 7, 12], and with the observation that non-inertial forces can be dominant in many experimental settings [13–15].

In Chapter 7 we replaced the impacting disc by a long cylinder. This modification led to the observation of a new and unexpected phenomenon: we found that capillary waves that are created as the cylinder top passes the water surface can significantly affect the closure depth of the cavity. In contrast to the completely continuous scaling of the closure depth with the impact velocity (encapsulated in the dimensionless Froude number) for the impacting disc, the closure depth for the cylinder follows the scaling predicted in [16–18] only for sufficiently high impact velocities. Below this threshold it exhibits discontinuous jumps whose origin are precisely the capillary waves created at the very beginning of the process.

Finally, in Chapter 8 we explained the filling of nanopits after the nucleation and subsequent collapse of a bubble by a jetting mechanism similar to the one described in Chapter 2. This effect is the reason why bubble nucleation by a low pressure pulse

can be triggered only once and why for subsequent pulses no further nucleation is observed.

Besides the various aspects studied in this thesis, the fascinating process of a solid object hitting a liquid surface still holds a large number of mostly unexplored phenomena which seem worth investigating.

It is an intriguing question how the cavity formation and jet ejection process will look like for non-axisymmetric objects. Recent work for the pinch-off of bubbles grown from underwater nozzles has revealed how small non-axisymmetric perturbations oscillate during the collapse of the cavity [19]. The behavior of larger disturbances beyond the linear regime studied in [19] is still largely unexplored. Using elliptical or "flower-shaped" discs one could easily use our existing experimental setup to impose arbitrary deformations on the initial cavity and then study its subsequent collapse. On the numerical side, in principle, a full three-dimensional boundary-integral code would be required to simulate such non-axisymmetric impacts. In a first approach, however, one could restrict the simulation to the horizontal plane containing the closure location of the cavity, thus neglecting the – presumably small – vertical flow components. Such a two-dimensional boundary-integral simulation is significantly simpler and can be obtained in a rather straightforward manner by extending the existing axisymmetric code.

Taking the above one step further one could imagine two discs being pulled down simultaneously thus creating two cavities very close to each other. During the collapse these two cavities would interact which will certainly affect the collapse and jetting dynamics. It would be very interesting to see to what extent this interaction is similar to the one observed for bubbles collapsing close to each other [20].

The impact of a liquid droplet on a water surface usually creates a jet which is much slower and thicker than the one observed after the impact of a solid object such as our disc. That said, there exists a small parameter range for which the jet rather abruptly becomes very thin and fast [21] – and thus much more reminiscent to the jets described in Chapters 2 and 3. Most studies report that precisely in this regime of thin jets a small bubble is formed at the bottom of the initial impact crater [21, 22]. One can therefore expect that these thin jets are created during the pinch-off of this bubble precisely by the mechanism presented in this thesis. It would be tempting to furnish a definite proof of this expectation.

A challenging extension to the experimental setup would be the installation of a pressure chamber around the water tank. With this one could modify the density of the surrounding gas (either by changing the pressure or by using gases different from

air). Besides the obvious relevance that this will have on the results in Chapter 4, it will most likely also affect the studies of Chapter 6. This is because air flow seems to be the main limiting factor for the experimental observability of the universal pinch-off regime. It is therefore conceivable that reducing the air density would prolong the duration of the universal regime and thereby make it easier to observe in our experiment.

An interesting aspect related to Chapter 4 is the air flow above the water surface. It has long been known that the air sucked into the cavity right after impact causes an underpressure in the center of the crown splash which – for large enough impact velocities – is able to draw the splash wall together leading to the so-called "surface seal". Despite its ubiquity this phenomenon has hardly ever been studied in detail. To date, not even the thickness of the ejected liquid sheet is known, let alone its intricate dynamics.

While the motivation for the present research was mainly of fundamental scientific nature, one can nevertheless envision numerous applications of the described processes. A major factor in climate modeling is the deposition of atmospheric carbon dioxide in the oceans. One of the mechanisms behind the deposition process is the entrainment of air by rain droplets as they impact on the ocean surface [22, 23]. The small bubbles which are left behind after droplet impact will furthermore oscillate with a characteristic frequency which is an important component of underwater noise.

In medical applications, the thin liquid jets which are created after the collapse of the impact cavity might be of practical use: for this, one would first inject a small bubble coated with a medical substance into a patient's blood. Sending an ultrasound pulse would then make the bubble collapse and release its content in a sharp and highly-directed jet reminiscent to the jetting observed in solid-object impact. This jet could be even strong enough to pierce a cell membrane and deliver almost any desired drug directly into the cell [24, 25].

# References

[1] M. S. Longuet-Higgins, "Bubbles, breaking waves and hyperbolic jets at a free surface", J. Fluid Mech. **127**, 103–121 (1983).

[2] J. E. Hogrefe, N. L. Peffley, C. L. Goodridge, W. T. Shi, H. G. E. Hentschel, and

D. P. Lathrop, "Power-law singularities in gravity-capillary waves", Physica D **123**, 183–205 (1998).

[3] B. W. Zeff, B. Kleber, J. Fineberg, and D. P. Lathrop, "Singularity dynamics in curvature collapse and jet eruption on a fluid surface", Nature **403**, 401–404 (2000).

[4] L. Duchemin, S. Popinet, C. Josserand, and S. Zaleski, "Jet formation in bubbles bursting at a free surface", Phys. Fluids **14**, 3000–3008 (2002).

[5] H. N. Oguz and A. Prosperetti, "Dynamics of bubble growth and detachment from a needle", J. Fluid Mech. **257**, 111–145 (1993).

[6] N. C. Keim, P. Møller, W. W. Zhang, and S. R. Nagel, "Breakup of air bubbles in water: breakdown of cylindrical symmetry", Phys. Rev. Lett. **97**, 144503 (2006).

[7] S. T. Thoroddsen, T. G. Etoh, and K. Takehara, "Experiments on bubble pinch-off", Phys. Fluids **19**, 042101 (2007).

[8] J. Eggers, M. A. Fontelos, D. Leppinen, and J. H. Snoeijer, "Theory of the collapsing axisymmetric cavity", Phys. Rev. Lett. **98**, 094502 (2007).

[9] M. A. Fontelos, J. H. Snoeijer, and J. Eggers, "The spatial structure of bubble pinch-off", preprint (2009).

[10] J. M. Gordillo and M. Pérez-Saborid, "Axisymmetric breakup of bubbles at high reynolds numbers", J. Fluid Mech. **562**, 303–312 (2006).

[11] R. Bergmann, D. van der Meer, M. Stijnman, M. Sandtke, A. Prosperetti, and D. Lohse, "Giant bubble pinch-off", Phys. Rev. Lett. **96**, 154505 (2006).

[12] J. C. Burton and P. Taborek, "Bifurcation from bubble to droplet in inviscid pinch-off", Phys. Rev. Lett. **101**, 214502 (2008).

[13] J. M. Gordillo and M. A. Fontelos, "Satellites in inviscid breakup of bubbles", Phys. Rev. Lett. **98**, 144503 (2007).

[14] J. M. Gordillo, "Axisymmetric bubble collapse in a quiescent liquid pool. I. Theory and numerical simulations", Phys. Fluids **20**, 112103 (2008).

[15] R. Bolaños-Jiménez, A. Sevilla, C. Martinez-Bazán, and J. M. Gordillo, "Axisymmetric bubble collapse in a quiescent liquid pool. II. Experimental study", Phys. Fluids **20**, 112104 (2008).

[16] H. N. Oguz, A. Prosperetti, and A. R. Kolaini, "Air entrapment by a falling water mass", J. Fluid Mech. **294**, 181–207 (1995).

[17] D. Lohse, R. Bergmann, R. Mikkelsen, C. Zeilstra, D. van der Meer, M. Versluis, K. van der Weele, M. van der Hoef, and H. Kuipers, "Impact on soft sand: void collapse and jet formation", Phys. Rev. Lett. **93**, 198003 (2004).

[18] V. Duclaux, F. Caillé, C. Duez, C. Ybert, L. Bocquet, and C. Clanet, "Dynamics of transient cavities", J. Fluid Mech. **591**, 1–19 (2007).

[19] L. E. Schmidt, N. C. Keim, W. W. Zhang, and S. R. Nagel, "Memory-encoding vibrations in a disconnecting air bubble", Nature physics **5**, 343–346 (2009).

[20] N. Bremond, M. Arora, S. M. Dammer, and D. Lohse, "Interaction of cavitation bubbles on a wall", Phys. Fluids **18**, 121505 (2006).

[21] M. Rein, "Phenomena of liquid drop impact on solid and liquid surfaces", Fluid. Dyn. Res. **12**, 61–93 (1993).

[22] H. N. Oguz and A. Prosperetti, "Bubble entrainment by the impact of drops on liquid surfaces", J. Fluid Mech. **219**, 143–179 (1990).

[23] H. N. Oguz and A. Prosperetti, "Numerical calculation of the underwater noise of rain", J. Fluid Mech. **228**, 417–442 (1991).

[24] C. D. Ohl and R. Ikink, "Shock-wave-induced jetting of micron-sized bubbles", Phys. Rev. Lett. **90**, 214502 (2003).

[25] M. Postema, A. van Wamel, F. J. ten Cate, and N. de Jong, "High-speed photography during ultrasound illustrates potential therapeutic applications of microbubbles", Med. Phys. **32**, 3707–3711 (2005).

# Summary

A spectacular example of free surface flow is the impact of a solid object on a liquid: At impact a "crown" splash is created and a surface cavity (void) emerges which immediately starts to collapse due to the hydrostatic pressure of the surrounding liquid. Eventually the cavity closes in a single point about halfway down its length and shoots out a fast and extremely slender water jet. In the present thesis we study the impact of thin circular discs a few centimeters in radius with impact velocities of a few meters per second. Combining high-speed imaging with sophisticated boundary-integral computer simulations we elucidate various aspects of this fascinating process.

Next to their undisputable interest for fundamental science such impacts can also be of practical relevance in other disciplines. For oceanographic research it is important that raindrops falling on the ocean entrain small air bubbles after the pinch-off of the impact cavity. This behavior constitutes the main mechanism for carbon dioxide exchange between the sea and the atmosphere and is furthermore a major source of underwater noise. As a medical application, the thin liquid jets which are generated during the collapse of a liquid cavity such as the cavities produced during liquid impact represent a promising possibility for very localized drug delivery into cells or through a patient's skin.

The subject of Chapter 2 is the fast, almost needle-like liquid jet shooting upwards from the cavity closure location, which by then has turned into a stagnation point surrounded by a locally hyperbolic flow pattern. We show that this flow, however, is *not* the mechanism feeding the jet. Instead, only the radial energy focussing along the entire cavity wall is strong enough to eject the very fast and extremely slender liquid jet. This focussing makes the process reminiscent of the violent jets of fluidized metal created during the explosion "of lined cavities" in military and mining operations. We continue the well-known theory of a collapsing void (using a line of sinks on the axis of symmetry) beyond pinch-off to obtain a new and quantitative model for jet formation which agrees well with numerical and experimental data. We further show that the liquid contained in the jet originates exclusively from a very thin layer straddling the surface of the impact cavity.

In Chapter 3 we extend these results in three ways: first, we demonstrate the applicability of our jetting model also to liquid jets formed after the pinch-off of a bubble grown from an underwater nozzle. Second, we add a new analytical model which allows us to explain not only the formation mechanism but the entire shape of the jet itself. Third, we show that the breakup of the liquid jet due to a surface-tension driven instability can be described in a universal fashion such that the knowledge of only two dimensionless parameters defined at the beginning of jet formation is sufficient to obtain the size of droplets ejected from the jet tip.

In Chapters 4 and 5 we use multiphase simulations combining our boundary-integral method with a fully compressible Euler solver to illustrate the intricate structure of the air flow as it is squeezed out of the shrinking impact cavity. The striking result is that even in our simple system of a 2 cm disc impacting at merely 1 m/s the air flow easily attains *supersonic* velocities. Notably, the cavity pressure nonetheless is only 2% larger than the surrounding atmosphere and thus much lower than the pressures usually observed in supersonic flow through converging-diverging ("de Laval") nozzles in common aerodynamics. The key difference is that in our case the confining cavity is a *liquid* which is rapidly evolving in time – a situation for which no equivalent exists in the scientific or engineering literature.

Chapter 6 compares the pinch-off of our impact cavity with bubble pinch-off in three related situations: gas bubbles injected through a small orifice, bubble rupture in a straining flow, and surface-tension induced break-up of a bubble with an initially necked shape. Our simulations, extending over 12 decades in time, suggest that all systems eventually follow the universal behavior predicted in [Eggers *et al.*, Phys. Rev. Lett. **98**, 094502 (2007)], at least under idealized conditions neglecting air dynamics. However, the time scale for the onset of this final regime varies by orders of magnitude depending on the system in question: while for the impacting disc it is well in the millisecond range, for the gas injection needle universal behavior sets in only a few microseconds before pinch-off. These time scales determine whether or not universal behavior may be observable in a real experiment and thus reconcile the different views expressed in recent literature about the universal nature of bubble pinch-off.

In Chapter 7 we replace the impacting disc by a long, smooth cylinder. While for an impacting disc the depth at which the cavity closes scales continuously with the impact velocity, we show here that for a cylinder the closure depth does not strictly obey the expected scaling. Instead, it displays distinct regimes separated by discrete jumps which are consistently observed in experiment and numerical simulations. We quantitatively explain this behavior as a consequence of capillary waves which are created when the top of the cylinder passes the water surface.

Finally, in Chapter 8 we simulate the collapse of nanobubbles nucleating from small (50 nm) pits drilled into a silicon wafer. We find that just prior to final collapse a jet very similar in appearance to those in Chapter 2 forms and penetrates deep into the hole. This effect, by which the pits fill up entirely with water after bubble collapse, provides the explanation for the intriguing observation that each pit can nucleate a bubble exactly once.

# Samenvatting

Een van de meest spectaculaire voorbeelden uit de vloeistoffysica is het inslaan van een object op een wateroppervlak: Direct na de inslag ontstaat een vloeistofkroon die de rand vormt van een holte. Deze holte implodeert vervolgens onder invloed van de hydrostatische druk ten gevolge waarvan een vloeistofjet omhoog schiet. In dit proefschrift bestuderen wij de inslag van een schijf met een straal van enkele centimeters en een snelheid van enkele meters per seconde. Wij combineren hogesnelheids fotografie met geavanceerde boundary-integral computer simulaties om de verschillende aspecten van dit fascinerende proces beter te begrijpen.

Naast de wetenschappelijke drijfveer om een dermate bekend en zeer vaak optredend verschijnsel beter te begrijpen, is het inslag proces ook van groot praktisch belang. Als elke dag miljarden regendruppels op de zee vallen, produceert elk van hen een klein belletje in het water. In de klimaatwetenschappen vormen dergelijke processen het hoofdmechanisme voor het transport van kooldioxide van de atmosfeer naar de oceaan. Bovendien is het een belangrijke bron van onderwater geluid. In de medische fysica zijn wetenschappers bezig met het onderzoek om dunne water jets, vergelijkbaar met die die ontstaan tijdens de inslag, te gebruiken voor transport van medicijnen door celwanden of door de huid van een patient.

Het onderwerp van hoofdstuk 2 is het vormingsproces van de snelle en dunne water jet die omhoog schiet na het instorten van de holte. Op het moment van sluiten is het sluitpunt van de holte omgeven door een hyperbolische stroming. Wij laten echter zien dat deze stroming niet het mechanisme voor het ontstaan van de waterjet vormt en dat alleen het focusseren van radiële energie door de gehele wand sterk genoeg is voor het genereren van deze bijzonder snelle jet. Het mechanisme is vergelijkbaar met dat van de krachtige jets van vloeibaar metaal die optreden tijdens de implosie van “lined cavities” in militaire en mijnbouw operaties. Wij breiden de bekende theorie voor een instortende holte uit tot na de sluiting en verkrijgen hiermee een nieuw en kwantitatief model voor het ontstaan van de jet. Dit model is in goede overeenstemming met zowel experimenten als simulaties. Verder laten wij zien dat alle vloeistof in de jet afkomstig is van een zeer dunne laag aan de oppervlakte van de holte.

In hoofdstuk 3 breiden wij bovengenoemde resultaten op drie manieren uit: ten

eerste laten wij zien dat onze theorie voor de vorming van de jet ook toegepast kan worden op jets gevormd na het imploderen van bellen die geïnjecteerd worden in een vloeistof tank. Ten tweede formuleren wij een nieuw analytisch model waarmee wij de volledige vorm van de waterjet kunnen voorspellen. Ten derde onderzoeken wij hoe de jet in waterdruppels opbreekt door een instabiliteit die veroorzaakt wordt door de oppervlaktespanning. Wij beschrijven dit opbreken op een universele manier in termen van twee dimensieloze parameters die gedefinieerd worden bij het begin van het ontstaan van de waterjet. Daarmee kunnen wij de grootte voorspellen van de druppeltjes die aan de top van de jet ontstaan.

In hoofdstuk 4 and 5 maken wij gebruik van zogenoemde 'multiscale' simulaties. Deze bestaan uit een combinatie van onze boundary-integral methode en een methode voor het numeriek oplossen van de Euler vergelijkingen voor een compressibele gasstroming. Hierdoor maken wij de complexe structuur van de stroming van het gas tijdens het instorten van de inslagholte. Het verrassende resultaat is dat zelfs in ons eenvoudig systeem bestaande uit een schijf met een straal van 2 cm die inslaat met een snelheid van 1 m/s de stroming in het gas supersoon kan worden. Desondanks is de druk binnen de holte niet meer dan 2% hoger dan de omgevingsdruk en daarmee veel lager dan de druk die gewoonlijk nodig is voor een supersone gasstroming door een zogeheten "de Laval nozzle". Het voornaamste verschil is dat in ons geval de stroming versneld wordt in een geometrie die gevormd wordt door een vloeibaar wateroppervlak die zeer snel van vorm verandert.

In hoofdstuk 6 vergelijken wij het insnoeren van de holte (de zogeheten "pinch-off") in ons geval met de pinch-off in drie verwante situaties: gas bellen geïnjecteerd door een naald, het insnoeren van bellen in een vervormende stroming, en het insnoeren van bellen door middel van oppervlaktespanning. Onze simulaties, die twaalf decaden in de tijd bestrijken, bevestigen dat alle bestudeerde systemen uiteindelijk het universele gedrag voorspeld door [Eggers *et al.*, Phys. Rev. Lett. **98**, 094502 (2007)] volgen, ten minste onder ideale omstandigheden waarin de luchtstroming verwaarloosd kan worden. Desalniettemin kan, afhankelijk van het systeem, de tijdschaal waarin het universele regime zichtbaar is over meerdere orden van grootte variëren: voor de schijf duurt het maar liefst enkele milliseconden, terwijl het bij de gasinjectie slechts een paar microseconden duurt. Deze tijdschaal is van belang omdat zij bepaalt of het universele regime in een echt experiment te observeren zal zijn. Dit onderzoek verzoent de verschillende opvattingen in de recente literatuur over het universele karakter van het insnoeren van bellen.

In hoofdstuk 7 vervangen wij de schijf door een lange en gladde cilinder. In het geval van de schijf schaalt de sluitingsdiepte van de holte op een continue manier met de inslagsnelheid. Wij laten zien dat de cilinder dit verwacht schalingsgedrag niet

strikt volgt. Er zijn verschillende regimes met daartussen discrete sprongen die zowel in experiment en simulatie teruggevonden worden. Wij verklaren dit gedrag als het gevolg van oppervlaktegolven die ontstaan als de cilinder door het wateroppervlak wordt getrokken.

In hoofdstuk 8 simuleren wij het imploderen van nanobellen die groeien vanuit kleine (50 nm) putjes die in een silicon wafer zijn geëtst. Wij laten zien dat net voor de uiteindelijke implosie van de belletjes een jet ontstaat op een manier die vergelijkbaar is met die van de jets in de hoofdstukken 2 en 3. Deze jet kan tot op de bodem van de putjes doordringen. Dit verschijnsel, dat leidt tot het vullen van de putjes met vloeistof, is de verklaring waarom uit elk putje slechts een keer een belletje kan ontstaan.

# Acknowledgements

During my thesis I have been in the lucky and unusual situation to have no less than three advisors. Furthermore, I have been in the – even more unusual – situation that all three of them (mostly) agreed on how things should be done. For this I want to express my deepest gratitude to Detlef Lohse, Devaraj van der Meer, and José Manuel Gordillo.

Devaraj has been most successful in introducing me to fluid mechanics. His ability and willingness to find intuitive explanations for the most complicated material are quite amazing. I want to thank him for being a true "advisor" in the broadest possible sense providing help, support, and advice in any situation and for any possible problem. In addition, he is certainly the most thorough manuscript proofreader I ever met. Detlef has been a most inspiring and motivating supervisor. He was the best guide into the intricacies of the world of science that I could find. I want to thank him especially for sharing with me his great knowledge on how to prepare manuscripts, abstracts, presentations, proposals, and the like. José Manuel with his joyful nature and optimism has lifted my spirits in many difficult situations. It is amazing how convincing he can be that the *next* try will bring the definite solution – no matter how miserably the previous 99 tries have failed. Besides his invaluable scientific advice I want to thank him especially for his hospitality during my visits to Sevilla.

Next I would like to thank my two master students Johanna Bos and especially Ivo Peters with whom I had the great pleasure to continue working during his PhD project. Without Ivo's corresponding smoke measurements our gas flow simulations would be worth so much less. Also I want to thank my two internship students Benoit Vandamme and Amneet Pal Singh Bhalla. Willingly or not, these four taught me how difficult it is to teach. In working with them I have probably learnt more for myself than I was able to teach them.

I want to thank Joanita Leferink for being such an efficient secretary and for taking care of every imaginable problem. It is the merit of Bas Benschop that the percentage of time that I had to dedicate to non-science-related computer problems was kept to an absolute minimum and I want to thank him honestly for that. I also want to thank Martin Bos and Gert-Wim Bruggert for their support while I was still

doing experiments myself.

Let me further thank Andrea Prosperetti and Leen van Wijngaarden for sharing their enormous experience with me. I always greatly enjoyed discussions with them and I am grateful for the various feedback they gave me.

During teaching of the Physics of Fluids course, I had the pleasure of working with Edip Can, Hanneke Bluemink, and Jacco Snoeijer. I want to thank them for the good ambiance in which we could do this job.

Let me also thank all the enthusiastic volleyballers of the group who joined many times during the last four summers to play on the "beach" of Enschede.

Finally, I want to thank my wife Stefanie for the beautiful cover illustration of this booklet.

For financial support I want to acknowledge the Stichting FOM who funded this project.

# About the author

Stephan Gekle was born the 20th of June 1978 in Nürtingen in the state of Baden-Württemberg in South-Western Germany. He graduated from high school in 1998 after which he spent one year working in a geriatric center during his mandatory civilian service. In 1999 he began his studies of physics at the University of Stuttgart. In 2001/2002 he spent an Erasmus year at the University of Valladolid in Northern Spain.

During his studies he was serving as a student delegate to the Faculty Board among other functions. A voluntary internship led him to Guatemala where he researched the practical applicability of plant oil cooking stoves with local families. In a second internship he spent two summers at University Paris 6 where he worked on the description of social dynamics using methods of statistical physics. His master project then involved the non-linear dynamics of the classical Hamiltonian for a hydrogen atom in crossed electric and magnetic fields.

After graduating from the University of Stuttgart he started his PhD project at the University of Twente in March 2006.